University of Genoa

Department of Electrical, Electronic and Telecommunication Engineering and Naval Architecture (DITEN)

PhD in Science and Technology for Electronic and Telecommunication Engineering

Microwave Imaging of The Neck by Means of Inverse-Scattering Techniques

PhD Thesis

Chiara Dachena
March 2023

TUTORS: Prof. Andrea Randazzo
Prof. Matteo Pastorino

Coordinator of the PhD Course: Prof. Maurizio Valle

Contents

Chapter 1

Introduction

In recent decades, in the field of applied electromagnetism, there has been a significant interest in the development of non-invasive diagnostic methods through the use of electromagnetic waves, especially at microwave frequencies [1]. Microwave imaging (MWI) - considered for a long period an emerging technique - has potentialities in numerous, and constantly increasing, applications in different areas, ranging from civil and industrial engineering, with non-destructive testing and evaluations (example e.g., monitoring contamination in food, sub-surface imaging based on both terrestrial and space platforms; detection of cracks and defects in structures and equipments of various kinds; antennas diagnostics, etc.), up to the biomedical field [2], [3], [4], [5], [6], [7]. One of the first applications of microwave imaging (MWI) in the medical field was the detection of breast tumors [8], [9], [10], [11], [12], [13], [14], [15], [16], [17]. Subsequently, brain stroke detection has received great attention [18],[19], [20], too. Other possible clinical applications include imaging of torso, arms, and other body parts [21], [22], [23], [24]. The standard diagnostic method are computerized tomography (CT), nuclear magnetic resonance (NMR) and X-rays. Although these consolidated techniques are able to provide extraordinary diagnostic results, some limitations still exist that stimulate the continuous research of new imaging solutions. In this context, MWI can be overcome some limitations of these techniques, such as the ionizing radiations in the CT and X-rays or the disadvantages of being expensive, in the NMR case. This motivates the study of MWI methods and systems, at least as a complementary diagnostic tools.

The aim of electromagnetic diagnostic techniques is to determine physical parameters (such as the electrical conductivity and the dielectric permittivity of materials) and/or geometrics of the objects under test, which are suppose contained within a certain space region, sometimes denoted as "investigation domain". In particular, by means of a properly designed transmitting antenna, the object under test is

illuminated by an electromagnetic radiation. The interaction between the incident radiation and the target causes the so-called electromagnetic scattering phenomena. The field generated by this interaction can be measured around the object by means of one or more receiving antennas, placed in what is sometimes defined as the "observation domain". Starting from the measured values of the scattering field, it is possible to reconstruct the fundamental properties of the test object by solving an inverse electromagnetic scattering problem.

As it is well known, the inverse problem is non-linear and strongly ill-posed, unless specific approximations are used, which can be applied in specific situations.

In several cases, two-dimensional configurations (2D) can be assumed, i.e., the inspected target has a cylindrical shape, at least as a first approximation. Moreover, often the target is illuminated by antennas capable of generating a transverse magnetic (TM) electromagnetic field [25]. These assumptions reduces the problem from a vector and three-dimensional problem to a 2D and scalar one, since it turns out that the only significant the field components are those co-polarized with the incident wave and directed along to the cylinder axis.

In recent years, several methods and algorithms that allow an efficient resolution of the equations of electromagnetic inverse scattering problem have been developed. The proposed approaches can be mainly grouped into two categories: qualitative and quantitative techniques. Qualitative procedures, such as the delay-and-sum technique [26], the linear sampling method [27], and the orthogonality sampling method [28], usually provides reconstructions that allows to extract only some parameters of the targets, such as position, dimensions and shape. However, they are in most cases fast and computationally efficient.On the contrary, quantitative methods allows in principle to retrieve the full distributions of the dielectric properties of the object under test, which allows to also obtain additional information on the materials composing the inspected scenario. Such approaches are often computationally very demanding [25].

Qualitative and quantitative approaches can be combined in order to develop hybrid algorithms [29], [30], [31], [32], [33], [34]. An example is represented by the combination of a delay-and-sum qualitative focusing technique [35], [36], [37] with a quantitative Newton scheme performing a regularization in the framework of the L^p Banach spaces [38], [39], [40].

Holographic microwave imaging techniques are other important qualitative methods. In this case, the processing of data is performed by using through direct and inverse Fourier transforms in order to obtain a map of the inspected target.

As previously mentioned, quantitative approaches aim at retrieving the distri-

butions of the dielectric properties of the scene under test, although they can be significantly more time-consuming especially in 3D imaging. Among them, Newton-type approach are often considered [39], [40].

Recently, artificial neural networks (ANNs) have been considered as powerful tools for quantitative MWI. The first proposed ANNs were developed as shallow network architectures, in which one or at least two hidden layers were considered [41], [42]. Successively, deep neural networks have been proposed, in which more complex fully-connected architecture are adopted. In this framework, Convolutional Neural Networks (CNNs) have been developed as more complex topologies, for classification problems or for solving the inverse scattering problems [43], [44], [45], [46], [47], [48], [49]. In the inverse scattering problems, the CNNs often require a preliminary image retrieved by other techniques [43], [44], [47], [50], [51] and do not allow directly inversion from the scattered electric fields collected by the receiving antennas. Standard CNNs are developed for different applications. Examples are represented by Unet [52], ResNet [53] and VGG [54].

This Thesis is devoted to the application of MWI techniques to inspect the human neck. Several pathologic conditions can affect this part of the body, and a non-invasive and nonionizing imaging method can be useful for monitoring patients. The first pathological condition studied in this Thesis is the cervical myelopathy [55], which is a disease that damages the first part of the spinal cord, between the C3 and C7 cervical vertebrae located near the head [56].

The spinal cord has an important function in the body, since it represents the principal actor in the nervous system. For this reason, it is "protected" inside the spinal canal [57]. A first effect of cervical myelopathy is a reduction of the spinal canal sagittal diameter, which may be caused by different factors [58]. Some patients are asymptomatic and for this reason a continuous monitoring could be very helpful for evaluating the pathology progression. To this end, the application of qualitative and quantitative MWI approaches are proposed in this document.

The second neck pathology studied in this Thesis is the neck tumor, in particular supraglottic laryngeal carcinoma [59], thyroid cancer [60] and cervical lymph node metastases [61]. These kinds of tumors are frequently occurring and shown a 50% 5-year survival probability [61],[62], [63], [64]. Fully-connected neural network are proposed for neck tumor detection.

The Thesis is organized as follows. In Chapter 2, the relevant concepts of the electromagnetic theory are recalled. Chapter 3 describes the developed inversion algorithms. It also reports an extensive validation considering both synthetic and experimental data. Detailed data about the imaging approach based on machine

learning are provided in Chapter 4. This chapter also reports the results obtained in a set of simulations and experiments. Finally, some conclusions are drawn in Chapter 5.

Chapter 2

Electromagnetic Formulation

In this chapter, some fundamental concepts of electromagnetic scattering theory are presented. After the definition of the Maxwell's equations, the electric properties of the materials are discussed, with particular emphasis on the dielectric properties of biological tissues. Then, the inverse scattering problem is addressed, with reference to three-dimensional and two-dimensional configurations. In particular, electromagnetic scattering phenomena in free space and in inhomogeneous environments are described.

2.1 Maxwell Equations

The electromagnetic field is governed by a set of experimental laws known as *Maxwell's equations*, which relate the field vectors to their sources [65]. Maxwell's equation can be expressed in the following local form

$$\nabla \times \bar{\boldsymbol{H}}(\boldsymbol{r}, t) = \frac{\partial \bar{\boldsymbol{D}}(\boldsymbol{r}, t)}{\partial t} + \bar{\boldsymbol{J}}_e(\boldsymbol{r}, t) \tag{2.1}$$

$$\nabla \times \bar{\boldsymbol{E}}(\boldsymbol{r}, t) = -\frac{\partial \bar{\boldsymbol{B}}(\boldsymbol{r}, t)}{\partial t} \tag{2.2}$$

$$\nabla \cdot \bar{\boldsymbol{D}}(\boldsymbol{r}, t) = \rho_e(\boldsymbol{r}, t) \tag{2.3}$$

$$\nabla \cdot \bar{\boldsymbol{B}}(\boldsymbol{r}, t) = 0 \tag{2.4}$$

where $\boldsymbol{r}$ denotes the position vector expressed in meters $[m]$ and t the time in seconds $[s]$. $\bar{\boldsymbol{H}}$ is the *magnetic field vector* $[A/m]$, $\bar{\boldsymbol{D}}$ is the *electric flux density* $[C/m^2]$, $\bar{\boldsymbol{E}}$ is the *electric field vector* $[V/m]$, and $\bar{\boldsymbol{B}}$ the *magnetic induction vector* $[Wb/m^2]$ (or, equivalently, $[T]$). The electromagnetic sources are ρ_e, the *volume electric charge*

density $[C/m^3]$, and $\bar{\boldsymbol{J}}_e$ that is the *electric current density* $[A/m^2]$.

In the follow, we consider harmonic fields. Therefore, the Maxwell's equation can be written as [65]

$$\nabla \times \bar{\boldsymbol{H}}(\boldsymbol{r}) = j\omega\bar{\boldsymbol{D}}(\boldsymbol{r}) + \bar{\boldsymbol{J}}_e(\boldsymbol{r}) \tag{2.5}$$

$$\nabla \times \bar{\boldsymbol{E}}(\boldsymbol{r}) = -j\omega\bar{\boldsymbol{B}}(\boldsymbol{r}) \tag{2.6}$$

$$\nabla \cdot \bar{\boldsymbol{D}}(\boldsymbol{r}) = \rho_e(\boldsymbol{r}) \tag{2.7}$$

$$\nabla \cdot \bar{\boldsymbol{B}}(\boldsymbol{r}) = 0 \tag{2.8}$$

where now the involved vectors represent the phasors of the corresponding time-domain quantities reported in (2.1)-(2.4).

2.2 Electromagnetic Properties of Materials

Maxwell's equations relate the field vectors $\boldsymbol{D}$, $\boldsymbol{E}$, $\boldsymbol{B}$, and $\boldsymbol{H}$ with the sources $\boldsymbol{J}_e$ and ρ_e, which hold true in every electromagnetic phenomenon. However, these equations are not sufficient for determining the vector fields univocally, since can be easily proven [66] that the equations [(2.5)-(2.8)] correspond to six independent scalar equations, whereas the 4 unknown vector fields can be represented by 12 unknown scalar functions. Indeed, Maxwell's equations contain no information on the media in which the electromagnetic phenomena occur. This kind of information is given by the *constitutive equations*, which provide additional constraints among the fields vectors $\boldsymbol{D}$, $\boldsymbol{E}$, $\boldsymbol{B}$, and $\boldsymbol{H}$. The constitutive equations are specified for any medium where the propagation take places [66]. In case a linear, stationary, isotropic, and non-dispersive (in space) medium, the *constitutive equations* can be written as

$$\begin{aligned} \boldsymbol{D}(\boldsymbol{r}) &= \epsilon(\boldsymbol{r})\boldsymbol{E}(\boldsymbol{r}) \\ \boldsymbol{B}(\boldsymbol{r}) &= \mu(\boldsymbol{r})\boldsymbol{H}(\boldsymbol{r}) \end{aligned} \tag{2.9}$$

where ϵ and μ are the dielectric permittivity $[F/m]$ and the magnetic permeability $[H/m]$, respectively. Relative dielectric permittivity and magnetic permeability are often introduced

$$\epsilon_r(\boldsymbol{r}) = \frac{\epsilon(\boldsymbol{r})}{\epsilon_0} \tag{2.10}$$

$$\mu_r(\boldsymbol{r}) = \frac{\mu(\boldsymbol{r})}{\mu_0} \tag{2.11}$$

where $\epsilon_0 \approx 8.85 \times 10^{-12}[F/m]$ and $\mu_0 = 4\pi \times 10^{-7}[H/m]$ denote the dielectric permittivity and the magnetic permeability of the vacuum, respectively.

Some materials exhibit frequency-dependent dielectric properties and a complex permittivity

$$\epsilon(\boldsymbol{r}, \omega) = \epsilon'(\boldsymbol{r}, \omega) - j\epsilon''(\boldsymbol{r}, \omega) \qquad (2.12)$$

Moreover, if inside the material there are free charges, an induced current is generated, that in some case is given by

$$\boldsymbol{J}_{ohm}(\boldsymbol{r}) = \sigma(\boldsymbol{r}, \omega)\boldsymbol{E}(\boldsymbol{r}) \qquad (2.13)$$

where σ is the electric conductivity in [S/m].

Replacing (2.12) and (2.13) in the Ampère equation (2.5), and considering that the total current density is the sum of impressed and inducted ones, was obtain

$$\nabla \times \boldsymbol{H}(\boldsymbol{r}) = j\omega \left(\epsilon(\boldsymbol{r}, \omega) - j\frac{\sigma(\boldsymbol{r}, \omega)}{\omega} \right) \boldsymbol{E}(\boldsymbol{r}) + \boldsymbol{J}_e(\boldsymbol{r}) \qquad (2.14)$$

As a result, it is possible to define an equivalent complex dielectric permittivity

$$\widetilde{\epsilon}(\boldsymbol{r}, \omega) = \epsilon(\boldsymbol{r}, \omega) - j\frac{\sigma(\boldsymbol{r}, \omega)}{\omega} = \epsilon'(\boldsymbol{r}, \omega) - j\left[\epsilon''(\boldsymbol{r}, \omega) + \frac{\sigma(\boldsymbol{r}, \omega)}{\omega} \right]$$
$$= \epsilon'(\boldsymbol{r}, \omega) - j\frac{\sigma_{eq}(\boldsymbol{r}, \omega)}{\omega} \qquad (2.15)$$

where σ_{eq} is an equivalent electric conductivity. $\widetilde{\epsilon}(\boldsymbol{r}, \omega)$ described both the effects of free charges and temporal dispersion.

2.3 Electromagnetic Characterization of Biological Materials

Biological materials exhibit dielectric properties that are strongly dependent upon the working frequency [67]. In particular, the dielectric permittivity values are deeply influenced by their water contents. Consequently, many biological tissues are very lossy, in particular at microwave frequencies, resulting in significant attenuations of the signals [1]. As shown in [68], biological tissues are characterized by three dispersion regions, which are characterized by significant variations in the values of the dielectric properties versus frequencies. The first region, called α *dispersion*, is related to the diffusion mechanism in the cellular membranes and happens between 0.1 kHz and 100 kHz. The β *dispersion* is between approximately 1 MHz and 20 MHz and is related to the presence of bound water in macromolecules, such as proteins. Finally, the γ *dispersion* is mainly due to the polarization of the water molecules

and is located around 20 GHz. Sometimes, a fourth transition region can be defined, called δ *dispersion*, that is present between α and β dispersion regions.

Some examples of the behavior of the real part of the dielectric permittivity and equivalent electric conductivity of some biological tissues in microwave band, are shown in Figure 2.1.

2.3.1 Parametric Models of the Dielectric Properties

As discussed in the previous section, biological tissues exhibit a temporal dispersion behavior, which produces a frequency dependence in the dielectric properties.

To this end, several models can be used for describing the dielectric properties of the materials in computational electromagnetics. In particular, the Debye and the Cole-Cole models are considered in the following.

Debye Model

The Debye model has been introduced in [69] for describing the dielectric properties of polar molecules. Using the Debye model, the complex dielectric permittivity of materials can be approximated with the following parametric formula

$$\widetilde{\epsilon}(\omega) = \epsilon_\infty + \frac{\Delta\epsilon}{1 + j\omega\tau} - j\frac{\sigma_s}{\omega} \tag{2.16}$$

where ϵ_∞, σ_s and τ are real valued parameters that depend upon the specific material. From equation (2.16) it is possible to write the real part of the dielectric permittivity and the equivalent electric conductivity as

$$\epsilon'(\omega) = \epsilon_\infty + Re\left\{\frac{\Delta\epsilon}{1 + j\omega\tau}\right\} = \epsilon_\infty + \frac{\Delta\epsilon}{1 + (\omega\tau)^2} \tag{2.17}$$

$$\sigma(\omega) = \sigma_s - \omega Im\left\{\frac{\Delta\epsilon}{1 + j\omega\tau}\right\} = \sigma_s + \frac{\omega^2\tau\Delta\epsilon}{1 + (\omega\tau)^2} \tag{2.18}$$

When $\omega \to +\infty$, it shows that $\epsilon \to \epsilon_\infty$, whereas, for $\omega \to 0$ we have $\sigma \to \sigma_s$. The two parameters ϵ_∞ and σ_s represent the asymptotic values of the dielectric permittivity and electric conductivity, respectively. Moreover, $\Delta\epsilon = \epsilon_s - \epsilon_\infty$, where ϵ_s is the static dielectric permittivity, since $\epsilon' \to \epsilon_\infty + \Delta\epsilon$ for $\omega \to 0$ [1].

In several cases, the model in (2.16) is not sufficient to accurately describe the dielectric properties over the whole range of frequencies of interest. In order to overcome this problem, the model has been extended considering multiple poles, such

that [70]

$$\widetilde{\epsilon}(\omega) = \epsilon_\infty + \sum_{n=1}^{N} \frac{\Delta\epsilon_n}{1 + j\omega\tau_n} - j\frac{\sigma_s}{\omega} \tag{2.19}$$

where ϵ_∞, σ_s, N, τ_n, and $\Delta\epsilon_n$ are again parameters depending upon the specific material.

Cole-Cole Model

The Cole-Cole model is an extension of Debye model [71], [72]. In particular, the complex dielectric permittivity is described as

$$\widetilde{\epsilon}(\omega) = \epsilon_\infty + \frac{\Delta\epsilon}{1 + j\omega\tau^{(1-\alpha)}} - j\frac{\sigma_s}{\omega} \tag{2.20}$$

where ϵ_∞ is the real value of dielectric permittivity for $\omega \to +\infty$, σ_s is the static electric conductivity, and $\Delta\epsilon = \epsilon_s - \epsilon_\infty$, being ϵ_s the static dielectric permittivity. In this model a new variable α is introduced, which varies between 0 and 1. It is worth noting that, if $\alpha = 0$, the Cole-Cole model reduces to the Debye one.

Also in this case, the model can be generalized considering multipoles. Therefore, the complex dielectric permittivity can be expressed as

$$\widetilde{\epsilon}(\omega) = \epsilon_\infty + \sum_{n=1}^{N} \frac{\Delta\epsilon_n}{1 + (j\omega\tau_n)^{1-\alpha_n}} - j\frac{\sigma_s}{\omega} \tag{2.21}$$

where ϵ_∞ and σ_s represent the asymptotic values of the dielectric permittivity and the electric conductivity, respectively, and $\Delta\epsilon_n$, τ_n, and α_n, with $n = 1, .., N$, are the parameters of the N poles.

2.4 Electromagnetic Scattering: Cylindrical Structures

Let us consider a linear, isotropic, time-invariant and spatially non-dispersive dielectric medium, characterized by a complex dielectric permittivity $\widetilde{\epsilon}_b$ and a magnetic permeability μ_b, with an inhomogeneity inside it that represents the object under test. Considering the hypothesis of non-magnetic materials, i.e., the magnetic permeability $\mu(\boldsymbol{r})$ is always equal to the vacuum value μ_0, the dielectric properties of the object are the dielectric permittivity $\epsilon(\boldsymbol{r})$ and the electric conductivity $\sigma(\boldsymbol{r})$. The considered object is contained in a region of the space, Ω, denoted as the "investigation domain", as showed in Figure 2.2. Moreover, the object is illuminated by a

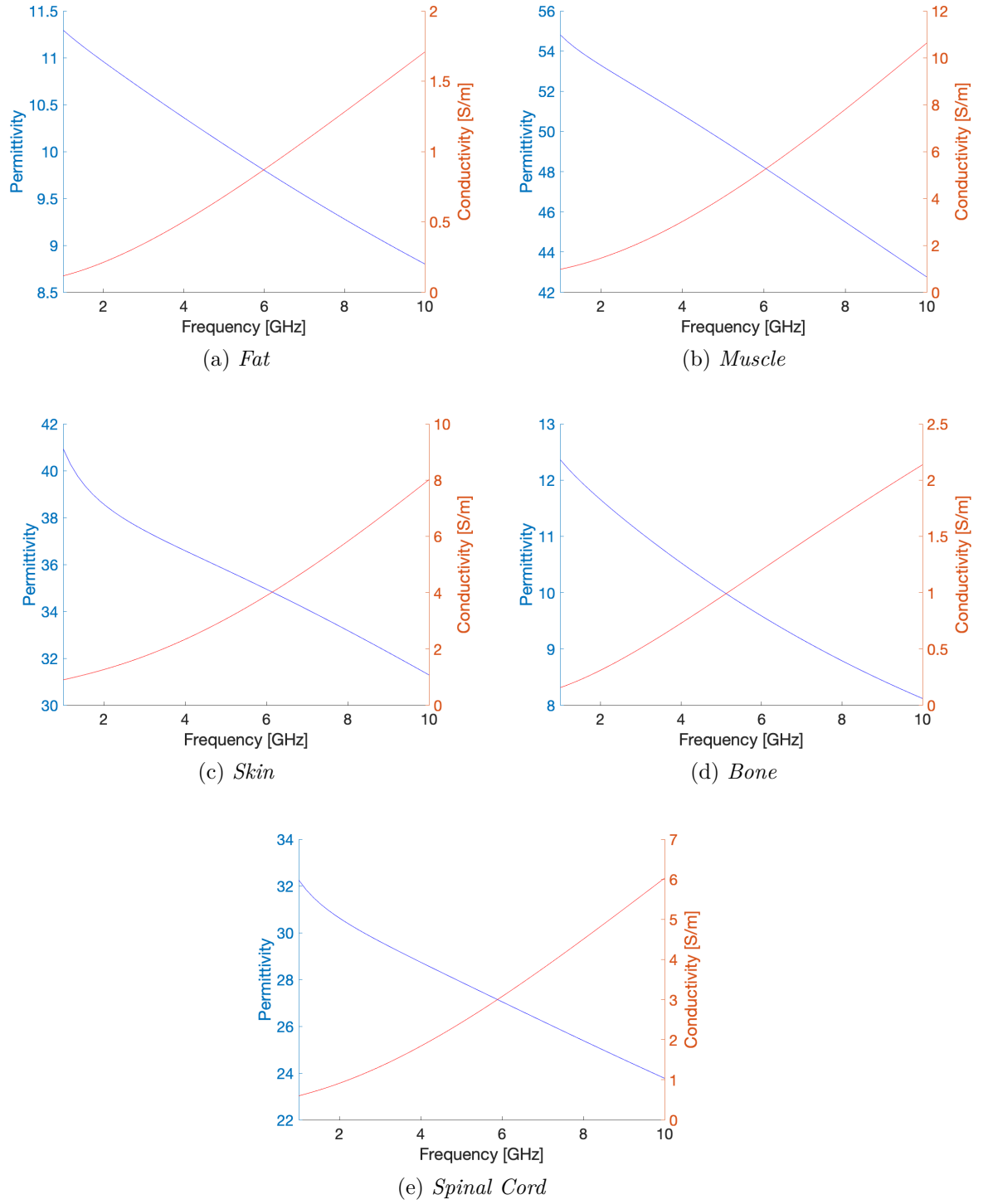(a) *Fat* (b) *Muscle* (c) *Skin* (d) *Bone* (e) *Spinal Cord*

Figure 2.1: Behavior of the real part of relative dielectric permittivity and the equivalent electric conductivity in some biological tissues [73].
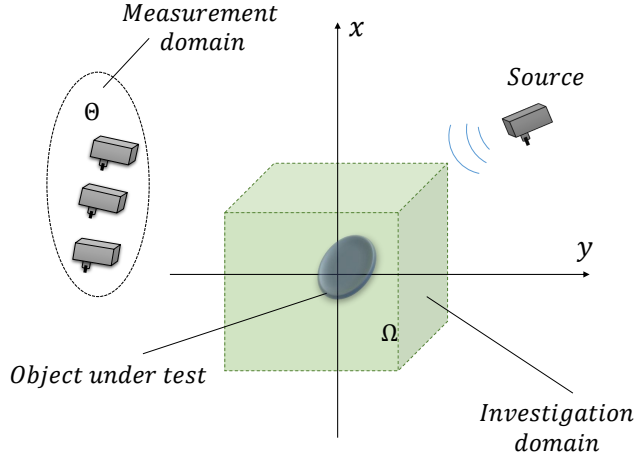
Figure 2.2: Three-dimensional configuration of the electromagnetic scattering problem. The object under test, inside the investigation domain Ω, is illuminated by an electromagnetic source. The scattering field is collected in the measurement domain Θ.

proper source that generates an electromagnetic radiation in the region of interest. Due to the electromagnetic scattering phenomena, the presence of the object modifies the surrounding field. As a result, a "total" electric field $\boldsymbol{E}_t$ is present at any point. If the object is absent, the total field coincides with the incident electric field $\boldsymbol{E}_i$. When the target is present, the difference between the total field and the incident field is usually referenced as the scattered electric field

$$\boldsymbol{E}_s(\boldsymbol{r}) = \boldsymbol{E}_t(\boldsymbol{r}) - \boldsymbol{E}_i(\boldsymbol{r}) \tag{2.22}$$

The scattered electric field $\boldsymbol{E}_s$ can be seen as a fictitious quantity given by the difference between the electric fields with and without the object under test. Usually two situations can occur. In the first case, the object is fully known and the scattered field is to be calculated. This is known as a forward scattering problem. The incident field $\boldsymbol{E}_i$, the values of ϵ_b and μ_b, and the distributions of dielectric properties of the object $\epsilon(\boldsymbol{r})$ and $\sigma(\boldsymbol{r})$ inside Ω are known. The purpose is to derive the scattered fields $\boldsymbol{E}_s$ in such a way to immediately get the total field $\boldsymbol{E}_t$ from equation (2.22).

In the second case, the object is unknown and its dielectric properties have to deduced from the perturbed field measurements, generally collected outside the object. This is called inverse scattering problem. The incident field $\boldsymbol{E}_i$ and the values of ϵ_b and μ_b are known, while the distributions of the dielectric parameter of the object, $\epsilon(\boldsymbol{r})$ and $\sigma(\boldsymbol{r})$, within Ω, are unknown.

11

2.4.1 Wave Equation and Equivalent Sources

The starting point for solving the inverse electromagnetic scattering is represented by the wave equation, which directly derive from Maxwell's equations. Let us consider a homogeneous, isotropic and non-magnetic medium characterized by a complex dielectric permittivity $\widetilde{\epsilon}_b$; in this case, the incident electric field satisfies the following vector wave equation

$$\nabla \times \nabla \times \boldsymbol{E}_i(\boldsymbol{r}) - k_b^2 \boldsymbol{E}_i(\boldsymbol{r}) = -j\omega\mu_0 \boldsymbol{J}_e(\boldsymbol{r}) \tag{2.23}$$

in which $k_b = \omega\sqrt{\widetilde{\epsilon}_b\mu_0}$ is the wavenumber of the background medium, $\boldsymbol{J}_e(\boldsymbol{r})$ is a current density of the source, and ∇ denotes a vector operator defined as

$$\nabla \triangleq \hat{\boldsymbol{x}}\frac{\partial}{\partial x} + \hat{\boldsymbol{y}}\frac{\partial}{\partial y} + \hat{\boldsymbol{z}}\frac{\partial}{\partial z} \tag{2.24}$$

where $\hat{\boldsymbol{x}}$, $\hat{\boldsymbol{y}}$ and $\hat{\boldsymbol{z}}$ represent the unit vectors related to the axes of the Cartesian coordinates x,y and z, such that $\boldsymbol{r} = x\hat{\boldsymbol{x}} + y\hat{\boldsymbol{y}} + z\hat{\boldsymbol{z}}$. Considering the vector identity $\nabla \times \nabla \times \boldsymbol{E}_i = \nabla\nabla \cdot \boldsymbol{E}_i - \nabla^2 \boldsymbol{E}_i$ equation (2.23) can be rewritten as

$$(\nabla^2 + k_b^2)\boldsymbol{E}_i(\boldsymbol{r}) = j\omega\mu_0 \boldsymbol{J}_e(\boldsymbol{r}) + \nabla\nabla \cdot \boldsymbol{E}_i(\boldsymbol{r}) \tag{2.25}$$

Thanks to the Gauss's law for the electric field and the continuity equation, the last term can be expressed as

$$\nabla\nabla \cdot \boldsymbol{E}_i(\boldsymbol{r}) = \frac{1}{\widetilde{\epsilon}_b}\nabla\rho_e(\boldsymbol{r}) = \frac{j}{\omega\widetilde{\epsilon}_b}\nabla\nabla \cdot \boldsymbol{J}_e(\boldsymbol{r}) \tag{2.26}$$

Hence, equation (2.25) becomes

$$\begin{aligned}
(\nabla^2 + k_b^2)\boldsymbol{E}_i(\boldsymbol{r}) &= j\omega\mu_0 \boldsymbol{J}(\boldsymbol{r}) + \frac{j}{\omega\widetilde{\epsilon}_b}\nabla\nabla \cdot \boldsymbol{J}_e(\boldsymbol{r}) \\
&= j\omega\mu_0 \boldsymbol{J}_e(\boldsymbol{r}) + \frac{j\omega\mu_0}{k_b^2}\nabla\nabla \cdot \boldsymbol{J}_e(\boldsymbol{r}) \\
&= j\omega\mu_0\left(\bar{\boldsymbol{I}} + \frac{\nabla\nabla}{k_b^2}\right) \cdot \boldsymbol{J}_e(\boldsymbol{r})
\end{aligned} \tag{2.27}$$

in which $\bar{\boldsymbol{I}}$ denotes the identity dyadic tensor. The solution of equation (2.25) is given by [25]

$$\boldsymbol{E}_i(\boldsymbol{r}) = j\omega\mu_0\int_{\Omega_0}\bar{\boldsymbol{G}}(\boldsymbol{r}|\boldsymbol{r}') \cdot \boldsymbol{J}_e(\boldsymbol{r}')d\boldsymbol{r}' \tag{2.28}$$

where Ω_0 is the volume that contains the source, and

$$\bar{G}(r|r') = -\left(\bar{I} + \frac{1}{k_b^2}\nabla\nabla\right)\frac{e^{-jk_b^2|r-r'|}}{4\pi|r-r'|} \tag{2.29}$$

is the dyadic Green's function for free space [74]. As well know, the dyadic Green's function is the solution of following dyadic equation [25]

$$\nabla \times \nabla \times \bar{G}(r|r') - k_b^2\bar{G}(r|r') = \bar{I}\delta(r-r') \tag{2.30}$$

where δ is the Dirac function. Let us assume that an object is contained inside the investigation domain Ω, the dielectric permittivity is now no more constant and the total electric field $E_t(r)$ everywhere satisfies the following equation [25]

$$\nabla \times \nabla \times E_t(r) - k^2(r)E_t(r) = -j\omega\mu_0 J_e(r) \tag{2.31}$$

where the wave number is equal to $k(r) = \omega\sqrt{\tilde{\epsilon}(r)\mu_0}$. Adding the quantity $k_b^2\mathbf{E}_t(r)$ to both side of the equation (2.31), we obtain

$$\nabla \times \nabla \times E_t(r) - k^2(r)E_t(r) + k_b^2E_t(r) = -j\omega\mu_0 J_e(r) + k_b^2E_t(r) \tag{2.32}$$

that can be written as

$$-\nabla \times \nabla \times E_t(r) + k_b^2E_t(r) = j\omega\mu_0 J_e(r) + \left(k_b^2 - k^2(r)\right)E_t(r) \tag{2.33}$$

At this point you can define the following equivalent current density

$$\widetilde{J_e}(r) = \frac{k_b^2 - k^2(r)}{j\omega\mu_0}E_t(r) = j\omega(\tilde{\epsilon}(r) - \tilde{\epsilon}_b)E_t(r) \tag{2.34}$$

Since outside of the investigation domain $\tilde{\epsilon}(r) = \tilde{\epsilon}_b$, it results that

$$\widetilde{J_e}(r) = 0 \qquad \forall r \notin \Omega \tag{2.35}$$

Considering equation (2.34), it is possible to rewrite equation (2.33) as

$$\nabla \times \nabla \times E_t(r) - k_b^2E_t(r) = -j\omega\mu_0 J_e(r) - j\omega\mu_0\widetilde{J_e}(r) \tag{2.36}$$

Since equation (2.36) represents a wave equation in a homogeneous medium, it can be solved using (2.28). In particular, due to the linearity of Maxwell's equations and assuming that the real source does not is modified by the presence of the object

(electromagnetic decupling), the solution of equation (2.36) can be expressed

$$
\begin{aligned}
\boldsymbol{E}_t(\boldsymbol{r}) &= j\omega\mu_0 \int_{\Omega_0} \bar{\boldsymbol{G}}(\boldsymbol{r}|\boldsymbol{r}') \cdot \boldsymbol{J}_e(\boldsymbol{r}')d\boldsymbol{r}' + j\omega\mu_0 \int_{\Omega} \bar{\boldsymbol{G}}(\boldsymbol{r}|\boldsymbol{r}') \cdot \widetilde{\boldsymbol{J}}_e(\boldsymbol{r}')d\boldsymbol{r}' \\
&= \boldsymbol{E}_i(\boldsymbol{r}) + j\omega\mu_0 \int_{\Omega} \bar{\boldsymbol{G}}(\boldsymbol{r}|\boldsymbol{r}') \cdot \widetilde{\boldsymbol{J}}_e(\boldsymbol{r}')d\boldsymbol{r}'
\end{aligned}
\tag{2.37}
$$

Finally, by recalling equation (2.22), the scattered electric field can be expressed as

$$
\boldsymbol{E}_s(\boldsymbol{r}) = \boldsymbol{E}_t(\boldsymbol{r}) - \boldsymbol{E}_i(\boldsymbol{r}) = j\omega\mu_0 \int_{\Omega} \bar{\boldsymbol{G}}(\boldsymbol{r}|\boldsymbol{r}') \cdot \widetilde{\boldsymbol{J}}_e(\boldsymbol{r}')d\boldsymbol{r}'
\tag{2.38}
$$

On the basis of the previous formulation, the scattered field can be viewed as radiated by an equivalent current density source $\widetilde{\boldsymbol{J}}_e(\boldsymbol{r})$ in free space. It is important to note that equation (2.38) is an expression of the volume equivalence principle [25], because it states that the equivalent source $\widetilde{\boldsymbol{J}}_e(\boldsymbol{r})$ in a homogeneous medium produces the same scattered electric field of the object. Equation (2.38) can be written in an equivalent form as

$$
\begin{aligned}
\boldsymbol{E}_s(\boldsymbol{r}) &= \int_{\Omega} \bar{\boldsymbol{G}}(\boldsymbol{r}|\boldsymbol{r}') \cdot O(\boldsymbol{r}')\boldsymbol{E}_t(\boldsymbol{r}')d\boldsymbol{r}' \\
&= -k_b^2 \int_{\Omega} \bar{\boldsymbol{G}}(\boldsymbol{r}|\boldsymbol{r}') \cdot \chi(\boldsymbol{r}')\boldsymbol{E}_t(\boldsymbol{r}')d\boldsymbol{r}'
\end{aligned}
\tag{2.39}
$$

where $O(\boldsymbol{r}') = \omega\mu_0(\widetilde{\epsilon} - \widetilde{\epsilon}_b)$ and the function

$$
\chi(\boldsymbol{r}') = \frac{\widetilde{\epsilon}(\boldsymbol{r}') - \widetilde{\epsilon}_b}{\widetilde{\epsilon}_b}
\tag{2.40}
$$

is the contrast function containing the information related to the dielectric properties of the object under test. In terms of the contrast function, the equivalent current density is given by

$$
\widetilde{\boldsymbol{J}}_e(\boldsymbol{r}) = j\omega(\widetilde{\epsilon} - \widetilde{\epsilon}_b)\boldsymbol{E}_t(\boldsymbol{r}) = j\omega\widetilde{\epsilon}_b\chi(\boldsymbol{r})\boldsymbol{E}_t(\boldsymbol{r})
\tag{2.41}
$$

2.4.2 The Inverse Scattering Problem

As mentioned above, the inverse problem aims at reconstructing the values of the contrast function $\chi(\boldsymbol{r})$ for $\boldsymbol{r} \in \Omega$ (i.e., in the investigation domain) starting from field measurements collected in a set of points located outside the investigation domain, i.e., the measurement domain Θ. Obviously, only the total electric field $\boldsymbol{E}_t(\boldsymbol{r})$ for $\boldsymbol{r} \in \Theta$ can be measured, but it is immediate to derive the scattered field (equation (2.22)) by subtracting the know incident field $\boldsymbol{E}_i$. As can be seen from equation (2.39), there

are two unknowns, $\chi(\boldsymbol{r})$ and $\boldsymbol{E}_t(\boldsymbol{r})$. Usually, this nonlinear problem is addressed by considering two equations [25]. The first one, usually known as "data equation", relates the scattered field in the measurement domain with the two unknowns and is given by

$$\boldsymbol{E}_s(\boldsymbol{r}) = -k_b^2 \int_\Omega \bar{\boldsymbol{G}}(\boldsymbol{r}|\boldsymbol{r}') \cdot \chi(\boldsymbol{r}')\boldsymbol{E}_t(\boldsymbol{r}')d\boldsymbol{r}', \qquad \boldsymbol{r} \in \Theta \qquad (2.42)$$

The second one is called "state equation" and links the two unknowns with the incident field inside the investigation domain

$$\boldsymbol{E}_t(\boldsymbol{r}) = \boldsymbol{E}_i(\boldsymbol{r}) - k_b^2 \int_\Omega \bar{\boldsymbol{G}}(\boldsymbol{r}|\boldsymbol{r}') \cdot \chi(\boldsymbol{r}')\boldsymbol{E}_t(\boldsymbol{r}')d\boldsymbol{r}', \qquad \boldsymbol{r} \in \Omega \qquad (2.43)$$

As it is well known, the electromagnetic inverse problem is severely ill-posed [25]. It is therefore necessary to adopt appropriate regularization strategies (that will be better detailed in the following).

2.4.3 Scattering Operators

Equations (2.42) and (2.43) can be combined together to write in a compact form the relation between the scattered electric field and the contrast function. To this end, it is possible to define two convolutional integral linear operators

$$\bar{\mathcal{G}}_\Theta \mathbf{f}(\boldsymbol{r}) = -k_b^2 \int_\Omega \bar{\boldsymbol{G}}(\boldsymbol{r}|\boldsymbol{r}') \cdot \mathbf{f}(\boldsymbol{r}')d\boldsymbol{r}', \qquad \boldsymbol{r} \in \Theta \qquad (2.44)$$

and

$$\bar{\mathcal{G}}_\Omega \mathbf{f}(\boldsymbol{r}) = -k_b^2 \int_\Omega \bar{\boldsymbol{G}}(\boldsymbol{r}|\boldsymbol{r}') \cdot \mathbf{f}(\boldsymbol{r}')d\boldsymbol{r}', \qquad \boldsymbol{r} \in \Omega \qquad (2.45)$$

whose kernel is the dyadic Green's function $\bar{\boldsymbol{G}}$. By using equation (2.44), the data equation can be rewritten as

$$\boldsymbol{E}_s(\boldsymbol{r}) = \bar{\mathcal{G}}_\Theta \bar{\chi} \boldsymbol{E}_t(\boldsymbol{r}), \qquad \boldsymbol{r} \in \Theta \qquad (2.46)$$

in which the contrast operator $\bar{\chi}$ is defined as

$$\bar{\chi}\mathbf{f}(\boldsymbol{r}) = \chi(\boldsymbol{r})\mathbf{f}(\boldsymbol{r}), \qquad \boldsymbol{r} \in \Omega \qquad (2.47)$$

Analogously, by applying equation (2.45), the state equation becomes

$$\boldsymbol{E}_t(\boldsymbol{r}) = \boldsymbol{E}_i(\boldsymbol{r}) + \bar{\mathcal{G}}_\Omega \bar{\chi} \boldsymbol{E}_t(\boldsymbol{r}), \qquad \boldsymbol{r} \in \Omega \qquad (2.48)$$

Finally, the total electric field $\boldsymbol{E}_t$ inside the investigation domain can be retrieved from equation (2.48) as

$$\boldsymbol{E}_t(\boldsymbol{r}) = \left(\bar{\mathcal{I}} - \bar{\mathcal{G}}_\Omega \bar{\chi}\right)^{-1} \boldsymbol{E}_i(\boldsymbol{r}), \qquad \boldsymbol{r} \in \Omega \tag{2.49}$$

where $\bar{\mathcal{I}}$ is the identity operator. Then, equation (2.49) can be used to rewrite (2.46) as

$$\boldsymbol{E}_s(\boldsymbol{r}) = \bar{\mathcal{G}}_\Theta \bar{\chi} \left(\bar{\mathcal{I}} - \bar{\mathcal{G}}_\Omega \Omega \bar{\chi}\right)^{-1} \boldsymbol{E}_i(\boldsymbol{r}) = \bar{F}(\chi)(\boldsymbol{r}), \qquad \boldsymbol{r} \in \Theta \tag{2.50}$$

where $\bar{F}$ is the scattering operator.

2.5 Two-dimensional Configurations

If the geometry of the considered problem does not change along one of the spatial coordinates, the electromagnetic problem can be simplified assuming a two-dimensional configuration, as shown in Figure 2.3.

In particular, let us assume that:

1. the contrast function is invariant along the z direction, i.e.,

$$\chi(\boldsymbol{r}) = \chi(\boldsymbol{r}_t) \tag{2.51}$$

where $\boldsymbol{r}_t = x\hat{\boldsymbol{x}} + y\hat{\boldsymbol{y}}$ is the transversal component of $\boldsymbol{r}$ in the (x,y) plane.

2. the incident electric field vector is transverse-magnetic (TM) and z-polarized, i.e.,

$$\boldsymbol{E}_i(\boldsymbol{r}) = E_i(\boldsymbol{r}_t)\hat{\boldsymbol{z}} \tag{2.52}$$

Because of symmetry, also the scattered and total electric fields are z-polarized, i.e., $\boldsymbol{E}_s(\boldsymbol{r}) = E_s(\boldsymbol{r}_t)\hat{\boldsymbol{z}}$ and $\boldsymbol{E}_t(\boldsymbol{r}) = E_t(\boldsymbol{r}_t)\hat{\boldsymbol{z}}$. Under these assumptions, the full vector 3D problem is reduced to a 2D and scalar problem. Equation (2.39) can be now written as

$$E_s(\boldsymbol{r}_t) = -k_b^2 \int_{\Omega_t} g(\boldsymbol{r}_t|\boldsymbol{r}_t')\chi(\boldsymbol{r}_t')E_t(\boldsymbol{r}_t')d\boldsymbol{r}_t' \tag{2.53}$$

where $g(\boldsymbol{r}_t|\boldsymbol{r}_t')$ is the 2D Green's function for the considered configuration.

For the 2D case, the data and state equations can be written as

$$E_s(\boldsymbol{r}_t) = -k_b^2 \int_{\Omega_t} g(\boldsymbol{r}_t|\boldsymbol{r}_t')\chi(\boldsymbol{r}_t')E_t(\boldsymbol{r}')d\boldsymbol{r}_t', \qquad \boldsymbol{r}_t \in \Theta \tag{2.54}$$

$$E_t(\boldsymbol{r}_t) = E_i(\boldsymbol{r}_t) - k_b^2 \int_{\Omega_t} g(\boldsymbol{r}_t|\boldsymbol{r}_t')\chi(\boldsymbol{r}_t')E_t(\boldsymbol{r}_t')d\boldsymbol{r}_t', \qquad \boldsymbol{r}_t \in \Omega_t \tag{2.55}$$
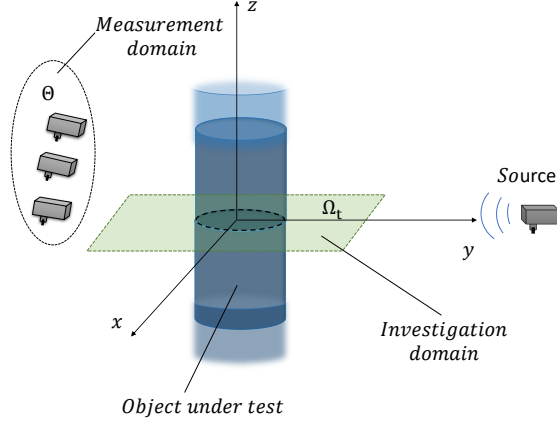
Figure 2.3: Cylindrical configuration. The object under test is an infinite cylinder with the axis parallel to the z axis. The cross section is contained in the investigation area Ω_t. The illuminating field is an electromagnetic TM wave.

where both the investigation area Ω_t and the measurement domain Θ are in the same *(x,y)* plane. In this case, too, the following linear operators can be defined

$$\mathcal{G}_\Theta f(\boldsymbol{r}_t) = -k_b^2 \int_{\Omega_t} g(\boldsymbol{r}_t|\boldsymbol{r}_t')f(\boldsymbol{r}_t')d\boldsymbol{r}_t', \qquad \boldsymbol{r}_t \in \Theta \tag{2.56}$$

and

$$\mathcal{G}_\Omega f(\boldsymbol{r}_t) = -k_b^2 \int_{\Omega_t} g(\boldsymbol{r}_t|\boldsymbol{r}_t')f(\boldsymbol{r}_t')d\boldsymbol{r}_t', \qquad \boldsymbol{r}_t \in \Omega_t \tag{2.57}$$

and it is possible to write the operator equations (2.54) and (2.55) as

$$E_s(\boldsymbol{r}_t) = \mathcal{G}_\Theta \chi E_t(\boldsymbol{r}_t), \qquad \boldsymbol{r}_t \in \Theta \tag{2.58}$$

$$E_t(\boldsymbol{r}_t) = E_i(\boldsymbol{r}_t) + \mathcal{G}_\Omega \chi E_t(\boldsymbol{r}_t), \qquad \boldsymbol{r}_t \in \Omega_t \tag{2.59}$$

Finally, also in the 2D case, a non-linear scattering operator can be defined, and the equation (2.50) can be expressed as

$$E_s(\boldsymbol{r}_t) = \mathcal{G}_\Theta \bar{\chi} \left(\mathcal{I} - \mathcal{G}_\Omega \chi\right)^{-1} E_i(\boldsymbol{r}_t) = F(\chi)(\boldsymbol{r}_t), \qquad \boldsymbol{r}_t \in \Theta \tag{2.60}$$

where $\mathcal{I}$ is the identity operator.

2.5.1 Objects in Free Space

Let us assume that the target under test is located in a homogeneous background characterized by a dielectric permittivity $\widetilde{\epsilon}_b$ (free space) (Figure 2.4). In this case
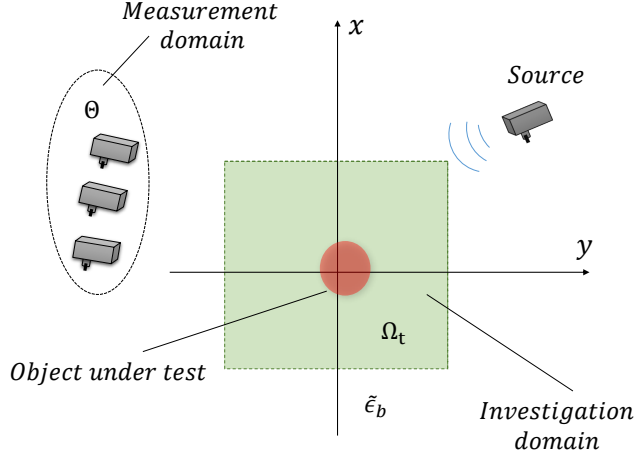
Figure 2.4: Two-dimensional configuration. The object under test is surrounded by an infinite and homogeneous medium, with a dielectric permittivity $\widetilde{\epsilon}_b$ (free space).

the 2D Green function $g(\boldsymbol{r}_t | \boldsymbol{r}_t')$ is equal to [74]

$$g(\boldsymbol{r}_t | \boldsymbol{r}_t') = \frac{j}{4} H_0^{(2)} \left(k_b |\boldsymbol{r}_t - \boldsymbol{r}_t'| \right) \qquad (2.61)$$

where $H_0^{(2)}$ is the zero-order Henkel function of second kind.

2.5.2 Objects in Inhomogeneous Structures

If the target under test is included in an inhomogeneous structure with arbitrary, but known, dielectric properties, an analytic Green's function does not exist (except in particular cases) and must be numerically computed.

To this end, let us consider a reference distribution of the contrast function inside the investigation domain $\hat{\chi}(\boldsymbol{r}_t)$, with $\boldsymbol{r}_t \in \Omega_t$, and a perturbation $\Delta\chi(\boldsymbol{r}_t)$ in the dielectric configuration (corresponding to the target in the inhomogeneous structure), such that

$$\chi(\boldsymbol{r}_t) = \hat{\chi}(\boldsymbol{r}_t) + \Delta\chi(\boldsymbol{r}_t) \qquad (2.62)$$

To solve the inverse problem, it is convenient to search the differential contrast function $\Delta\chi(\boldsymbol{r}_t)$ instead of the total one, since $\hat{\chi}(\boldsymbol{r}_t)$ is known. The scattered field ΔE_s due to the differential contrast function can be expressed as [25]

$$\Delta E_s(\boldsymbol{r}_t) = -k_b^2 \int_{\Omega_t} \hat{g}(\boldsymbol{r}_t | \boldsymbol{r}_t') \Delta\chi(\boldsymbol{r}_t') E_t(\boldsymbol{r}_t') d\boldsymbol{r}_t' \qquad (2.63)$$

where $\hat{g}(\boldsymbol{r}_t|\boldsymbol{r}_t')$ is the Green's function of the inhomogeneous dielectric configuration $\hat{\chi}$, which satisfy the following equation

$$\hat{g}(\boldsymbol{r}_t|\boldsymbol{r}_t') = g(\boldsymbol{r}_t|\boldsymbol{r}_t') - k_b^2 \int_{\Omega_t} \hat{\chi}(\boldsymbol{r}_t'')g(\boldsymbol{r}_t|\boldsymbol{r}_t'')\hat{g}(\boldsymbol{r}_t'|\boldsymbol{r}_t'')d\boldsymbol{r}_t' \qquad (2.64)$$

As can be seen, equation (2.64) is similar to (2.55). For this reason, the same numerical approaches can be used to calculate the total electric field $E_t(\boldsymbol{r}_t)$ in equation (2.55) and the function $\hat{g}(\boldsymbol{r}_t|\boldsymbol{r}_t')$ in (2.64). Now, the electromagnetic inverse problem can be formulated using the following data and state equations

$$\Delta E_s(\boldsymbol{r}_t) = -k_b^2 \int_{\Omega_t} \hat{g}(\boldsymbol{r}_t|\boldsymbol{r}_t')\Delta\chi(\boldsymbol{r}_t')E_t(\boldsymbol{r}_t')d\boldsymbol{r}_t', \qquad \boldsymbol{r}_t \in \Theta \qquad (2.65)$$

$$E_t(\boldsymbol{r}_t) = \hat{E}_t(\boldsymbol{r}_t) - k_b^2 \int_{\Omega_t} \hat{g}(\boldsymbol{r}_t|\boldsymbol{r}_t')\Delta\chi(\boldsymbol{r}_t')E_t(\boldsymbol{r}_t')d\boldsymbol{r}_t', \qquad \boldsymbol{r}_t \in \Omega_t \qquad (2.66)$$

where $\hat{E}(\boldsymbol{r}_t)$ is the total electric field due to the reference configuration $\hat{\chi}$. This field is given by

$$\hat{E}_t(\boldsymbol{r}_t) = E_i(\boldsymbol{r}_t) - k_b^2 \int_{\Omega} g(\boldsymbol{r}_t|\boldsymbol{r}_t')\hat{\chi}(\boldsymbol{r}_t')\hat{E}_t(\boldsymbol{r}_t')d\boldsymbol{r}_t', \qquad \boldsymbol{r}_t \in \Omega \qquad (2.67)$$

where E_i is again the incident field in free space.

2.5.3 Discretization of the Continuous Model

In order to develop numerical algorithms able to solve forward and inverse electromagnetic problems, the scattering equation described in the previous Section must be discretized. The considered 2D geometry is sketched in Figure 2.5. N_a antennas are located around the object under test and are modeled as z-directed infinite line current sources located at points $\boldsymbol{r}_s$, $s = 1, \ldots, S$. Each antenna sequentially illuminates the object under test with a transverse-magnetic (TM) field and the total electric field due to the interaction with the object is collected in the measurement domain Θ composed, for each transmitting antenna, by the remaining at $M = N_a - 1$ antennas, modelled as ideal probes located at points $\boldsymbol{r}_{s,m}$, $m = 1, \ldots, M$. For the sake of simplicity, a single-view and a single-frequency case is described here. In what follows, the indexes $s = 1, \ldots, S$ and $f = 1, \ldots, F$, represent the considered view and frequency, respectively. As shown in Figure 2.5, the investigation domain Ω_t is partitioned into I_{tot} square subdomains R_i, centered at $\boldsymbol{r}_i$, $i = \ldots, I_{tot}$, with side length ρ. With this assumption, the samples of the z-component of the electric field in the measurement domain are related to the dielectric properties of the object
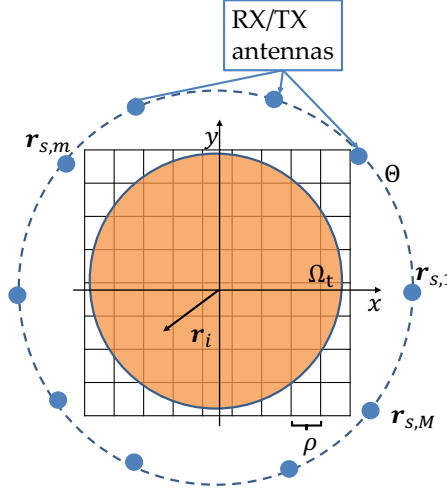
Figure 2.5: Schematic representation of the considered discretized problem.

by means of the following equations [1]

$$\mathbf{E}_t^{s,f} = \mathbf{E}_{ref}^{s,f} + \mathbf{g}_{state}^f \mathsf{diag}(\chi)\mathbf{E}_t^{s,f} \tag{2.68}$$

$$\mathbf{E}_s^{s,f} = \mathbf{g}_{data}^{s,f} \mathsf{diag}(\chi)\mathbf{E}_t^{s,f} \tag{2.69}$$

where $\mathbf{E}_t^{s,f} = [E_t^{s,f,1}, \ldots, E_t^{s,f,I_{tot}}]^T$ and $\mathbf{E}_{ref}^{s,f} = [E_{ref}^{s,f,1}, \ldots, E_{ref}^{s,f,I_{tot}}]^T$ are the arrays containing the z-components of the total and reference electric fields for the sth view and the fth frequency in the investigation domain and $\mathbf{E}_s^{s,f} = [E_s^{s,f,1}, \ldots, E_s^{s,f,M}]^T$ is the array of the z-component of the electric field due to the scattering phenomena at the measurement points. The reference field is due to a given reference configuration when illuminated by the incident electromagnetic field produced by the source. The $\mathbf{g}_{state}^f$ and $\mathbf{g}_{data}^{s,f}$ matrices contain the integrals of the values of the inhomogeneous Green's function for the reference configuration [1]. Finally, the array of the contrast function $\chi = [\frac{\epsilon(\boldsymbol{r_1}) - \epsilon_{ref}(\boldsymbol{r_1})}{\widetilde{\epsilon}_b}, \ldots, \frac{\epsilon(\boldsymbol{r}_{I_{tot}}) - \epsilon_{ref}(\boldsymbol{r}_{I_{tot}})}{\widetilde{\epsilon}_b}]^T$ contains the values of the complex dielectric permittivity of the actual and reference configurations in each subdomain R_i. Combining the equations (2.68) and (2.69), the following equation describing the whole electromagnetic scattering phenomena is defined

$$\mathbf{E}_s^{s,f} = \mathbf{g}_{data}^{s,f} \mathsf{diag}(\chi)[\mathbf{I} - \mathbf{g}_{state}^f \mathsf{diag}(\chi)]^{-1}\mathbf{E}_{ref}^{s,f} \tag{2.70}$$

where $\mathbf{I}$ is an $I_{tot} \times I_{tot}$ identity matrix.

20

Chapter 3

Deterministic Inversion Methods

As introduced in the previous chapter, the considered electromagnetic inverse scattering problem consists in retrieving the contrast function of the object under test, starting from the collected measurements of the electric field in the measurement domain. Therefore, equation (2.60) needs to be solved with respect to the unknown contrast function χ. As mentioned, the relation between the scattered field and the contrast function is strongly nonlinear and ill-posed. For this reason, a proper non-linear regularization approach is required to solve the involved inverse problem.

In the present Thesis, following an approach previously developed at the Applied Electromagnetic Laboratory of DITEN, University of Genoa, a regularization approach based on an *InexactNewton* method is considered, performing a regularization in the framework of *L^p Banach Spaces* [38], [40], [75]. The considered scheme consists in two nested loops: The outer one, iteratively linearizes equation (2.60), whereas in the inner one the linear problem obtained in the previous step is solved by a regularization approach in L^p Banach Space. Figure 3.1 shows the workflow of the considered inversion method through a block diagram.

3.1 Inexact Newton approach (outer loop)

Generally, the equation (2.60) can be written in compact form as

$$F(\chi) = E_s \tag{3.1}$$

The unknown χ belongs to the linear space $\mathcal{C}$, provided with L^p norm. The scattered filed E_s belongs to the linear space D, also provided with L^p norm. F is a non-linear operator so that $F\colon \mathcal{C} \to D$. The developed Inexact-Newton algorithm [76],[77],[78], schematized in Figure 3.1, inverts equation (3.1) through the following
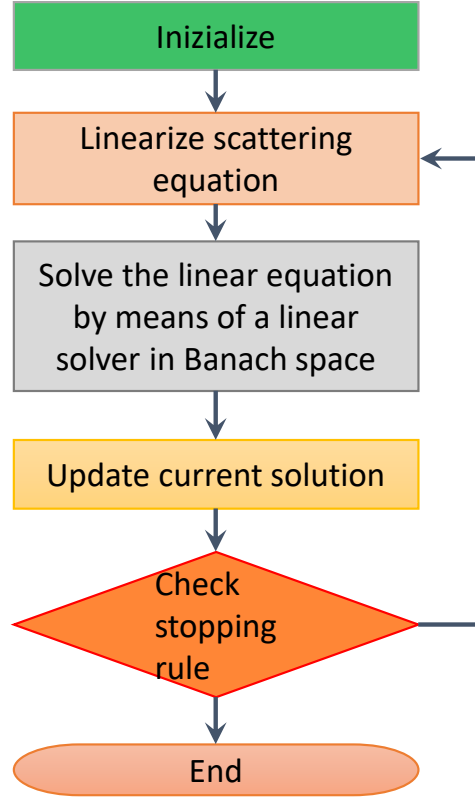
Figure 3.1: Block diagram representing the workflow of the proposed Inexact-Newton inversion scheme.

iterations:

1. Definition of the initial solution χ_0. If a priori information is not available, $\chi_0 = 0$ is used.

2. First-order Taylor expansion of equation (3.1) around the current solution χ_i. The following linear system is obtained [79]

$$F'_{\chi_i} h = E_s - F(\chi_i) = b_i \qquad (3.2)$$

where F'_{χ_i} is the Fréchet derivative of F around the current trial solution χ_i, and b_i is the residual at the ith iteration.

3. Find a regularized solution h of equation (3.2) through a linear algorithm developed in L^p Banach spaces.

4. Update the solution with

$$\chi_{i+1} = \chi_i + h \qquad (3.3)$$

5. If a given stopping rule is satisfied, the algorithm terminates, otherwise repeat from step 2.

As previously introduced, the algorithm belongs to the class of local deterministic methods. Consequently, it may fall into local minima corresponding to false solutions of the inverse scattering problem [80]. To partially overcome this problem, the eventually available a priori information should be used to give an initial solution χ_0 as close as possible to the correct one [81].

3.2   Regularization in Banach Space (inner loop)

The developed Inexact-Newton scheme requires the application of a linear method for the solution of the linear equation obtained in the outer loop. Typically, such solvers are defined in the framework of the L^2 Hilbert space, where it is possible to use standard mathematical tools, such as spectral analysis, to study convergence properties and regularization methods [25], [82], [83], [84]. However, algorithms developed in Hilbert spaces are often characterized by over-smoothness and ringing effects in the obtained solutions, which makes it difficult to recognize small dielectric discontinuities [40], [75], [85]. Therefore, different strategies have been considered. One of the most promising approach is represented by the generalization of the classical solution to L^p Banach spaces, with $p > 1$ [86]. The main novelty is represented by the parameter p, which characterizes the norm of the Banach space. Such a parameter can be tuned in order to mitigate the ringing effects and over-smoothness. On the other hand, the lack of a norm induced by an inner product [87] denies the possibility of defining a singular value decomposition of the linear operators, and, consequently, it is not possible to use standard mathematical tools.

The duality maps represent the key point for the extension of linear solution method to L^p spaces [86], [88]. These are nonlinear functions that associate an element of a generic Banach space $\mathcal{B}$ to an element in its dual space $\mathcal{B}^*$, defined as the space of all the continuous linear functionals from $\mathcal{B}$ to the real value. Beyond the mathematical definition of the duality maps, a heuristic description can be obtained considering the following theorem:

Asplund Theorem. Let $\mathcal{B}$ be a generic Banach space with norm $||\cdot||_{\mathcal{B}}$. The subdifferential of the convex functional $\frac{1}{r}||\cdot||_{\mathcal{B}}^r$ with $r > 1$ is duality map, i.e., $J_B = \partial\left(\frac{1}{r}||\cdot||_{\mathcal{B}}^r\right)$ [86].

In our considered problem, the linear system in equation (3.2) is solved by finding

a regularized solution that minimizes the following functional

$$\frac{1}{2}||F'_{\chi_i}h - b_i||_D^2 \tag{3.4}$$

Applying the chain rule for derivatives, it results that

$$\partial\left(\frac{1}{2}||F'_{\chi_i}h - b_i||_D^2\right) = F'^*_{\chi_i}J_p^D(F'_{\chi_i}h - b_i) \tag{3.5}$$

where $F'^*_{\chi_i}$ is the adjoint operator of F'_{χ_i} and $J_p^D : D \to D^*$, with D^* dual space of D, is the duality map of the considered L^p space. In particular, in the considered settings, J_p^D turns out to be defined as [86], [88]

$$J_p^D(g) = ||g||_D^{2-p}|g|^{p-1}sign(g) \tag{3.6}$$

where $sign(g) = \dfrac{g}{|g|}$, if $g \neq 0$, and $sign(0) = 0$ otherwise.

As it will be seen in the following, the solution methods for the linear equation (3.2) use the quantity at the right member of the equation (3.5) to carry out an iterative update of the solution. In particular, thanks to the application of the duality maps, the updated step is not executed in the contrast functions space, but in its dual one. Once the new estimated solution is obtained in the dual space $\mathcal{C}^*$, the corresponding element in the solution space is obtained by applying the duality map $J_q^{\mathcal{C}^*} : \mathcal{C}^* \to (\mathcal{C}^*)^* \equiv \mathcal{C}$, defined as [86], [88]

$$J_q^{\mathcal{C}^*}(f) = ||f||_{\mathcal{C}^*}^{2-q}|f|^{q-1}sign(f) \tag{3.7}$$

where $q = p/(p-1)$ is the Hölder conjugate of p and $f \in \mathcal{C}^*$. This approach uses a non standard minimization of the functional defined in equation (3.4). In particular, the directions of minimization are not steepest descent ones of the classic methods (i.e., conjugate gradient method), but non standard ones that derive from convex analysis of the Banach spaces. The two approaches are equal only when $p = 2$, that is the case in which the data and unknown spaces are provided with the structure of the Hilbert L^2 space; in fact, the duality maps in the equations (3.6) and (3.7) reduce to identities when $p = 2$. It is important to highlight that has been proven that new method can mitigate the mentioned oversmoothing and ringing issues when $1 < p < 2$ [86].

3.2.1 Conjugate Gradient Method in Lebesgue Space

The classic conjugate gradient exhibits regularizing properties when a proper early stopping of the iterations is adopted, since it behaves as a spectral filter [83]. The conjugate gradient method has been generalized to the L^p Banach space (with $p > 1$) in [89], [90], showing advantages in the reconstruction capabilities with respect to classical approaches. Its superior performance has been shown for the first time in the context of 2D brain stroke microwave imaging (MWI) in [38]. The method is characterized by the following steps:

1. Initialization of $h_0 = 0 \in \mathcal{C}$, $\hat{h}_0 = 0 \in \mathcal{C}^*$ and $\hat{p}_0 = F_{\chi_i}'^* J_p^D(b_i) \in \mathcal{C}^*$.

2. Solution of the following single-variable minimization problem

$$\alpha_k = \underset{\alpha > 0}{\arg\min} \underbrace{||F_{\chi_i}' J_q^D(\hat{h}_k + \alpha \hat{p}_{k-1}) - b_i||_p^2}_{\Phi(\alpha)} \tag{3.8}$$

   This can be solve by a simple one-dimensional optimizer (such as the secant method [91]).

3. Computation of the following parameters

$$\hat{p}_k = -F_{\chi_i}'^* J_p^D(F_{\chi_i}' h_k - b_i) + \beta_k \hat{p}_{k-1}$$
$$\beta_k = \frac{||F_{\chi_i}'^* J_p^D(F_{\chi_i}' h_k - b_i)||_2^2}{||F_{\chi_i}'^* J_p^D(F_{\chi_i}' h_{k-1} - b_i)||_2^2} \tag{3.9}$$

4. Update of the solution in $\mathcal{C}^*$ with

$$\hat{h}_{k+1} = \hat{h}_k + \alpha \hat{p}_k \tag{3.10}$$

5. Update of the solution in $\mathcal{C}$ through

$$h_{k+1} = J_q^{\mathcal{C}^*}(\hat{h}_{k+1}) \tag{3.11}$$

6. If a given stopping rule is satisfied, the process terminates, otherwise repeat from step 2.

3.3 Multi-frequency inversion through frequency hopping

When field measurements are available at F different working frequencies ($f_1 < f_2 < \cdots < f_F$), it is possible to use this information in order to improve the quality of the inversion at single frequency by using the frequency hopping method [92], [93]. In particular, such technique performs several single frequency inversions (in this work the inexact-Newton scheme detailed above is adopted), starting from the data with the lower frequency. The result obtained for a given frequency are then used as initial guess for the subsequent inversion at a higher frequency. Basically, the approach can be schematized as follows.

1. *Initialization.* The frequency hopping scheme is started considering the lowest working frequency f_1. The data at this frequency are inverted. If no a-priori information is available, the starting solution is set to $\chi_0 = 0$. The resulting reconstructed contrast function is indicated as χ_{0,f_1}.

2. *Main loop.* For $v = 2, \cdots, F$, apply the inversion algorithm to the data related to the f_v frequency to obtain a new reconstructed contrast function χ_{f_v}. The initial solution guess χ_{0,f_v} is computed as

$$\chi_{0,f_v} = \Re(\chi_{f_{v-1}}) + j\frac{f_{v-1}}{f_v}Im(\chi_{f_{v-1}}) \tag{3.12}$$

3. *End.* The frequency hopping loop stops when the data at the F-th frequency are processed.

3.4 Hybrid Method: Newton Scheme with Delay-and-Sum Beamforming

Following an approach previously developed at the Applied Electromagnetic Laboratory of DITEN, University of Genoa, the Newton scheme in Lebesgue spaces has also hybridized with a qualitative method based on the delay-and-sum (DAS) beamforming technique [35], [36], [37]. A block scheme of the procedure is shown in Figure 3.2.
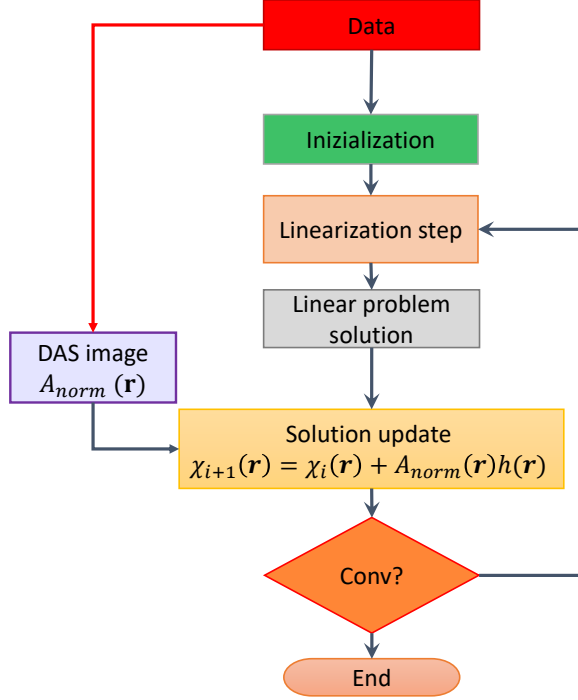
Figure 3.2: Block diagram of the hybrid inversion technique.

Specifically, the data collected in the measurement domain are first processed but using the DAS method. In particular, assuming a multistatic multiview configuration (as better specified in the following), in which the domain is sequentially illuminated by the incident field produced by a different antennas located in a domain Θ_{TX} a preliminary image of the inspected scenario is obtained as

$$A(\boldsymbol{r}) = \int_{\Theta_{TX}} \int_B \int_\Theta E_s(\boldsymbol{r'}, \omega) e^{j\omega\sqrt{\mu_0\epsilon_0\mu_b\epsilon_b}d(r,r',r'')} d\boldsymbol{r'} d\omega d\boldsymbol{r''}, \qquad \boldsymbol{r} \in \Omega \qquad (3.13)$$

where $d(\boldsymbol{r}, \boldsymbol{r'}, \boldsymbol{r''}) = \|\boldsymbol{r} - \boldsymbol{r''}\| + \|\boldsymbol{r'} - \boldsymbol{r}\|$ ($\boldsymbol{r'} \in \Theta$ and $\boldsymbol{r''} \in \Theta_{TX}$ represent the positions of receiving and transmitting antennas, respectively). Moreover, ϵ is the dielectric permittivity of the propagation medium (in the case of inhomogeneous target, an average value is used). Such a preliminary image is then normalized with respect to its maximum value, resulting in a map $A_{norm}(\boldsymbol{r}) = |A(\boldsymbol{r})| / \max_{\boldsymbol{r} \in \Omega} |A(\boldsymbol{r})|$, which is used in the subsequent quantitative reconstruction procedure. $A_{norm}(\boldsymbol{r})$ assumes values near unity in the parts of the domain where significant dielectric discontinuities (with respect to the background) are present, thus allowing an initial identification of target.

The second step of the hybrid approach relies upon the iterative Newton method with a conjugate-gradient-like inner solver in L^p Banach spaces detailed above.

However, differently from the standard Newton scheme, the solution update is weighted by the normalized map obtained in the first step, i.e., the updated solution is computed as

$$\chi_{i+1}(\boldsymbol{r}) = \chi_i(\boldsymbol{r}) + A_{norm}(\boldsymbol{r})h(\boldsymbol{r}) \tag{3.14}$$

In this way, the solution update is focused on the region where the delay-and-sum method finds dielectric discontinuities. In the developed approach, the DAS image obtained in the first step is used only for updating the solution in the iterative Newton method. Since DAS method returns only a qualitative reconstruction and not directly the ϵ_r and σ, it has been chosen to not exploit it in the definition of the initial guess of the inversion. However, it has been found that this approach generates sufficently good results. The iterations are stopped when a proper termination criterion, e.g., based on the maximum number of iterations or on the variation of the residual during subsequent iterations, is satisfied.

3.5   Numerical and Experimental Validation: CG Method

In this Section, a validation analysis concerning the application of the conjugate gradient method is reported. First of all, numerical and experimental phantoms mimicking the human neck are described. They have been designed and realized for assessing the feasibility of the inversion method. Concentric cylinders are used as preliminary simplified neck phantoms, followed by targets with more complex cross sections. Numerical and experimental results are reported to evaluate the capabilities and limitations of the proposed approach and of the adopted microwave measurement system.

3.5.1   Numerical and Experimental Phantoms

As a preliminary numerical neck phantom, concentric circular cylinders are used to describe the various tissues into the neck. The distributions of the relative dielectric permittivities and electric conductivities are shown in Figure 3.3. Such a phantom is composed by five concentric layers with circular cross sections, modeling skin, fat, muscle, bone and spinal cord. The dielectric properties of each tissue have been modeled by using the Debye models in [94], and the corresponding parameters at 1 GHz are reported in Table 3.1. The external diameters of the layers have been set equal to $D_{skin} = 12.8$ cm, $D_{fat} = 12.6$ cm, $D_{muscle} = 9$ cm, $D_{bone} = 3.8$ cm, and $D_{spine} = 1.8$ cm [95].
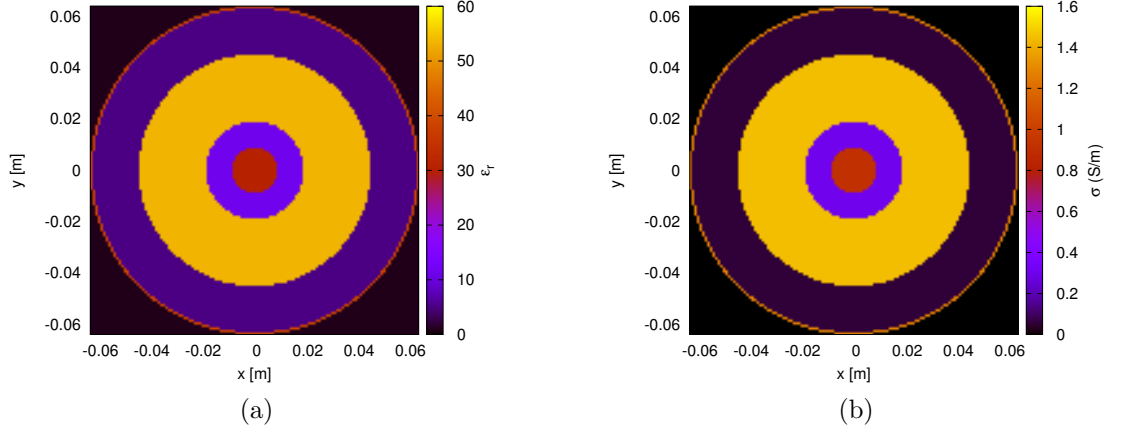
Figure 3.3: Simplified model of the neck used as preliminary phantom. (a) Relative dielectric permittivity and (b) electric conductivity [95].

To improve the complexity of the neck phantom, two different geometries are considered, both numerically and experimentally. The geometry of the phantom, which has been designed on the basis of realistic geometrical shapes reported in [96] and by using the average dimensions reported in [57], is shown in Figure 3.4. The main structure consists of a cylinder with an internal circular inclusion close to the outer border that represents the trachea (Figure 3.4 (a)). The outer boundary has a circular cross section with diameter $d_{out} = 11$ cm and height $h_n = 11$ cm. Internally, a circular compartment with diameter $d_{in} = 9.5$ cm and center in $(-0.175, 0)$ cm has been added. The trachea has inner and outer diameters $d_{in/t} = 1.8$ cm and $d_{out/t} = 2.4$ cm, respectively, both centered at $(-3.9, 0)$ cm (Figure 3.4 (b)). Inclusions of different sizes d_t can be placed inside the structure for modeling the spinal canal ("Phantom 1"). An improved model includes a simplified section of the vertebral column ("Phantom 2"). The shape of this part is sketched in Figure 3.4 (d), and the corresponding dimensions are: $r_1 = 4.23$ cm, $r_2 = 4.31$ cm, $r_3 = 1.3$ cm, $a_1 = 4.8$ cm, $a_2 = 3.9$ cm, $a_3 = 0.6$ cm, and $a_4 = 0.3$ cm. The spinal canal inclusion has an inner diameter $d_{sc} = 1.8$ cm and it is centered at $(0.5, 0)$ cm.

3D printed neck phantoms are developed following the structures of the numerical ones. Polylactic acid (PLA) is used to create the main structure and also as a supporting material for trachea and internal inclusions. The considered dielectric properties of PLA are reported in [97] and the structure is modeled with a relative dielectric permittivity $\epsilon_{r,PLA} = 3$ and an electric conductivity $\sigma_{PLA} = 0.001$ S/m. As a preliminary proof of concept, the phantoms have been filled with glycerin/water mixtures in different concentrations to approximate the average contrast between neck tissues. In particular, a glycerin/water mixture with 70% volumetric content

of glycerin has been used to fill the main structure. The spinal canal has been modeled with an 80% glycerin/water mixture, whereas pure glycerin has been used for the vertebral bone. The dielectric properties of the involved liquids have been obtained by means of reflection coefficient measurements on a liquid-filled section of a short-circuited coaxial line [98]. Table 3.2 reports the parameters of the single pole Debye model obtained by fitting the measured data. As shown in Figure 3.5 (a), the relative dielectric permittivity of the adopted mixture are quite similar to those of the corresponding biological tissues (on the basis of the results reported in [99], [100]), average neck properties are calculated with a concentration of 80% muscle and 20% fat). Figure 3.5 (b) reports the simulated and the actual contrasts between spinal cord and average neck (green line) and between spinal cord and bone (blue line), which also show a good agreement with the mentioned experimental data.

3.5.2 Numerical and Experimental Results

In this Section, numerical and experimental reconstruction results obtained by the application of the proposed inexact-Newton scheme with the conjugate gradient method in L^p Banach spaces (described in the previous chapter) and using the developed phantoms are reported.

First of all, in order to establish suitable working conditions, a planar multilayer model composed by $N = 5$ layers is adopted. The outermost semi-infinite layer, whose relative dielectric permittivity is $\epsilon_{r,b} \in [1, 80]$, represents the the coupling medium outside the neck, whereas the innermost layer is used to model the bone. The coupling medium outside the neck is used to increase the field penetration and to reduce the skin reflection that otherwise could be too large. The three internal layers, representing skin, fat and muscle, have thickness $d_{skin} = 3$ mm, $d_{fat} = 9$ mm and $d_{muscle} = 26$ mm [96]. The innermost semi-infinite layer represents the vertebral bone. The dielectric properties of these tissues are characterized by the

Tissue	Relative dielectric permittivity	Electric conductivity (S/m)
Skin	40.90	0.90
Fat	5.45	0.116
Muscle	54.80	0.98
Bone	12.40	0.16
Spine	32.30	0.60

Table 3.1: Dielectric properties at 1 GHz of the tissues considered in the simplified model of the neck [95].
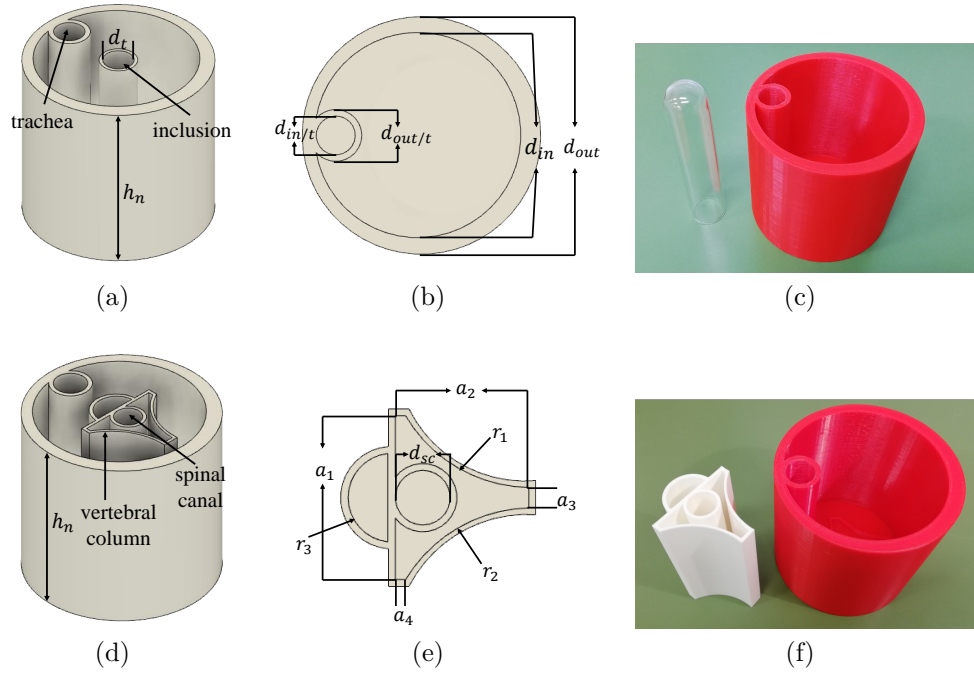
Figure 3.4: Design and dimension of the neck phantoms. "Phantom 1": (a) General view; (b) Top view of the neck model; (c) 3D printed neck phantom with a cylindrical inclusion. "Phantom 2": (d) General view; (e) Top view of the vertebral column model; (f) 3D printed neck phantom with printed model of the vertebral column [101].

Tissue	Glycerin (vol.)	ϵ_∞	$\Delta\epsilon_1$	$\tau_1[ps]$	$\sigma_s[mS/m]$
Avg. neck	70%	12.440	40.157	116.75	127.46
Spinal Cord	80%	10.999	35.360	192.48	135.16
Bone	100%	5.7649	7.1352	187.52	219.74

Table 3.2: Parameters of the first-order Debye models of the glycerin/water mixtures used inside the neck phantom [101].

frequency-dependent Cole-Cole models available in [72]. Such a model is used to evaluate the reflection at the external interface of the neck and the transmission coefficients inside the vertebral bone, versus the working frequency and the dielectric permittivity of the coupling medium. The magnitudes of these two parameters are computed with a custom code based on the analytical formulation reported in [102]. The results are shown in Figure 3.6. As can be seen, the analysis is done with operating frequencies between 300 MHz and 3 GHz. The aim is to find the values of dielectric permittivity of the coupling medium and the working frequency allowing a good trade-off between low reflection from skin and high transmission toward the vertebra. The reflection coefficient, shown in Figure 3.6(a), presents three regions with low values. The first one is located around 300 MHz, when $\epsilon_{r,b} \gtrsim 30$, the second

one is approximately between 500 MHz and 1 GHz, with $5 \lesssim \epsilon_{r,b} \gtrsim 60$, and the third one, which is partially overlapped to second one, is between 1 GHz and 1.8 GHz with $5 \lesssim \epsilon_{r,b} \gtrsim 30$. From 2 GHz onward, a significant reflection appears. Regarding the transmission coefficient, as can be seen in Figure 3.6(b), higher values appear at lower frequencies with $\epsilon_{r,b} \gtrsim 5$. On the basis of these results, the second frequency band and a coupling medium with relative dielectric permittivity $5 \lesssim \epsilon_{r,b} \gtrsim 60$ have been selected [101].

As a very preliminary test, the simplified multilayer cylindrical phantom is adopted for the inversion procedure. Let us start with the description of the illuminating and measurement simulated setup. The background medium is vacuum, which is characterized by the propagation constant $k_b = k_0 = \omega\sqrt{\mu_0\epsilon_0}$. The working frequency is set to 1 GHz without adopting coupling media. A multistatic measurement setup is considered, with $N_a = 16$ antennas uniformly spaced on a circumference of diameter $D_{meas} = 14.8$ cm, surrounding the neck. Each antenna, modeled as a line-current source, acts in turn in transmission mode and the remaining $M = N_a - 1 = 15$ ones are used to collect the scattered electric field. In the numerical simulations, the electric field data used as input data for the inversion procedure have been computed by using forward analytical solutions [103] for multilayer circular cylinders. In order to simulate more realistic imaging conditions, a white Gaussian noise with a zero mean value and a standard deviation corresponding to a signal-to-noise ratio equal to $SNR = 40$ dB has been added to the total electric field of the simulated data. The investigation domain corresponds to the whole neck, i.e., it is a circular area with diameter equal to $d_{\Omega_t} = 12.8$ cm and it is discretized into $I_{tot} = 12645$ square cells of
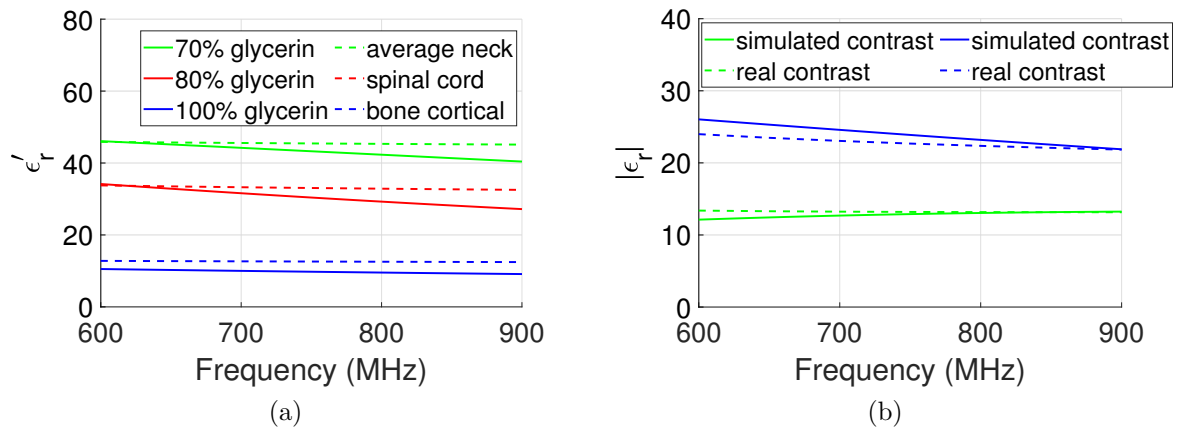
Figure 3.5: (a) Relative dielectric permittivity of biological tissues and glycerin in different concentrations. (b) Real and simulated dielectric contrast between spinal cord and bone (blue line) and between spinal cord and average neck (green line) [101].
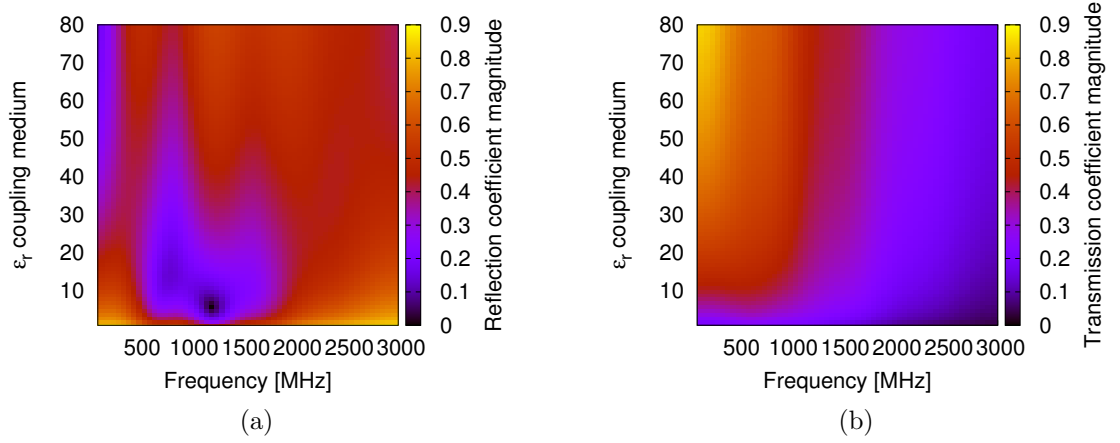
Figure 3.6: (a) Reflection and (b) transmission coefficients for different values of the frequency and of the dielectric permittivity of the coupling medium [101].

side 1 mm. The parameters of the inversion procedure are the following: Maximum number of linearization iterations, $B = 20$; number of inner linear solver iteration, $C = 10$; norm of the data and unknown spaces, $p = 1.4$.

To test the capabilities of the proposed method, two sizes of spinal cord are considered (diameters of the innermost layer: 0.6 cm and 1.8 cm) that represent the pathological and normal condition, respectively. As preliminary test case, the reference scenario is assumed to be the actual neck without the spinal cord and the aim is to retrieve the dielectric discontinuities represented by the spinal cord. The results obtained by applying the inversion procedure are shown in Figure 3.7. Such figures report the distributions of the normalized amplitude of the retrieved differential contrast function, i.e., $I(\boldsymbol{r}) = |\chi(\boldsymbol{r})|/\max_{\boldsymbol{r} \in \Omega_t} |\chi(\boldsymbol{r})|$. In the reported cases,
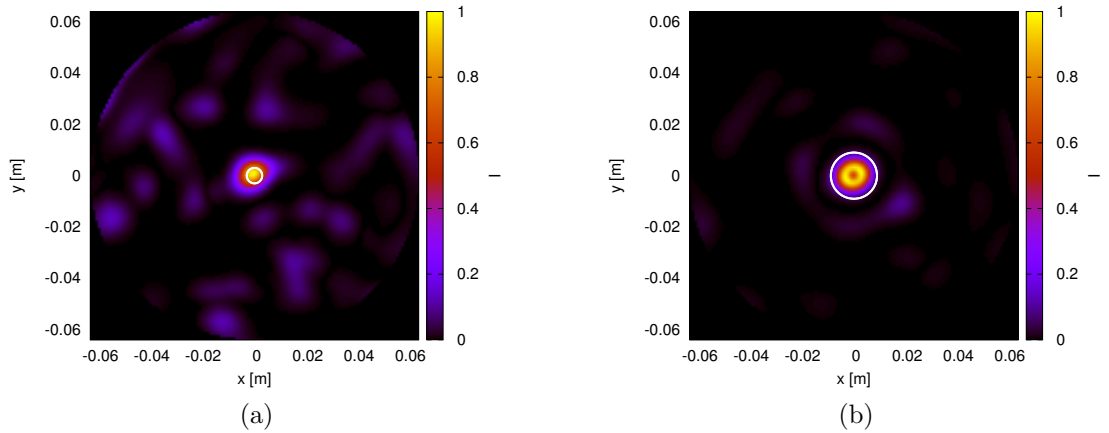
Figure 3.7: Reconstruction images for two sizes of the spinal cord: (a) 0.6 cm and (b) 1.8 cm. Normalized values of the differential contrast function [95].
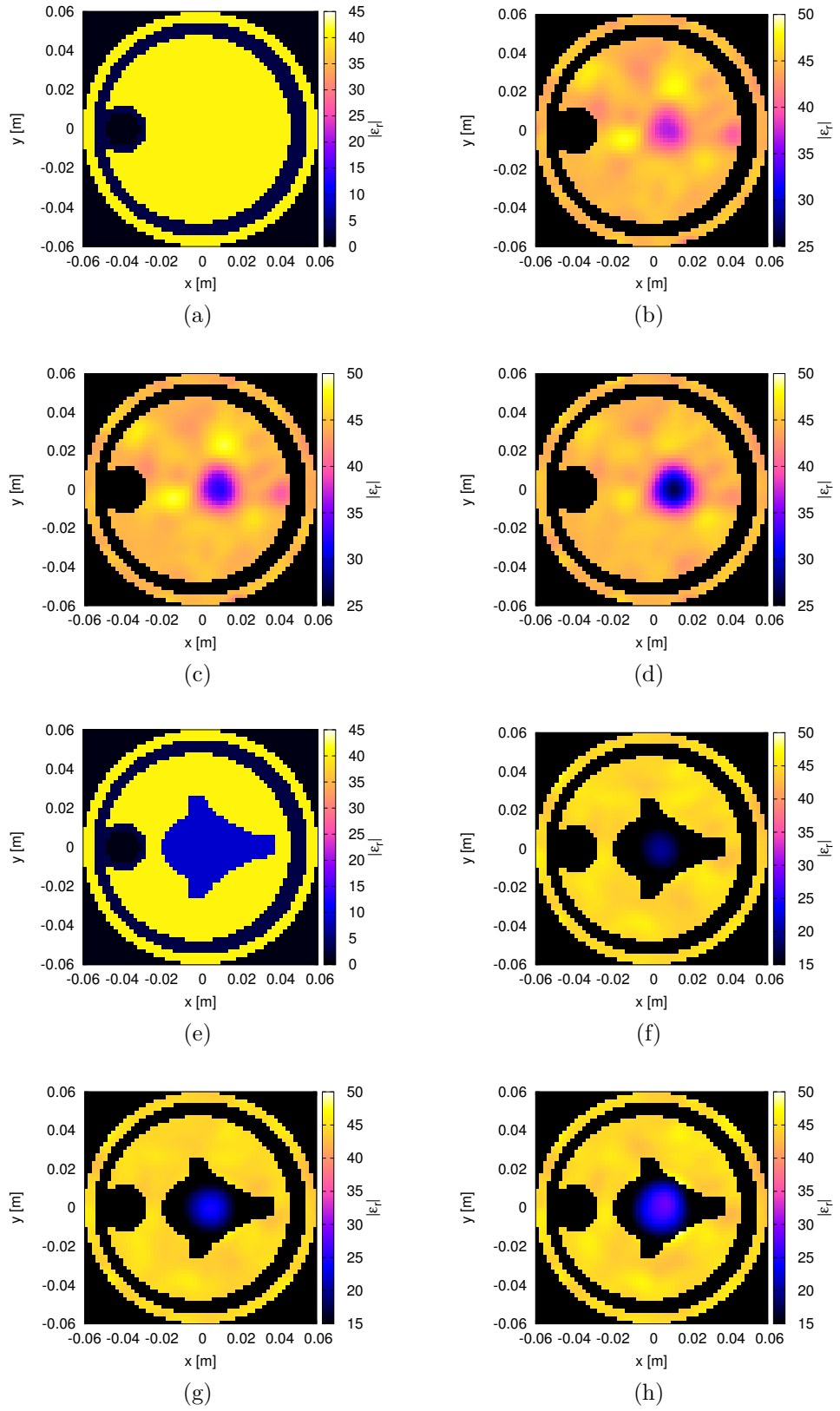
Figure 3.8: Reconstructed relative dielectric permittivity for different diameters of the spinal canal d_t. "Phantom 1": (a) $d_t = 1.4$cm, (b) $d_t = 1.8$ cm and (c) $d_t = 2.4$ cm. "Phantom 2": (a) $d_t = 1.4$ cm, (b) $d_t = 1.8$ cm and (c) $d_t = 2.4$ cm [101].

the size of the inclusion can be identified with a reasonable accuracy (withe circles represent the correct diameters), although some artifacts appear for the smallest considered diameter.

Finally, the inversion procedure has been numerically tested by using the more complex neck phantoms, which have been described in the previous section. The capabilities of the inverse procedure are tested by means of numerical simulations involving the numerical model shown in Figure 3.4 (a)-(b) ("Phantom 1"). The dielectric properties of the simulated phantom are characterized by using the Debye model reported in Table 3.2. The measurement system is composed by $N_a = 10$ antennas with $D_{meas} = 12.8$ cm. The frequency range is between 600 and 900 MHz, with a frequency step of 50 MHz. A 2D simulator based on the method of moment is used for performing the forward simulation [104]. In this case, we assume a $SNR = 35$ dB added to the total electric field and an investigation domain constituted by a circular region with diameter $d_{\Omega_t} = 12$ cm, which is discretized into $N_f = 11304$ square cells of 1 mm in side. For the inversion procedure, the following parameters are considered: $I_{tot} = 2828$ square cells of side 2 mm; $p = 1.4$; $B = 20$; $C = 10$; and the residual threshold is equal to $R_{th} = 0.01$. Also in this case, the reference scenario is the actual neck without the spinal canal [Fig. 3.8 (a)]. Three different diameters of the spinal canal d_t are considered: 1.4 cm, 1.8 cm, and 2.4 cm. Figures 3.8 (b)-(d) show the distributions of the reconstructed dielectric properties (in particular, the value of $|\epsilon_r|$) at 900 MHz for the considered test cases. The aim of this inital test was to evaluate the cabability of the proposed method to reconstruct different value of spinal cord diameter. For this reason, in the figures the modulus of dielectric permittivity, $|\epsilon_r|$, is shown. The estimated diameters of the spinal cord, calculated with a threshold value corresponding to 45% of the actual contrast between the dielectric values of the spinal cord and the average neck, are 1.66 cm, 2.19 cm, and 2.58 cm, respectively. Such values are very close to the actual ones and allow distinguishing between the different canal sizes. As a second test case,
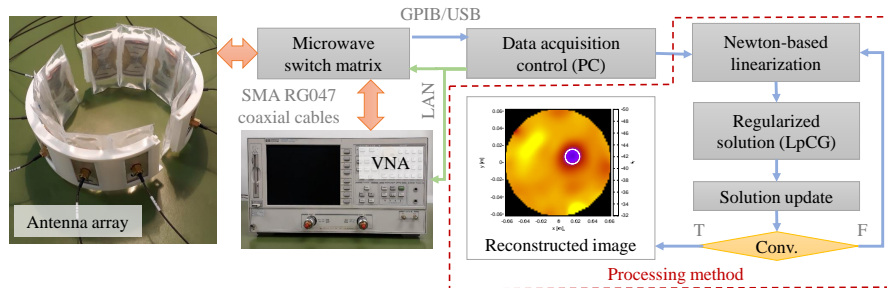
Figure 3.9: Structure of the proposed microwave imaging system [101]

the more complex "Phantom 2" (Figure 3.4 (d)-(e)), containing the simplified model of the vertebral column, is investigated. As in the previous case, the same values for the diameter of the spinal canal are assumed, i.e., 1.4 cm, 1.8 cm, and 2.4 cm. In this case, the reference scenario is the actual neck with the vertebra and without the spinal cord [Fig. 3.8 (e)], whereas the inversion parameters are the same as in the previous simulation. The distributions of the reconstructed dielectric properties are reported in Figure 3.8 (f)-(h). The estimated diameters are 1.58 cm, 2.27 cm and 2.88 cm, respectively. Also in this case, it is possible to distinguish between the pathologic condition and the normal one.

Moving to the experimental results, let us introduce the proposed microwave imaging system developed at the Applied Electromagnetics Laboratory of DITEN, University of Genoa. The system processes the scattered-field data acquired with a vector network analyzer (VNA) by means of a non linear inverse scattering technique, and provides an image of the neck cross section. The structure of the prototype is shown in Figure 3.9, where both the measurement instrumentation and the processing scheme are highlighted. A two-port VNA is used for performing measurements in a multistatic way, i.e., a single antenna radiates at a time and all the other ones are subsequently swept to obtain multiview data. A microwave switch matrix is inserted between the VNA and the antennas. The switch is controlled by MATLAB R2019a (The MathWorks, Natick, MA, USA). In particular, $N_a = 10$ slotted bowtie-like antenna elements with back cavity realized on a FR-4 substrate are used. Details about these antennas can be found in [38]. The number of antennas has been chosen as a trade-off between the minimum number of sampling point and the available space around the neck. The antennas are supported by a modular 3D printed assembly of

(a)	(b)
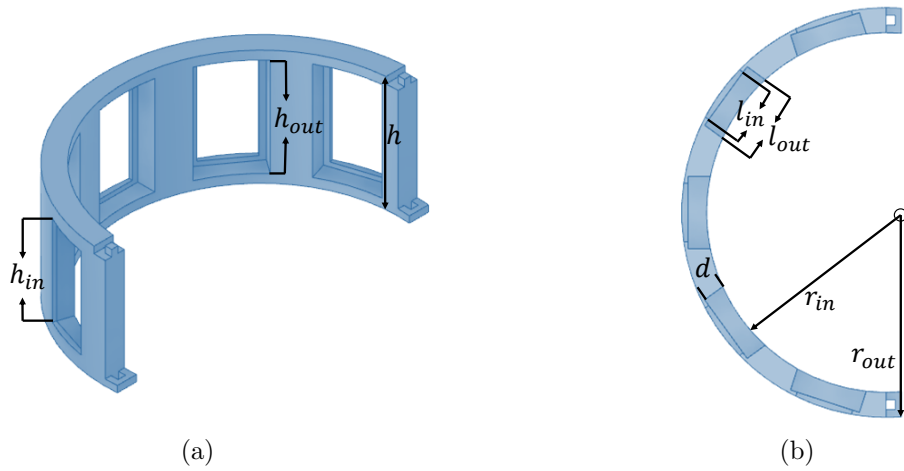
Figure 3.10: Design parameters of a section of the 3D printed antenna support structure. (a) Side view. (b) Top view.
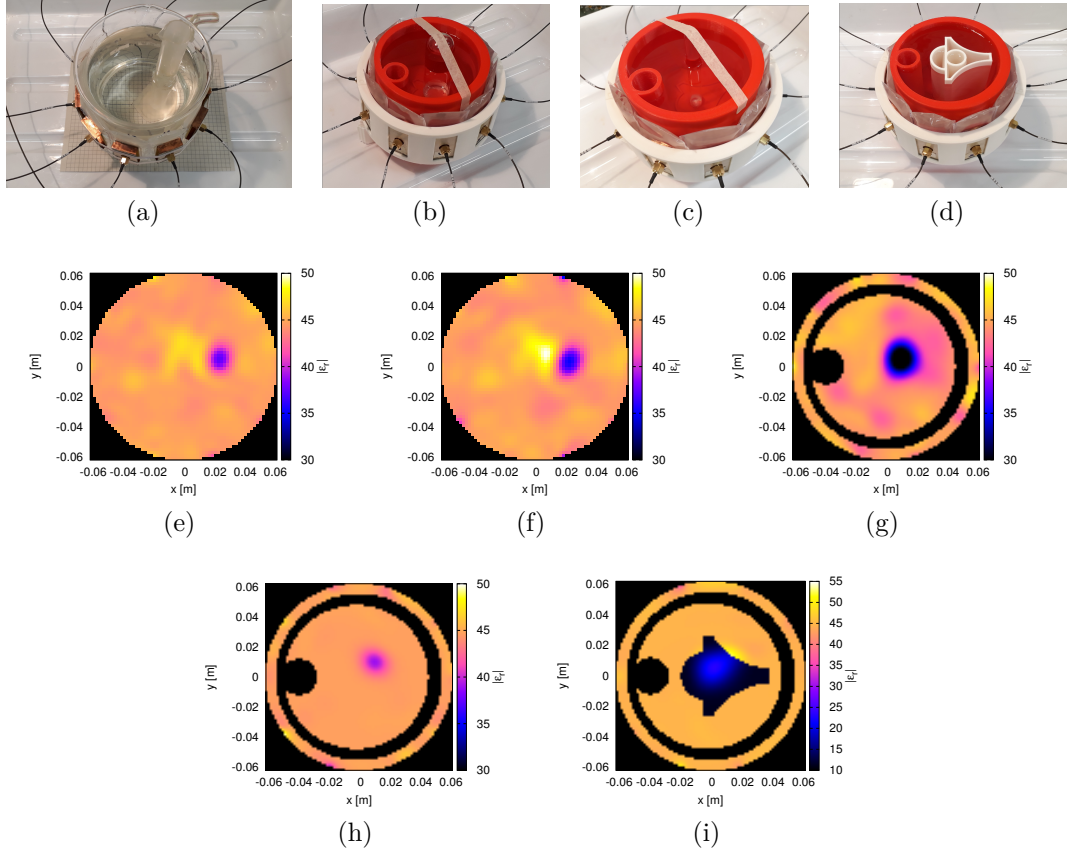
Figure 3.11: Experimental target: (a) Simplified beaker; "Phantom 1" with (b) a large and (c) a small inclusions; (d) "Phantom 2". Reconstructed relative dielectric permittivity: Simplified beaker with (e) a small and (f) a middle-size inclusions; "Phantom 1" with (g) large and (h) small inclusion; (i) "Phantom 2" [101].

PLA having the shape of a circular collar containing N_a holes where the antennas are located. The dimensions of the antenna support structure are reported in Figure 3.10. In particular, with reference to the elements specified in the figure, it results: $h_{out} = 4.2$ cm, $h_{in} = 4.2$ cm, $l_{out} = 2.6$ cm, $l_{in} = 2.1$ cm, and $d = 0.8$ cm. The whole assembly is composed of two equal parts with height $h = 5.4$ cm, and with inner and outer radii equal to $r_{in} = 6.45$ cm and $r_{out} = 7.35$ cm, respectively. These parts are hooked with two joints that should allow quite a comfortable application on the patient's neck. The coupling between the probing elements and the neck is ensured by plastic bags filled with a matching medium placed in contact with the radiating surface of each antenna. The adopted matching medium, which is enclosed in sealed polyethylene bags, is a mixture of glycerin and water, with 70% volumetric content of glycerin. As mentioned, the bags are placed in contact with the radiating surfaces of the antennas and are also able to compensate for variations in neck size.

Some preliminary experimental results are provided in Figure 3.11. Initially, the

MWI system and the applied inversion procedure are assessed by using the simplified phantom shown in Figure 3.11(a), called in the follow "Beaker". It is composed of a circular glass beaker with external diameter $d_b = 10.7$ cm, which is filled with a 70% glycerin/water mixture. Circular inclusions filled with an 80% glycerin/water mixture are placed inside the beaker in order to simulate the presence of the spinal canal. The described microwave system is used to collect measurement data in the frequency range between 600 and 900 MHz, with a frequency step of 50 MHz frequency step. The measured data are used by inversion approach (described in the previous chapters) and using a frequency-hopping scheme. In this case, the total and incident electric fields used in the inversion method are obtained from the acquired S parameter after a calibration procedure [105]. In particular, for each case, a complex scaling coefficient is computed by considering the measurements of the incident field performed in a known condition. The reference configuration is represented by a homogeneous cylinder with the dielectric properties of a 70% glycerin/water mixture. For the inversion procedure, the region of interest has a diameter $d_{\Omega_t} = 12.2$ cm and is partitioned into $I_{tot} = 3024$ square cells of side 2 mm. The following inversion parameters are used: $p = 1.4$, $B = 20$, $C = 10$, $R_{th} = 0.01$. Two different diameters of the inclusion model of the spinal canal are considered: $d_{g1} = 1.24$ cm and $d_p = 1.69$ cm. The reconstructed distributions of the contrast function magnitudes for the two cases are shown in Figure 3.11(e) and Figure 3.11 (f), respectively. In both experimental cases, the internal cylinder is reconstructed quite accurately and the estimated diameters are 1.03 cm and 1.58 cm, respectively. Moreover, the differences between the two inclusions of different diameters can be clearly deduced from the reconstructed images.

Subsequently, the imaging setup has been tested by using the 3D printed neck phantom. Initially, the simplified structure denoted as "Phantom 1" is adopted. As shown in Figure 3.11 (b) and Figure 3.11 (c), two different diameters of the inclusions, i.e., $d_{g2} = 2.4$ cm and $d_{g3} = 1.0$ cm, are considered again. The investigation domain has a diameter of $d_{\Omega_t} = 12.4$ cm and it is partitioned into $I_{tot} = 5024$ square cells of side length equal to 1.5 mm. The printed phantom without inclusions has been used as reference model and the inversion parameters for the first inclusion are: $p = 1.4$, $B = 20$, $C = 10$, $R_{th} = 0.2$. For the second case, $p = 1.2$, whereas the other parameters are the same as in the previous example. The reconstructed distributions are in Figure 3.11 (g) and Figure 3.11 (h), respectively. The sizes of the inclusion are quite correctly identified in both cases (the estimated diameters are 2.74 cm and 0.72 cm, respectively), confirming that even when using a more complex structure, it is still possible to distinguish between the two different inclusions on the basis of

their sizes.

The last considered configuration is based on the more accurate "Phantom 2", which is shown in Figure 3.11 (d). The vertebral bone is filled with pure glycerin and the internal inclusion is filled with a 80% glycerin/water mixture to simulate the spinal canal, which has a diameter of 1.8 cm. The investigation domain is the same used in the previous cases and the considered reference scenario is a numerical model of the phantom with the vertebral section filled with pure glycerin. The inversion parameters are the same as before. The reconstructed distributions of the dielectric permittivity are reported in Figure 3.11 (i). Although the increased complexity of this phantom leads to a slight decrease in the reconstruction accuracy (the estimated diameter is 2.25 cm), it confirms the possibility of identifying the inclusion even in this more challenging case. Also in these preliminary experimental results the aim was to evaluate the cabability to individuate different diameter values; the distribution of $|\epsilon_r|$ have been considered.

3.6   Experimental Validation: Hybrid Method

In this Section, some preliminary results concerning the validation of the hybrid approach that combines the DAS method with the Newton scheme (which has been described in section 3.4) are reported and discussed.

The simplified phantom described in the previous Section and referred as "Beaker" is considered. This phantom is composed by a circular glass beaker with diameter $d_b = 10.7$ cm and filled with a mixture of water and 70% glycerin by volume. Two test cases are considered, with two different inner inclusions. The first one includes an additional circular glass pipe with diameter $d_{g1} = 12.4$ mm, which is filled with a mixture of water and 80% glycerin by volume. The dielectric properties of the considered mixtures, at a frequency of 800 MHz, are equal to $\epsilon_{80\%} = 29.26 - 20.71$ and $\epsilon_{70\%} = 42.31 - 20.39$, respectively. The microwave system used to acquire the data is the same that has been described in the previous Section. Data are collected in the frequency band ranging from 600 MHz to 800 MHz, with a frequency step of 50 MHz. The investigation area has a circular shape with a diameter $d_{\Omega_t} = 12.4$ cm. The domain is discretized into $I_{tot} = 3024$ square cells of side equal to 2 mm. The considered reference scenario is the mentioned phantom without the spinal cord inclusion. For the inversion procedure, the following parameters of the method are used: $p = 1.3$, $R_{th} = 0.1$, $B = 20$, and $C = 10$.

Figure 3.12 (a) shows a reconstructed qualitative image obtained by applying the DAS method. As can be seen, the DAS technique is able to identify the presence of
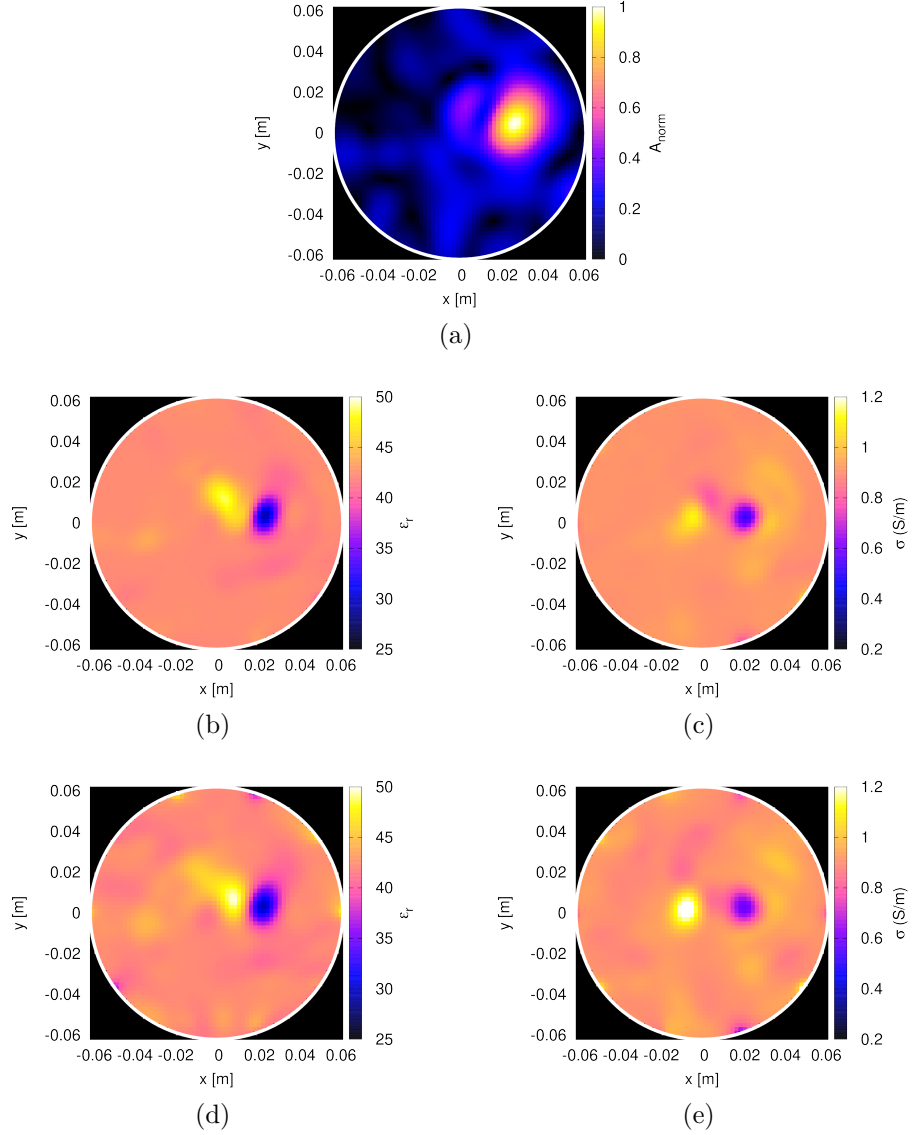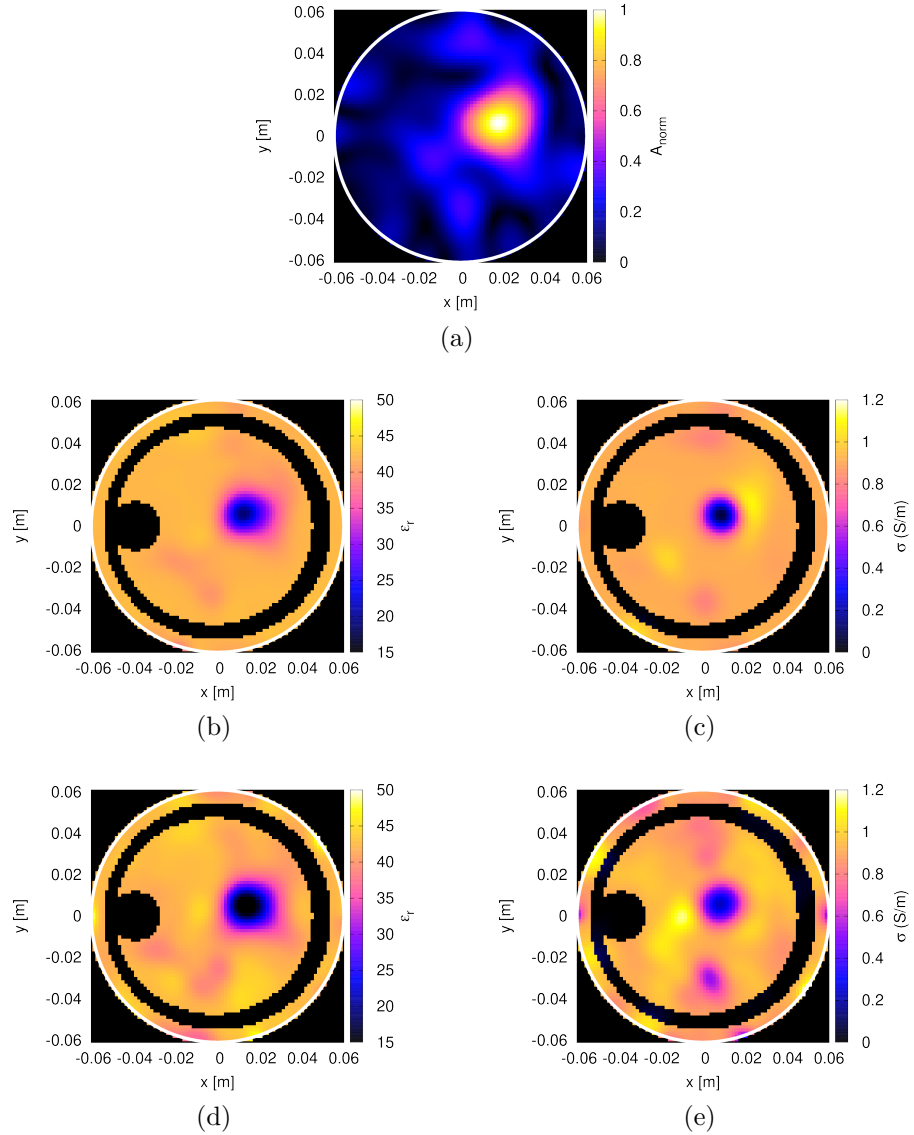
39
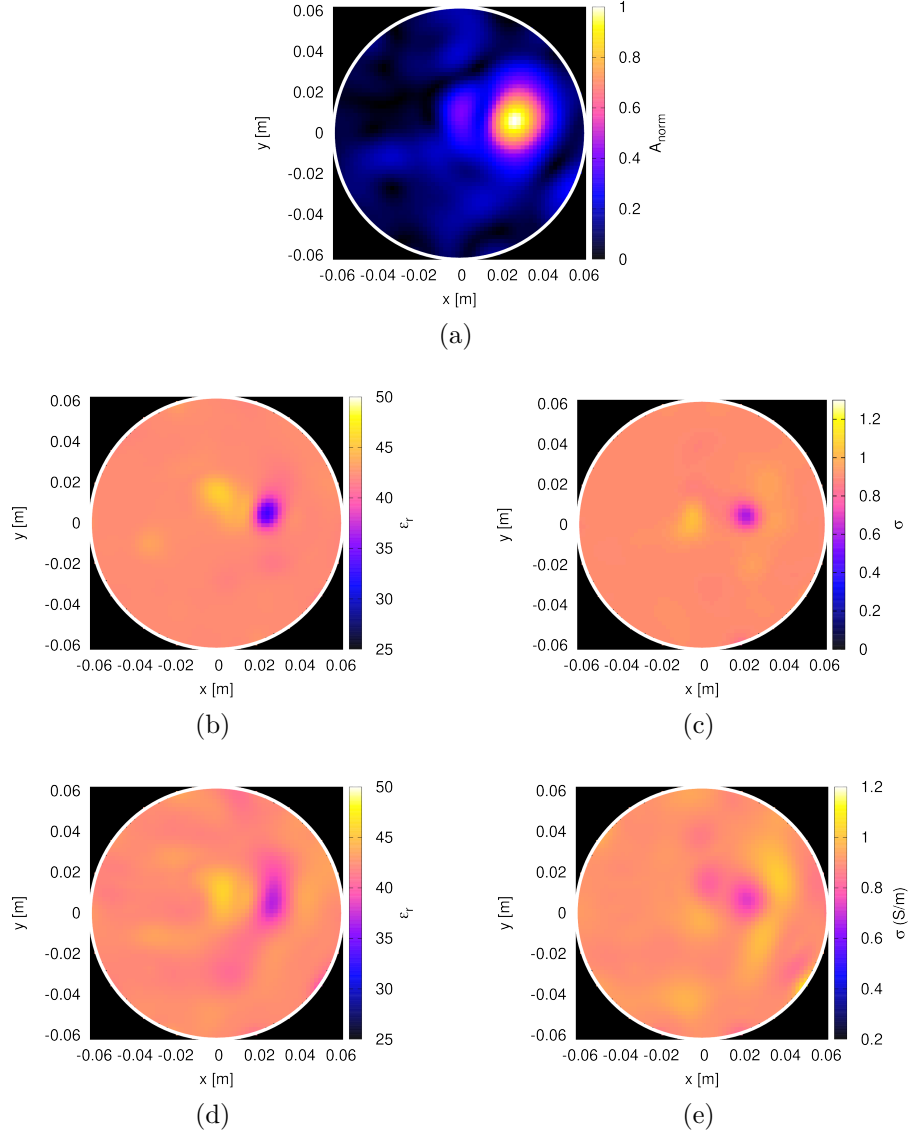
Figure 3.12: "Beaker" phantom with glass inclusion with $d_{g1} = 12.4$ mm. (a) Qualitative image provided by the DAS method. Reconstructions obtained by using the hybrid method (800 MHz). (b) Relative dielectric permittivity and (c) electric conductivity ($p = 1.3$), (d) relative dielectric permittivity and (e) electric conductivity ($p = 2.0$. Hilbert space) [106].

the inclusion and its position, although the size is largely overestimated, and artefacts affect the background region. Such an image allows guiding the inversion process in the second step in an effective way, by focusing the updates mainly in the region where the inclusion is detected. This results in an enhanced capability of reducing artefacts outside the inclusion, which in turn allows a better estimation of its dielectric properties. The reconstruction results obtained by applying the proposed hybrid method are provided in the other figures. In particular, Figure 3.12 (b)-(c) report the reconstructed distributions of the relative dielectric permittivity and of the electric

Norm parameter, p	Estimated diameter [cm]
1.1	0.87
1.2	1.11
1.3	1.26
1.4	1.46
1.5	1.49
1.6	1.55
1.7	1.68
1.8	1.76
1.9	1.77
2.0	1.74

Table 3.3: Estimated diameter of the inclusion versus the norm parameter p [106].

conductivity with a norm parameter $p = 1.3$, whereas the reconstructions in Figure 3.12 (d)-(e) are obtained in the Hilbert space, i.e., with $p = 2.0$. The reconstructions with $p = 1.3$ exhibit a good target localization, different from the ones obtained in the Hilbert-space, in which a certain over-smoothing is present in the inclusion region.

For completeness, the hybrid method has been tested for different values of the norm parameter (in the range $[1.1, 2]$). The reconstructed values of the diameter of the spinal canal are calculated for each norm value. A threshold equal to $0.5 \max |\epsilon_{r,rec} - \epsilon_{r,ref}|$ is used, where $\epsilon_{r,rec}$ and $\epsilon_{r,ref}$ are the relative dielectric permittivities of the reconstructed and actual configuration, respectively. The obtained results are reported in Table 3.3. As can be seen, the value of the norm parameter significantly influences the reconstruction quality. For the considered case, the "optimal" norm value is $p = 1.3$, for which the inner estimated diameter is equal to 1.26 cm. For smaller norm values, the size of the inclusion is underestimated, whereas for higher values the diameter is significantly overestimated (due to the increased oversmoothing of the reconstructed images). Indeed, low values of the norm parameter p enhance the sparsity of the solution and thus improve the reconstruction of small and localized targets.

The second inclusion is a plastic pipe with diameter $d_p = 16.9$. The pipe is filled with the same mixture as the previous case. The obtained DAS image is shown in Figure 3.13 (a). In this case, too, the method is able to detect the inclusion region. A comparison between the hybrid method and quantitative method alone, with the same parameter p, has been performed, too. In Figure 3.13 (b)-(c) the reconstructions of the relative dielectric permittivity and electric conductivity are provided, respectively, whereas in Figure 3.13 (d)-(e) the reconstructed images obtained with the quantitative

Figure 3.13: "Beaker" phantom with plastic inclusion with $d_p = 16.9$ mm. (a) Qualitative image provided by the DAS method. Reconstructions obtained (800 MHz and $p = 1.3$) by using the hybrid method, (b) relative dielectric permittivity and (c) electric conductivity. Reconstructions obtained by using the quantitative method alone, (d) relative dielectric permittivity and (e) electric conductivity [106].

method alone are reported. As can be seen, the hybrid method allows a better reconstruction of the background, both for ϵ_r and σ.

Finally, other two test cases are proposed. In particular, "Phantom 1" and "Phantom 2" are used. These phantoms have been described in details in the previous section. Firstly, "Phantom 1" is considered, in which a glass inclusion with diameter $d_{g2} = 24$ mm is present. The DAS image obtained in this case is reported in Figure 3.14 (a). As can be seen, it allows a good detection of the considered inclusion. The

42

reconstructions of the dielectric properties yielded by applying the hybrid method (with $p = 1.3$), are provided by Figure 3.14 (b)-(c). The corresponding results obtained with applying only the quantitative method are reported in Figure 3.14 (d)-(e). In this case, too, the use of hybrid method allows again a better reconstruction of dielectric properties and a quite good detection of the inclusion if compared with the results provided by the quantitative approach. In the latter reconstructions, however, significant artefacts are presented, in particular concerning the distribution of the electric conductivity.

(a)

(b)   (c)

(d)   (e)

Figure 3.14: "Phantom 1" with glass inclusion with $d_{g2} = 24$ mm. (a) Qualitative image provided by the DAS method. Reconstructions obtained (800 MHz and $p = 1.3$) by using the hybrid method, (b) relative dielectric permittivity and (c) electric conductivity. Reconstructions obtained by using the quantitative method alone, (d) relative dielectric permittivity and (e) electric conductivity [106].

43
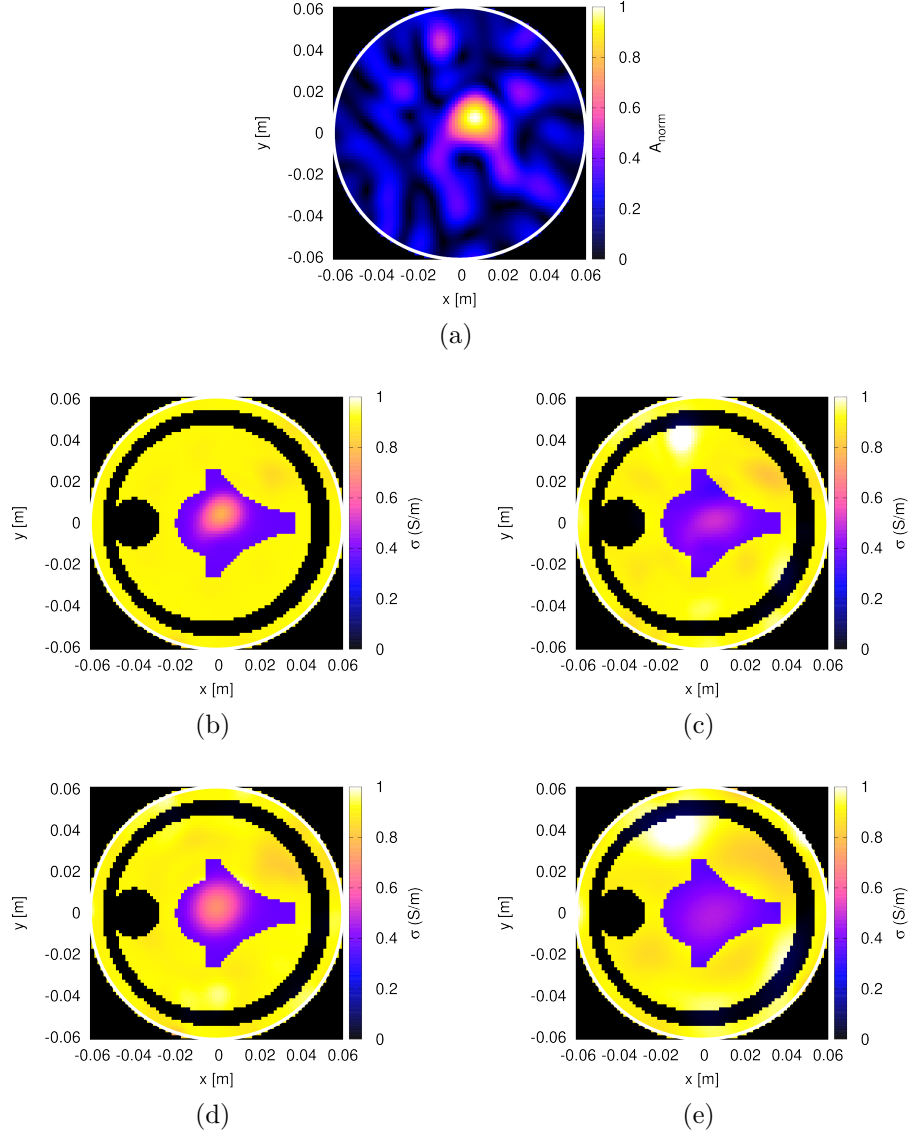
Figure 3.15: "Phantom 2" with an inclusion with $d_{v1} = 18$ mm. (a) Qualitative image provided by the DAS method. Reconstructions of electric conductivity with hybrid method (b) with $p = 1.3$ and (c) with $p = 2.0$. Reconstructions with quantitative method alone (d) with $p = 1.3$ and (f) with $p = 2.0$ [106].

Finally, "Phantom 2" is considered, for which the inclusion has a diameter $d_{v1} = 18$ mm. The obtained DAS image is reported in Figure 3.15 (a). It exhibits more artefacts than in the previous cases, although the inclusion region can be correctly localized. For this case, a comparison between the results obtained with the hybrid method ($p = 1.3$ and $p = 2.0$), and with the quantitative method applied in a straightforward way, are given. In particular, Figure 3.15 (b)-(e) report the reconstructed images of the electric conductivity obtained with the hybrid method, with $p = 1.3$ (Figure 3.15(b)) and with $p = 2.0$ (Figure 3.15 (c)), and the results obtained by the quantitative method, with $p = 1.3$ (Figure 3.15 (d)) and with $p = 2.0$ (Figure

3.15 (e)). The best detection of the inclusion is obtained with the hybrid method with $p = 1.3$. Both with the hybrid method and the quantitative one, the retrieved distributions include some artefacts and the electric conductivity of the inclusion is rather underestimated.

In conclusion, the presented results demonstrate the capabilities of the proposed hybrid method in improving the reconstruction of the distribution of the dielectric parameters. In general, for the considered cases, the best results are obtained with a norm parameter equal to 1.3.

Chapter 4

Inversion Methods with Machine Learning Approach

In this Chapter, another new, fast and reliable imaging method based on a machine learning approach is investigated. Artificial neural networks (ANNs) represent recent and useful tools for quantitative microwave imaging. In particular, fully-connected neural networks have been found to be very effective in this framework [107]. In this Chapter, the network architecture is presented, followed by the description of the dataset constructed on the basis of numerical neck phantoms. As it is well known, in machine learning approaches a massive quantity of data for the training phase is required. To this end, a set of neck phantoms is used in this phase. The aim of the proposed approach is to retrieve the geometric and dielectric properties of the cross section of the human neck under investigation, starting by the measured values of the scattered electric field, which represent the input of the fully-connected network.

4.1   Network Architecture

A feed-forward fully-connected network allows implementing a direct inversion of the values of the scattered electric field in order to retrieve the dielectric properties of the neck profiles. In particular, the adopted network is shown in Figure 4.1. As can be seen, it includes L hidden layers and D neurons for each layer. All the hidden layers have the same number of units, except the last layer, which is denoted as the $L+1$ layer. With reference to the general tomographic imaging configuration reported in Figure 2.5 (section 2.5.3), the network input is the array of values of the scattered electric fields, which is defined as following

$$\mathbf{P} = [Re\{E_s^{1,1,1}\}, \dots, Re\{E_s^{S,F,M}\}, Im\{E_s^{1,1,1}\}, \dots, Im\{E_s^{S,F,M}\}]^T \qquad (4.1)$$
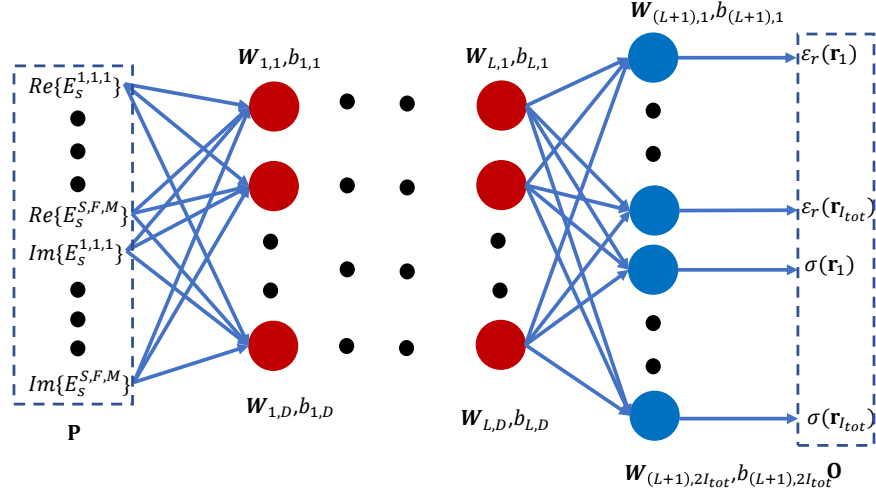
Figure 4.1: Sketch of the fully-connected artificial neural network architecture adopted in the present Thesis [108].

The array contains the values of the real and the imaginary part of the scattered field collected for each view s, $s = 1, \ldots, S$ (S number of views), frequency f, $f = 1, \ldots, F$ (F number of frequencies), and measurement point m, $m = 1, \ldots, M$ (M number of measurement points). Moreover, the output of the network is an array containing the values of the dielectric properties in each cell R_i of the investigation domain $\mathbf{O} = [\epsilon_r(\mathbf{r}_1)], \ldots, \epsilon_r(\mathbf{r}_{I_{tot}}), \ldots, \sigma(\mathbf{r}_1), \ldots, \sigma(\mathbf{r}_{I_{tot}})]^T$.

For the dth unit of the lth layer of the network, a numerical array of weights of its input connections $\mathbf{W}_{l,d} \in \mathbb{R}^D$, and a scalar bias value, $b_{l,d}$, are defined, with $l = 1, \ldots, L$ and $d = 1, \ldots, D$. The $L + 1$ layer has a number of neurons equal to $2I_{tot}$, where I_{tot} is the number of square cells in which the investigation domain Ω_t is partioned (see Section 2.5.3). Accordingly, the output array $\mathbf{O}$ is obtained as

$$\mathbf{O} = \mathbf{R}[\mathbf{W}_{L+1,1}^T\mathbf{O}_L + b_{L+1,1}, \ldots, \mathbf{W}_{L+1,2I_{tot}}^T\mathbf{O}_L + b_{L+1,2I_{tot}}]^T \tag{4.2}$$

where $\mathbf{W}_{L+1,1}^T \in \mathbb{R}^{2I_{tot}}$ and $b_{L+1,d} \in \mathbb{R}^D$ are the numerical array of weights and a scalar bias value of the last layer, respectively. The output of a generic layer $l = 2, \ldots, L$ can be written as

$$\mathbf{O}_l = \mathbf{R}[\mathbf{W}_{l,1}^T\mathbf{O}_{l-1} + b_{l,1}, \ldots, \mathbf{W}_{l,D}^T\mathbf{O}_{l-1} + b_{l,D}]^T \tag{4.3}$$

For the first hidden layer, $l = 1$, the output is

$$\mathbf{O}_1 = \mathbf{R}[\mathbf{W}_{1,1}^T\mathbf{P} + b_{1,1}, \ldots, \mathbf{W}_{1,D}^T\mathbf{P} + b_{1,D}]^T \tag{4.4}$$

with $\mathbf{W}_{1,d} \in \mathbb{R}^{S \times F \times M}$ and $b_{l,d} \in \mathbb{R}^D$ are the numerical array and the scalar bias value of the first layer, respectively. In the equations (4.2) - (4.4), $\mathbf{R}$ indicates the so-called Rectified Linear Unit (ReLu) activation function [109], i.e.,

$$\mathbf{R}(\mathbf{x}) = [\mathsf{relu}(x_1), \mathsf{relu}(x_2), \dots, \mathsf{relu}(x_D)]^T \tag{4.5}$$

where $\mathbf{x} = [x_1, x_2, \dots, x_D]^T$ and

$$\mathsf{relu}(x) = \begin{cases} x, & if \ x \leq 0 \\ 0, & otherwise \end{cases} \tag{4.6}$$

Finally, to train the fully-connected neural network, a large dataset of neck phantoms is necessary. In particular, the dataset will be split in two different groups, the training and the validation set. The first set is used to "training" the developed network with selected parameters, such as the number of hidden layers, neurons for each layer, etc.. The training phase is used to obtain the best weights vectors that minimize the prediction error. Usually, the weights are randomly initialized with a normal distribution with zero mean and a standard deviation equal to 0.01. For each training epoch, i.e. the number of times in which the neural network is trained with all the training data, the difference between the actual output and predicted one is calculated. The loss function is used to calculate the reconstruction error in the training set for each epoch. Then, backpropagation is used to update the weights in an attempt to correctly map arbitrary inputs to outputs. In the backpropagation, an iterative optimization algorithm is used for finding the minimum of the error function. The aim is to reduce the difference between prediction and actual output. The second set is used to "validate" the network, such as the set is used to evaluate the performance of the network. In particular, during the training phase, the error prediction of the validation set is evaluated. When the error on the validation set increases whereas the error on the training set is stable, this is sign of over-fitting to the training set. The network learns too much from the training data, such as the weights in the network allow a good prediction for the training data but not for a new input data not used in the training phase.

Finally, the obtained weights of the trained network are used to predict the reconstructions for the test set. The data in the test set are different from the training and validation set and are used to evaluate the performance of the developed network.
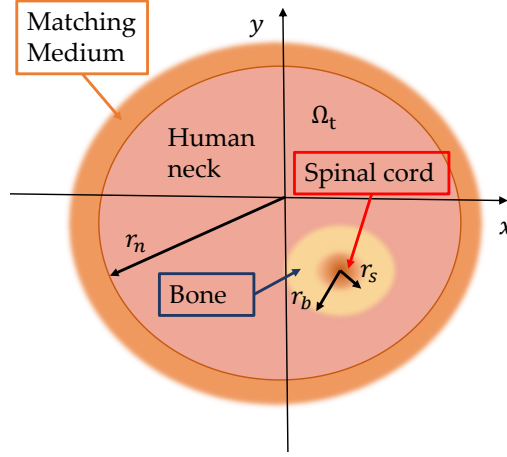
Figure 4.2: Sketch of the simplified neck phantom [110]

4.2 Numerical Neck Phantom

In order to perform a quantitative inversion by means of the proposed neural network, a database of simplified neck phantoms, with different geometric and dielectric properties, has been developed.

4.2.1 Circular Cross Section Cylinders

Firstly, a circular cylinder filled with dielectric properties of the average of the internal neck tissues, which are approximated by a medium with dielectric properties calculated with a concentration of 80% muscle and 20% fat, following the suggestions reported in [99], [100], is created. Accordingly, the relative dielectric permittivity and electric conductivity has been chosen to change in the range $[40, 50]$ and $[0.5, 0.8]$
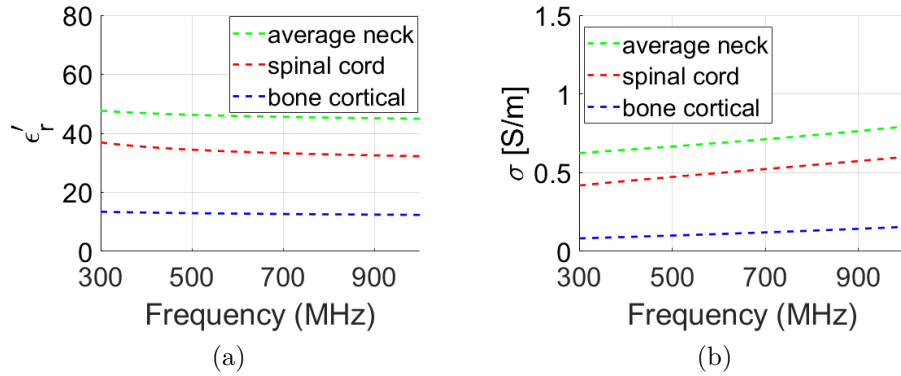
Figure 4.3: (a) Relative dielectric permittivity and (b) electric conductivity of the considered neck tissues [110].

Tissue	Radius Range [cm]	ϵ_r	$\sigma[S/m]$
Average Neck	[5,7]	[40,50]	[0.5,0.8]
Bone	[2,2.5]	[10,20]	[0.06,0.2]
Spinal Cord	[0.5,0.9]	[30,40]	[0.4,0.7]

Table 4.1: Summary of tissues parameters variations adopted in simplified neck phantoms [110].

S/m, respectively. The dimension of the radius of the neck, r_n, varies uniformly in the range $[5,7]$ cm and its center changes randomly no more than of 1 cm with respect to the center of the coordinate system. On the outside of the main structure of the neck, a circular shell representing the coupling medium between the antennas and the neck is added, as shown in Figure 4.2. This layer has an external radius $r = 8$ cm and fixed dielectric properties, i.e., $\epsilon_r = 43$ and $\sigma = 0.8$ [S/m], which approximately correspond to those of a 70% glycerin/water mixture at 750 MHz [111]. Others circular cylinders are used to mimic the main internal neck structures, i.e., the bone and the spinal cord. The bone radius varies uniformly in the range $r_b \in [2, 2.5]$ cm. Its center varies maximum of 1 cm with respect to the center of the neck. The relative dielectric permittivity of this layer, in the training set, ranges from 10 to 20 and the electric conductivity lies in the range $[0.06, 0.2]$ S/m. The last considered tissue is the spinal cord whose properties range from 30 to 40 and from 0.4 to 0.7 S/m for the relative dielectric permittivity and the electric conductivity, respectively. The radius r_s can change from 5 mm up to 9 mm, to represent physiological and pathological conditions. The range of values used to generate the dataset are summarized in Table 4.1. The different ranges in which the dielectric properties vary are shown in Figure 4.3.

4.2.2 Models from Virtual Family

To improve the complexity of the neck phantom, two strategies to define the training set based on a realistic neck slice extracted from the man phantom of $Virtual Family$ [112] are developed.

Five-Tissues Model

In the first simplified case, the spline function [113] is used to randomly generate the boundary of five considered biological tissues of the neck, i.e., bone, muscle, skin, spinal cord and trachea. The spline function create smooth curves out of irregular data points, called control points. When the coordinate of the control points change,
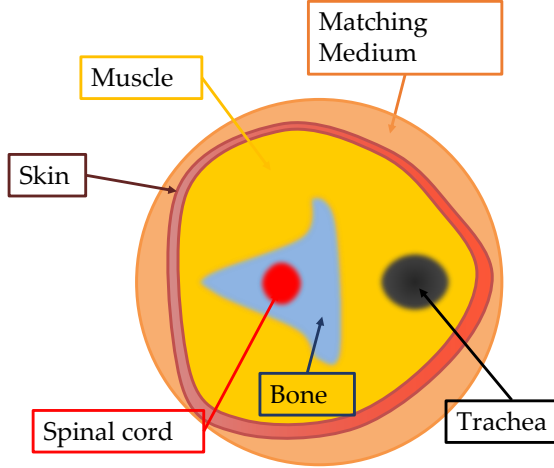
Figure 4.4: Sketch of five-tissues neck phantom that includes: bone, muscle, skin, spinal cord and trachea [110].

the obtained shape is different from the previous one. Figure 4.4 provides a sketch of the developed phantom. The control points of the spline function and the dielectric properties of each tissue are randomly varied in a given range, to obtain realistic phantom.

Nine-Tissues Model

The second case is more accurate than the previous one. The slice from the Duke phantom is extracted at 1.60 m of height and includes the third cervical vertebra, as shown in Figure 4.5 (a). The discretization of the considered slice is equal to 2 mm and 9 biological tissues are present, i.e., skin, fat, muscle, vertebral bone, spinal cord, trachea, cartilage, cerebrospinal fluid (CSF) and blood vessels. To obtain a suitable phantom that can mimic the real neck, all tissues are considered, except CSF, which is only present in a few pixels of the slice and its presence is not relevant for our study, as can be seen in Figure 4.5 (b). The remaining tissues are modeled in a simple way to allow a reproducible and randomized generation of phantoms. In this case, the boundaries of tissues are modeled by means of two different approaches: Ellipses and splines. As shown in Figure 4.5 (b), the tissues boundaries modeled with ellipses are:

- Vertebral Bone

- Infiltrated Fat

- Cartilage.

Spline functions are used to model the remaining biological tissues boundaries, i.e.:

- Skin

- Subcutaneous Fat

- Muscle

- Spinal Cord

- Blood Vessels

- Trachea

Specifically, in order to define a curve that models the particular shape of some tissue boundaries, the natural cubic spline functions are considered. This kind of functions takes the coordinates of some chosen points, called control points, and defines a curve that passes through them. In this way, a specific shape is obtained. With this approach, the first modeled tissue boundary is the skin, which also defines the external shape of the neck. To develop the skin structure, 14 control points have been considered adequate to mimic the external shape of the phantom. The control points allow generating different configurations and sizes of the neck. The thickness of the skin vary in the range $[2, 4]$ mm. After that, the subcutaneous fat tissue is also modeled with spline functions. This tissue is located internally, adjacent to the skin and its thickness df varies between $[2, 8]$ mm. The subcutaneous fat is located along the skin, both in the anterior and posterior part of the neck. Defined these two tissues (skin and subcutaneous fat) the structure is internally filled with the dielectric properties of muscle. In this way, the shape of muscle depends only on the thickness of skin and subcutaneous fat. Then, the remaining anatomical structures are located inside the neck, overlapping with the previous ones already created.
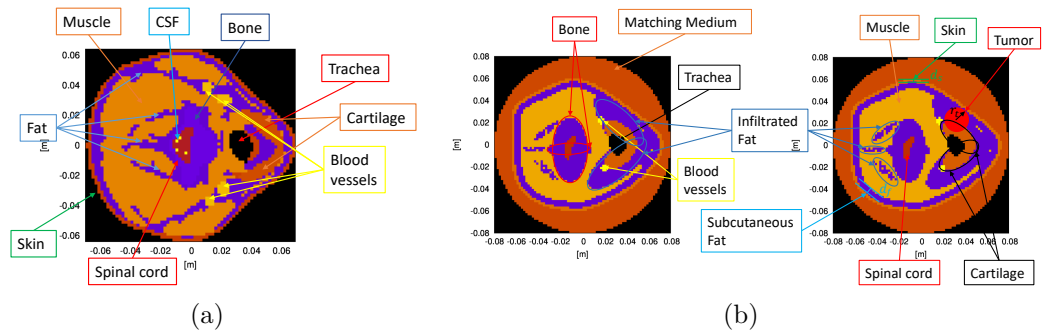
Figure 4.5: Realistic cross section of the neck: (a) Slice extracted from the *Duke* man phantom of the *VirtualFamily*. (b) Example of a nine-tissues neck phantom with different structures: bone, blood vessels, cartilage, infiltrated fat, subcutaneous fat, muscle, skin, spinal cord, trachea and tumor [108].

52

Internally to the vertebral bone, the spinal cord is inserted. In this case, 5 control points are used to define the tissue and are chosen to obtain a shape that can mimic the stretched configuration of the spinal cord. Other considered structures are the blood vessels. In the Virtual Family phantom [Fig. 4.5 (a)], there are two arteries and two veins, one for each side of the neck. In the developed phantom, only one vessel for each side is considered for simplicity and because their presence is not so relevant for this study. In this case, 4 control points are used to define the shape of the vessel, and then such a shape is duplicated to obtain the second vessel. Finally, the trachea structure is created. Here, 5 control points are used to obtain the structure. As shown in Figure 4.5 (b), the trachea is embedded inside the cartilage tissue.

To reproduce other tissue structures, one or more ellipses are used. First, the vertebral bone is created using two ellipses, one placed vertically and the other horizontally. Another tissue modeled with elliptic shape is the infiltrated fat. For this tissue, three ellipses are placed near the bone, in the posterior region of the neck. Within such ellipses, a binary random variable with uniform distribution defines whether pixels are occupied by fat or not. To complete the presence of fat in the phantom, other two ellipses are defined, which are placed in the anterior part of the neck. The last biological tissue modeled with elliptic structures is cartilage: two ellipses are located in the anterior part of the neck, overlapped to the fat structure.

Considering all tissues, those created with ellipses and those with the spline functions, the obtained phantom - although unavoidably simplified - reproduces in a suitable way the cross section of the neck. To create the training set, a huge number (hundreds) of neck phantoms are required. For this reason, each geometrical parameter, i.e., center and semi-axes of ellipses, coordinates of the spline control points and dielectric properties, randomly varies in a certain range to obtain different phantoms preserving the simplicity and the realism of the neck. The ranges in which the dielectric properties vary are selected following their dielectric behavior in the considered frequency band [72]. The coordinates of the control points vary along the $x-y$ axis, both in the negative and positive directions respect of a cartesian coordinates system, in which the center is in (0,0) mm. Moreover, each neck structure is rotated by applying a rotation matrix with random angle $\phi \in [-45°, 45°]$, to increase the variability of the training set. In Table 4.2, the properties of the tissues considered for the developed phantoms are given. The value of each parameter is randomly defined (with uniform distribution in the reported intervals) and independent from each other. The approach used to generate each tissue region, the position of the center and the size of the semi-axes for ellipses, the number of control points for the spline functions, as well as the dielectric properties are also provided.

Finally, to obtain the neck cross section with a tumor (i.e., to reproduce a pathological situation) a circle with radius r_t is inserted in the anterior part of the neck, near the trachea. For tumors such as supraglottic laryngeal carcinoma [59] and thyroid cancer [60], the cross section can be approximated as a circular inclusion [114]. Also in previous works [115], [116], [117], the tumor cross sections have been simulated like circles. Tumors such as thyroid cancers [59], [114], neck sarcomas or cervical lymph node metastases [61] are nodular, being approximately spherical, with a radius in the range 3-5 mm, located up to 3 cm below the skin surface [118], [119], [120]. To reproduce in an accurate way the dielectric properties of the tumor, the results reported in [116] are used. For most neck tumors, the relative dielectric properties are relatively high, and in the considered frequency band are on average around $\epsilon_r \approx 59$ and $\sigma \approx 0.9$ [S/m], as can be derived by MRI and as usually modeled in numerical studies in the field of microwave hyperthermia [72], [117], [121], [122]. For this reason, by also taking into account possible changes of such parameters, the dielectric properties of the simulated tumor model were chosen in the range between 55 and 65 for the relative dielectric permittivity, whilst the electrical conductivity lies within $[0.5, 1]$ S/m. Also in this case, the generated neck phantom is set inside a circular shape with radius $r = 8$ cm and $\epsilon_r = 43$ and $\sigma = 0.8$ S/m, representing the matching medium, between the antenna and the neck. The dielectric properties of the matching medium have been selected in order to increase the field penetration and to reduce the reflection due to the skin. In particular, as shown in [101], a 70% glycerin/water mixture allows obtaining a good tradeoff between these two requirements.

4.3 Numerical Results

In this Section, preliminary numerical results are reported. As first dataset, the simplified circular phantoms, described above, are considered for the training procedure. The investigation domain Ω_t is discretized into $I_{tot} = 5024$ square cells of side 2 mm and $N_a = 10$ antennas are simulated to sequentially illuminate via TM fields the neck. The system acquired measurements at $F = 7$ different frequencies in the range $[600, 900]$ MHZ. We assume a fully-connected network with $L = 4$ hidden layers and $D = 64$ neurons in each layer. The weights vectors illustrated above, are initialized by a Gaussian distribution with zero-mean and standard deviation equal to 0.01 and the initial bias is set to zero. The updating rule for the training procedure is based on the adaptive moment estimation method (ADAM) [123], with a learning rate equal to 0.01, to minimizes the loss function, which is in this case the

Neck tissue	Developed phantom		No. of control points	Variability of semi-axis a, b [mm]	Variability of ellipses center (x_0, y_0) [mm]	Rotation angle ϕ [deg]	Variability of control points [mm]	ϵ_r	σ [S/m]
Skin	Spline		14	-	-	-	[-6,6]	[40,50]	[0.6,1]
Sub-cutaneous	Spline		14	-	-	-	[-6,6]	-	-
Fat	Filled Ellipses	Fat 1	-	$a \in [10,16]$ $b \in [26,40]$	$x_0 \in [20,34]$ $y_0 \in [4,14]$	[215,235]	-	[8,15]	[0.006,0.13]
		Fat 2		$a \in [10,16]$ $b \in [26,40]$	$x_0 \in [20,34]$ $y_0 \in [-14,-4]$	[125,145]			
Infiltrated	Partially Filled Ellipses	Fat 3	-	$a \in [2,6]$ $b \in [8,16]$	$x_0 \in [-14,6]$ $y_0 \in [-6,6]$	[215,235]	-		
		Fat 4		$a \in [2,6]$ $b \in [8,16]$	$x_0 \in [-14,6]$ $y_0 \in [-6,6]$	[125,145]			
		Fat 5		$a \in [2,6]$ $b \in [6,14]$	$x_0 \in [-14,6]$ $y_0 \in [-6,6]$	0			
Muscle	Spline		14	-	-	-	[-6,6]	[50,60]	[0.7,1]
Bone	Ellipses	Bone 1	-	$a \in [20,32]$ $b \in [6,20]$	$x_0 \in [-14,6]$ $y_0 \in [-6,6]$	0	-	[10,20]	[0.006,0.2]
		Bone 2		$a \in [6,20]$ $b \in [20,32]$	$x_0 \in [-14,6]$ $y_0 \in [-6,6]$	0			
Cartilage	Ellipses	Cartilage 1	-	$a \in [6,10]$ $b \in [20,30]$	$x_0 \in [20,34]$ $y_0 \in [4,10]$	[215,235]	-	[44,49]	[0.5,0.8]
		Cartilage 2		$a \in [6,0]$ $b \in [20,30]$	$x_0 \in [-34,-20]$ $y_0 \in [4,10]$	[125,145]			
Spinal cord	Spline		5	-	-	-	[-2,4]	[30,40]	[0.4,0.7]
Blood Vessels	Spline		4	-	-	-	[-2,2]	[58,68]	[1.3,1.6]
Trachea	Spline		5	-	-	-	[-2,2]	1	0
CSF	-		-	-	-	-	-	-	-
Tumor	Ellipse		-	$a = b \in [5,15]$	$x_0 \in [x_0^{trachea} +10, x_0^{trachea} +20]$ $y_0 \in [y_0^{trachea} -10, y_0^{trachea} +10]$	0	-	[55,66]	[0.5,1]

Table 4.2: Parameters of the tissues inside the neck phantom [108].

mean square error (MSE). The choice of learning rate value is a trade-off between a too large value, that can cause the model to converge too quickly to a suboptimal solution, and a too small value that can requires more training epochs and can cause the process to get stuck.The training procedure is performed with a maximum of 100 epochs.

To test the performance of the developed network, a dataset of $K = 7000$ simplified neck phantoms is built. 90% of the data are used in the training procedure, the remaining 10% as validation set. A test case is created according to the procedure explained in Section 4.2, with the dielectric properties of tissues related to a random frequency in the considered range. The neck under test is created following the procedure described above, specifically presents a circular cross section of radius equal to $r_n = 6$ cm, wich represent the external shape of the neck, with the relative dielectric permittivity equal to 45.87 and the electric conductivity equal to 0.688 S/m. Its center is in $(0, -0.005)$ m. The bone is a circular cylinder with radius equal to $r_b = 2.3$ cm centred in $(0.011, 0.001)$ m, with $\epsilon_{r,bone} = 12.79$ and $\sigma_{bone} = 0.11$ S/m. At the end, the spinal cord circle is set in $(0.009, 0.001)$ m with radius equal to $r_s = 9$ mm. The dielectric properties are $\epsilon_{r,spinal} = 37.77$ and $\sigma_{spinal} = 0.497$ S/m. A custom direct solver based on method of moments (MoM) is applied on the created neck profiles to calculate the corresponding scattered electric fields. Moreover, to test the network response with more realistic data, the total electric fields of validation set and the test case were corrupted with a white Gaussian noise with a variance corresponding to a SNR equal to 35 dB and zero mean value. The results obtained for the test case are reported in Figure 4.6 and confirm a quite accurate reconstruction. To evaluate the accuracy of the reconstruction, normalized mean square errors are calculated as

$$err_{\epsilon_r,\sigma} = \frac{||rec_{\epsilon_r,\sigma} - obj_{\epsilon_r,\sigma}||^2}{||obj_{\epsilon_r,\sigma}||^2} \tag{4.7}$$

in which $rec_{\epsilon_r,\sigma}$ and $obj_{\epsilon_r,\sigma}$ represent the reconstructed and the actual values of relative dielectric permittivity and electric conductivity, respectively. The mean square errors of the reconstructed distributions of ϵ_r and σ are $err_{\epsilon_r} = 0.070$ and $err_\sigma = 0.11$. These results show that the reconstruction of the relative dielectric permittivity is slightly better than the one of the electric conductivity, as can be seen in Figures 4.6 (b)-(d). In particular, in the ϵ_r reconstruction image there are few artefatcts. Moreover, reconstructed radius of the spinal cord is equal to 17.8 mm, which is very close to the original value.
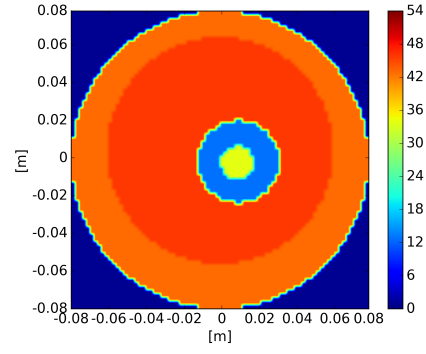
(a)
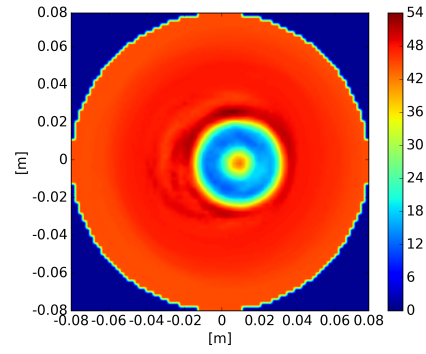
(b)
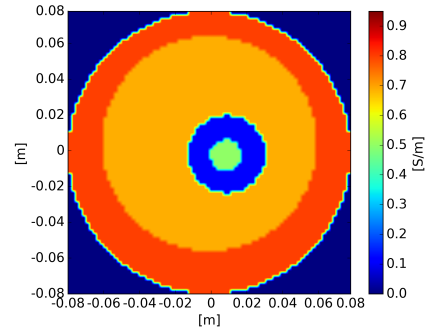
(c)
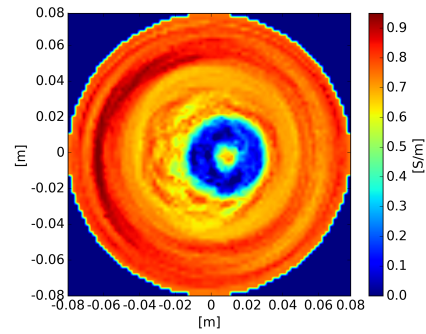
(d)

Figure 4.6: Reconstruction of simplified neck test configuration: (a) Relative dielectric permittivity of the reference configuration. (b) Distribution map of relative dielectric permittivity obtained via ANN. (c) Electric conductivity of the reference configuration. (d) Distribution map of electric conductivity obtained via ANN [110].
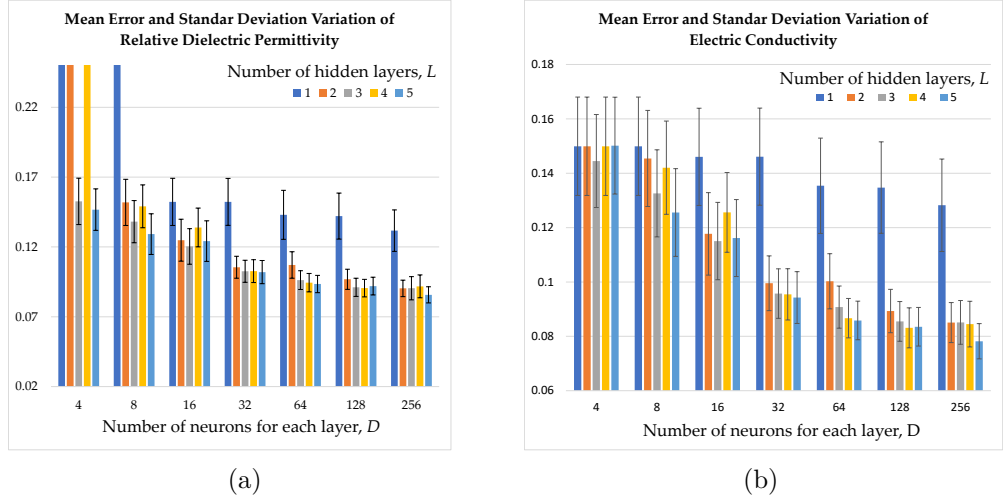
Figure 4.7: Mean error and standard deviation of (a) ϵ_r and (b) σ versus the number of L hidden layers and D neurons [110].

In another set of simulations, the five-tissues model described above, is used to train and test the network. In this case, too, $K = 7000$ are numerically constructed and the same number of training and validation sets are considered. All the network parameters are the same as in the previous case, except for the loss function that in this case is expressed as

$$\mathcal{L} = \frac{1}{D_{tr}} \left[\sum_i \frac{||rec_{\epsilon_r}^i - obj_{\epsilon_r}^i||}{||obj_{\epsilon_r}^i||} + \sum_i \frac{||rec_\sigma^i - obj_\sigma^i||}{||obj_\sigma^i||} \right] \tag{4.8}$$

The choice to normalize the ϵ_r and σ values allows to obtain two quantities comparable between them and a better reconstruction of both of ϵ_r and σ (previously the reconstruction of σ was worse). D_{tr} is the number of samples considered in the training procedure and i represents the ith considered samples.

A preliminary analysis concerning different numbers of hidden layers, neurons and values of SNR on field of the test set is performed. Figure 4.7 shows the mean error (equation (4.7)) and the standard deviation, both for ϵ_r and σ, versus L and D in the test set. The number of hidden layers is set to $L = \{1, 2, \ldots, 5\}$, whereas the number of neurons for each layer is $D = \{4, 8, 16, \ldots, 256\}$. The graphs show that for one hidden layer and a low number of neurons the errors are always very high, and they decrease as the number of neurons and layers increase. In particular, the best results are obtained with the highest number of layers and neurons, $L = 5$ and $D = 256$. Moreover, the distribution maps of reconstructed dielectric properties of a test case are evaluated with different network architecture, in particular with: $L = 1$ and $D = 4$; $L = 4$ and $D = 128$; $L = 5$ and $D = 256$. The obtained maps for all
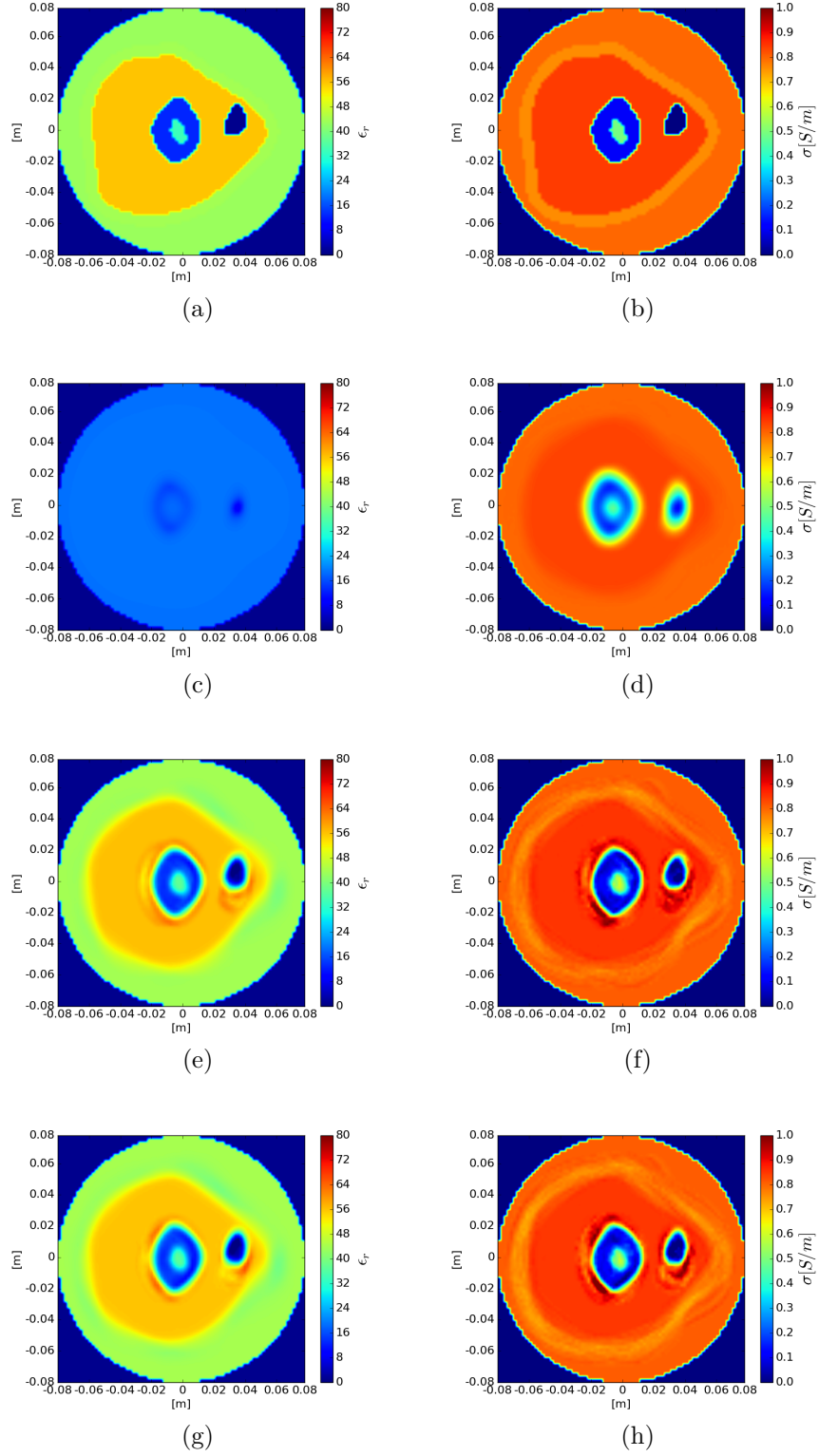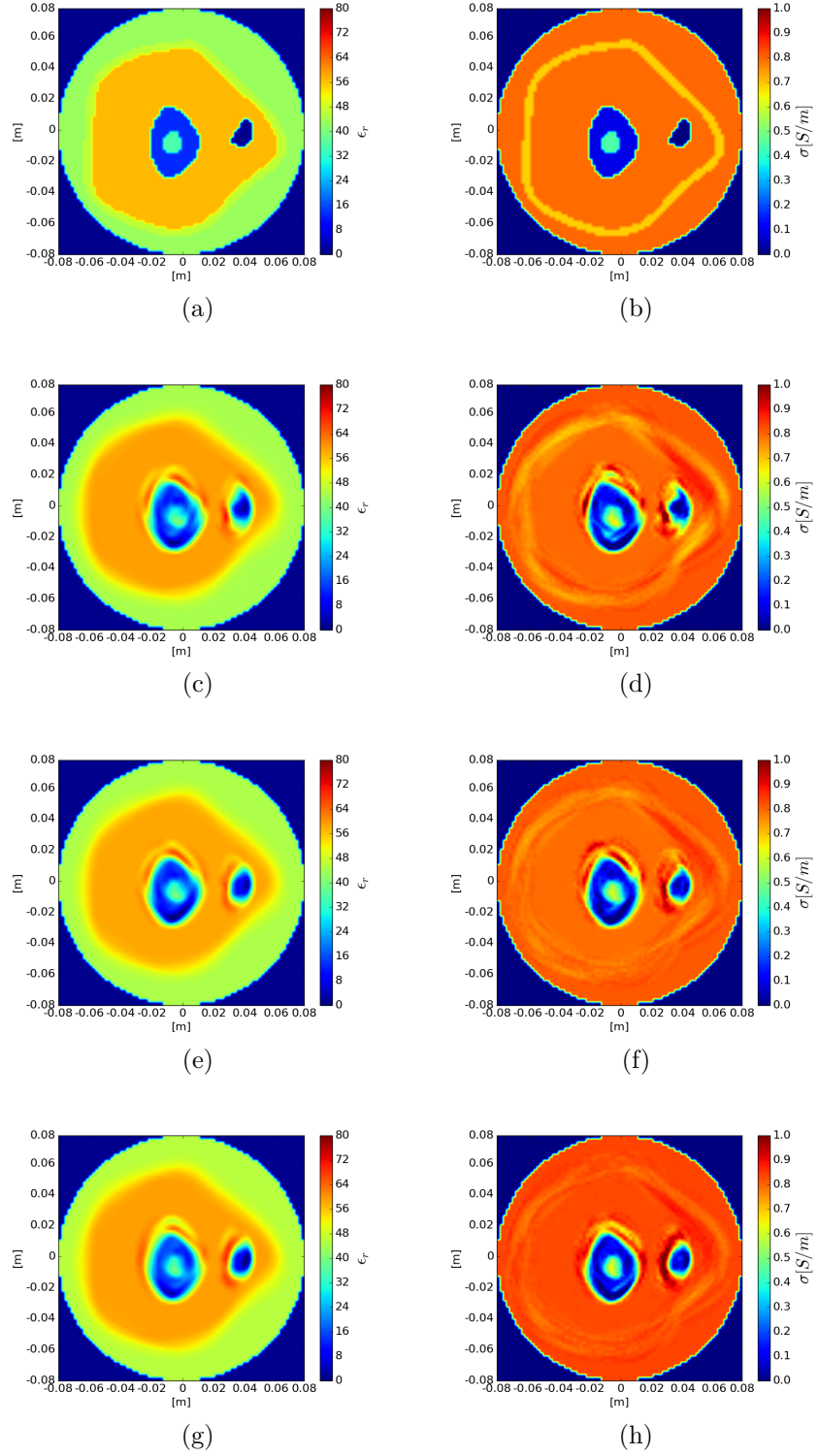
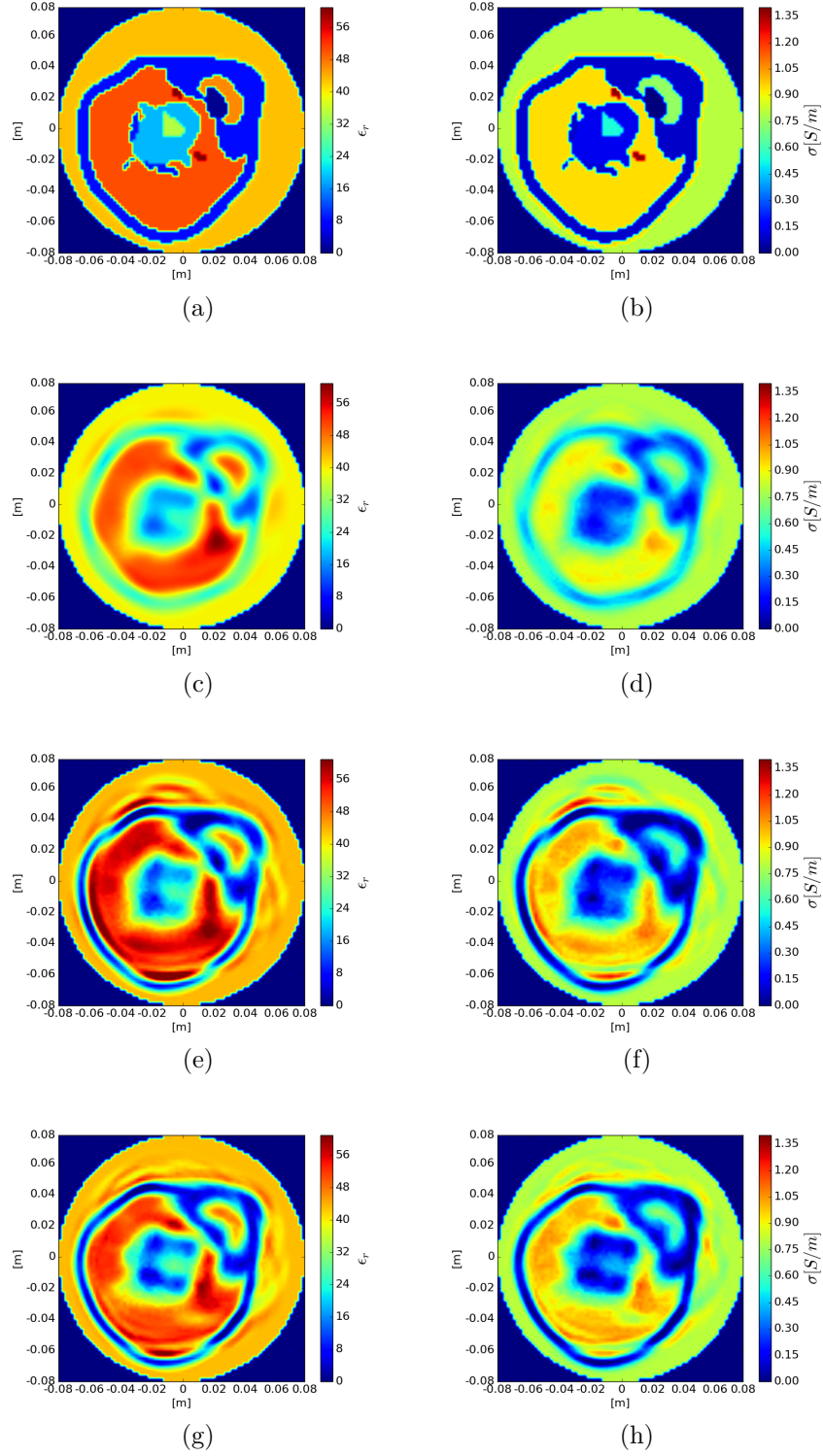Figure 4.8: Five-tissues neck configuration. (a) Actual relative dielectric permittivity and (b) electric conductivity. Reconstruction with $L = 1$ and $D = 4$ of (c) ϵ_r and (d) σ. Reconstruction with $L = 4$ and $D = 128$ of (e) ϵ_r and (f) σ. Reconstruction with $L = 5$ and $D = 256$ of (g) ϵ_r and (h) σ

.

cases are shown in Figure 4.8, in which Figure 4.8 (a)-(b) represent the actual distributions maps of dielectric properties, ϵ_r and σ, respectively.

As can be seen, the reconstructions of dielectric properties with the lowest number of layers and neurons don't allow to correctly detect the inner biological structure. In particular, ϵ_r and σ are highly underestimated, and the skin is not detected. On the contrary, with higher numbers of L and D, the reconstructed structures are more accurate, and it is possible to individuate all tissues. The best reconstructions are shown in Figure 4.8 (g)-(h), with $L = 5$ and $D = 256$, confirming the previous results shown in the graphs of Figure 4.7.

Moreover, the mean error and the standard deviation are evaluated changing the SNR value, considering a neural architecture with $L = 4$ and $D = 128$. The total electric field of test set is corrupted with a Gaussian noise with zero mean and variance corresponding to a given SNR. The graph in Figure 4.9 shows how the mean error and standard deviation decrease when the SNR value increase, and this behavior is in line with what is expected.

For completeness, the maps of reconstructed dielectric properties of some test cases with different value of SNR are shown in Figure 4.10, in which Figure 4.10 (a)-(b) represent the actual distribution of dielectric properties, ϵ_r and σ, respectively. In Figure 4.10 (c)-(d) the reconstructions obtained with $SNR = 5$ dB are presented. As can be seen, the reconstructions show significant artifacts, near the trachea and the bone, both in the ϵ_r and σ. With $SNR = 15$ dB (Figure 4.10 (e)-(f)), the reconstructions improve and the best of all configurations, in particular in the internal structures, are obtained with $SNR = 25$ dB, shown in Figure 4.10 (g)-(h).

Finally, the most complex dataset described in the previous Section, the nine-
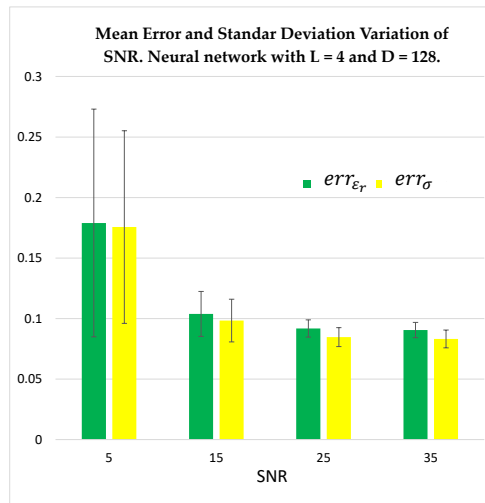
Figure 4.9: Mean error and standard deviation of ϵ_r and σ versus the SNR value [110]

tissues model, is used in the training phase. A preliminary analysis is performed in order to choose the best parameters for the neural network architecture. Then, the selected architecture is tested with different cases. To train the developed neural network, a data set of $K = 30000$ simplified neck phantoms is built. Each neck phantom is generated by the random variations of the dielectric and geometrical properties described in Section 4.2. The dataset does not contain any duplicate. The investigation domain is discretized with $I_{tot} = 5024$ square cells of side 2 mm. Half of the dataset represents the neck profile with the presence of variable tumors in the anterior neck area, whereas the other half is without tumor. This dataset is subdivided into two subsets: 95% of the samples for the training procedure and the remaining 5% for the validation phase. A custom direct solver based on MoM is applied on the created neck profiles to calculate the corresponding scattered electric fields, with $F = 7$ frequencies in the range $[600, 900]$ MHz, $N_a = 10$ antennas, and $M = 9$ measurement points. Moreover, a Gaussian noise with zero mean value and $SNR = 35$ dB is added to the total electric fields of validation cases to obtain more realistic data.

The neural network parameters are the same as the previous cases, and 500 epochs for each training phase are considered, with mini-batch size of 256. The considered loss function is expressed in equation (4.8). The input layer size is defined as $F \times S \times M \times 2 = 1260$, whereas the output layer consists of $2I_{tot} = 10048$ neurons.

In order to find a trade-off between the accuracy in the reconstruction and computational complexity, different network architectures are tested. To perform a quantitative assessment for evaluating the best architecture, for each proposed network structure, the average error parameters err_{ϵ_r} and err_{σ} described in equation (4.7) are calculated for the reconstructions of the data in the validation set.

Also in this analysis, the impact of the number of L and D are evaluated. To this end, the number of hidden layers is set to $L = \{1, 2, \ldots, 5\}$, whereas the number of neurons for each layer is $D = \{32, 64, 96, \ldots, 512\}$. Figure 4.11, which reports the behaviors of err_{ϵ_r} and err_{σ} versus L and D, shows that for $L = 5$ hidden layers and $D = 448$ neurons the smallest reconstruction errors are obtained, both for relative dielectric permittivity err_{ϵ_r} [Figure 4.11 (a)] and for electric conductivity err_{σ} [Figure 4.11 (b)]. The findings show that err_{ϵ_r} and err_{σ} assume the highest values for $L = 1$, regardless of the value of D. Moreover, the reconstruction errors remain high for $L = 32$ and any value of D. This analysis highlights that for $L = 1$ and a low number of neurons the reconstruction is not accurate. Indeed, as shown in other works [107], a too small number of hidden layers and neurons does not allow a good quality of the reconstruction.
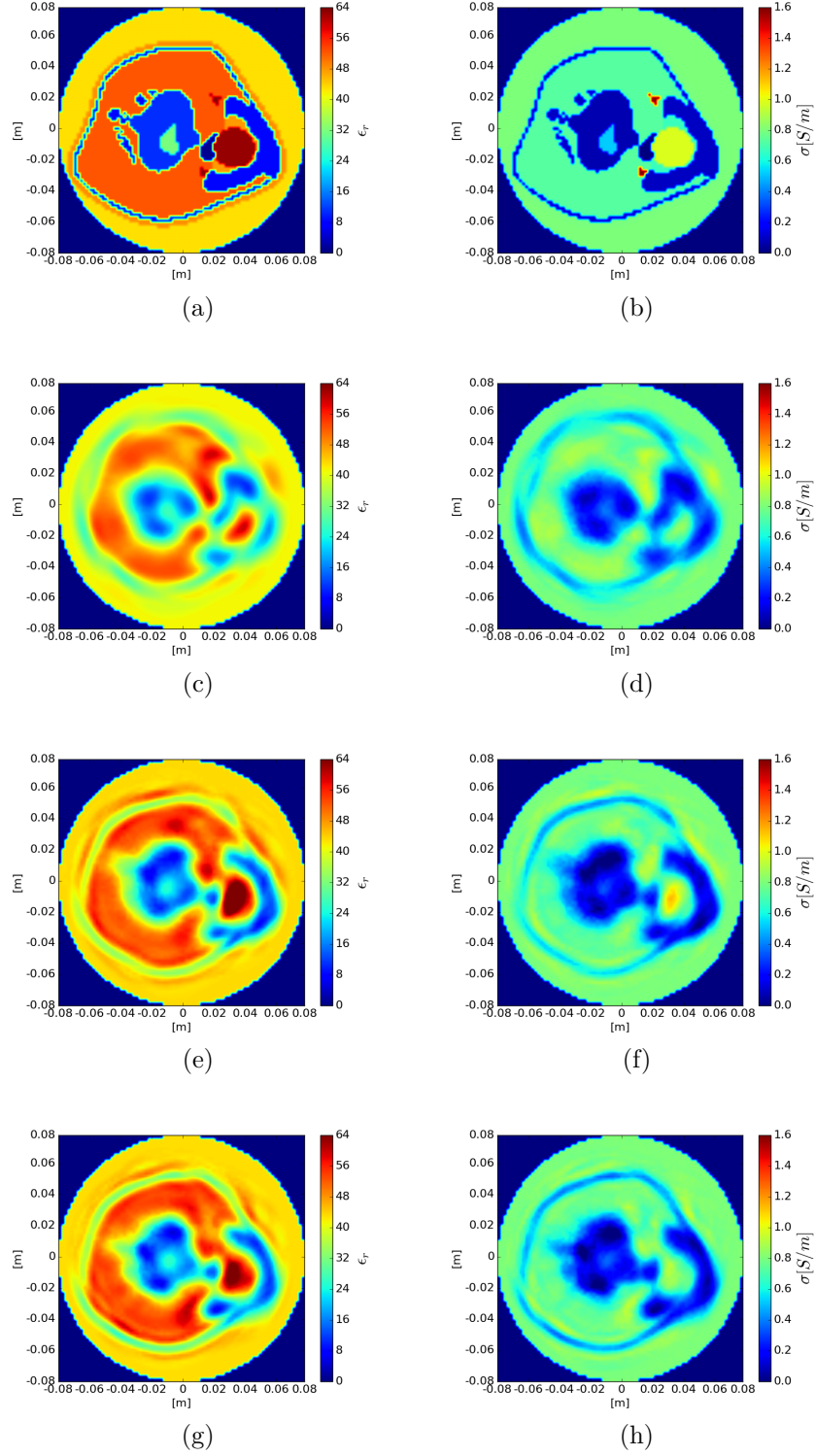
Figure 4.10: Five-tissues neck configuration. (a) Actual relative dielectric permittivity and (b) electric conductivity. Reconstructions obtained with $L = 4$ and $D = 128$. $SNR = 5$ dB [(c) ϵ_r and (d) σ]. $SNR = 15$ dB [(e) ϵ_r and (f) σ]. $SNR = 25$ dB [(g) ϵ_r and (h) σ].
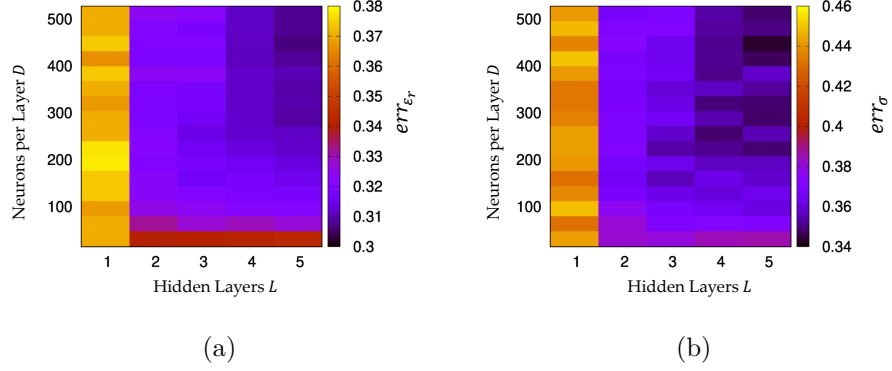
Figure 4.11: Mean reconstruction error on (a) ϵ_r and (b) σ versus the number of L hidden layers and D neurons [108].

Following this preliminary analysis, quantitative reconstructions of the cross section of neck are analyzed with different values of L and D. In particular, three different network topologies are tested against two selected cases from the validation set.

The actual values of the relative dielectric permittivity and electric conductivity in the first case are shown in Figure 4.12 (a) and Figure 4.12 (b), respectively. The neck cross section, in this configuration, presents each biological tissue in a normal physiological condition, without any tumor. The first tested network topology is characterized by $L = 1$ and $D = 32$ (i.e., the simplest network architecture). Figure 4.12 (c)-(d) report the reconstructed maps of the relative dielectric permittivity and of the electric conductivity, which are not very accurate in this case. Indeed, the ϵ_r value of the infiltrated fat near the cartilage is overestimated ($24 - 32$ vs. the actual values of $8 - 15$), the blood vessels are not well detected, and the subcutaneous fat thickness is larger than in the actual configuration. The same considerations hold for the σ reconstruction. The second tested network topology is characterized by $L = 3$ and $D = 224$, a slightly more complex neural network structure. The reconstructions obtained with this network are shown in Figure 4.12 (e)-(f). Now, the reconstructions are more precise: the thickness of the subcutaneous fat is close to its true value for both ϵ_r and σ; the cartilage is better shaped, and the trachea is well retrieved. On the other hand, the reconstructions show some artefacts outside the neck, in the matching medium, and in the relative dielectric permittivity overall. The last considered neural network has $L = 5$ and $D = 448$, and it shows the best results of the err_{ϵ_r} and err_σ errors. The reconstructed maps of the relative dielectric permittivity and electric conductivity are plotted in Figure 4.12 (g) and Figure 4.12 (h). With this network architecture, the reconstructions are better than those obtained with the previous topologies. Here, in both reconstructions of ϵ_r and σ, the

Figure 4.12: Nine-tissues neck configuration without tumor, validation case: (a) Actual relative dielectric permittivity and (b) electric conductivity. Reconstruction with $L = 1$ and $D = 32$ of (c) relative dielectric permittivity and (d) electric conductivity; reconstruction with $L = 3$ and $D = 224$ of (e) relative dielectric permittivity and (f) electric conductivity; reconstruction with $L = 5$ and $D = 448$ of (g) relative dielectric permittivity and (h) electric conductivity [108].

Figure 4.13: Nine-tissues neck configuration with tumor, validation case: (a) Actual relative dielectric permittivity and (b) electric conductivity. Reconstruction with $L = 1$ and $D = 32$ of (c) relative dielectric permittivity and (d) electric conductivity; reconstruction with $L = 3$ and $D = 224$ of (e) relative dielectric permittivity and (f) electric conductivity; reconstruction with $L = 5$ and $D = 448$ of (g) relative dielectric permittivity and (h) electric conductivity [108].

blood vessels are well identified, the cartilage shape reproduces well the real one and the thickness of the subcutaneous fat is reconstructed correctly. Moreover, the spinal cord shape is detected, and the artifacts visible in the previous reconstructions are less evident.

To test the ability to detect the presence of a tumor, a second case extracted from the validation set is analyzed. This case is a cross section of the neck with a tumor in the anterior neck part, as shown in Figure 4.13 (a)-(b). In this configuration, too, the reconstructions are evaluated for three different network architectures, as explained previously. For the first neural network, Figure 4.13 (c)-(d) report the reconstructed maps of the dielectric properties ϵ_r and σ. As before, the reconstructions are not very precise, with an overestimation of subcutaneous fat thickness, the absence of blood vessels, and an incorrect tumor shape. The reconstructions achieved with the second neural network, as can be seen in Figure 4.13 (e)-(f), highlight a significant improvement of results. The tumor is better reconstructed, as well as fat, both for dielectric and geometric properties.

Finally, the last neural network is tested, with $L = 5$ and $D = 448$, and the corresponding reconstructions can be found in Figure 4.13 (g)-(h). Now, the external shape of the neck is better retrieved than in the previous cases [Figure 4.13 (c), (d), (e), (f)]. Moreover, the tumor is identified with its correct shape and the cartilage around it is identified correctly. The trachea is now detected, although the dielectric permittivity is overestimated and assumes values similar to those of the fat. However, this fact does not prevent the identification of the tumor. Moreover, the spinal cord is properly recognized inside the vertebral bone, too, both in the relative dielectric permittivity and electric conductivity (e.g., estimated values of $25 - 35$ vs. the actual values of $30 - 40$). It is worth noting that in general, the dielectric properties of the muscle and tumor tissues may overlap. However, the considered laryngeal tumors are usually located in the anterior part of the neck and near the cartilage, where there is a reduced presence of muscle tissue. In this case, it is still possible to identify the presence of anomalies/tumors in reconstructed images, as confirmed by Figure 4.13.

After this preliminary analysis, a network with $L = 5$ hidden layers and $D = 448$ neurons has been selected for the training procedure and to test different cases with and without tumor.

To prove the robustness of the approach, the identified network is tested on realistic numerical neck phantoms extracted from the Virtual Family numerical phantoms [112]. Five test cases are created to assess the capability of discriminating the presence, size and position of the tumor. The dielectric properties of neck tissues are related to the frequency of 750 MHz, and the tumor properties are set to $\epsilon_r = 58$
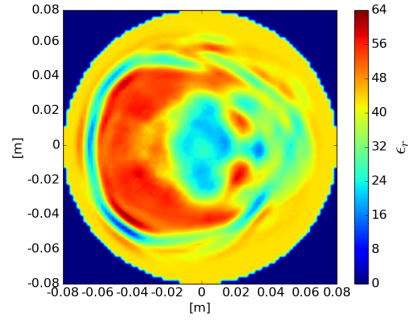
(a)
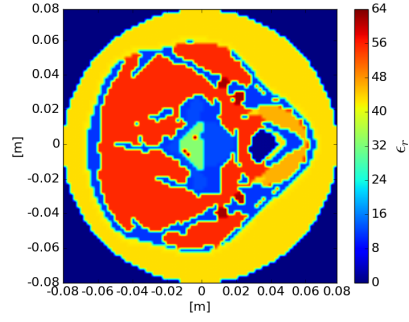
(b)
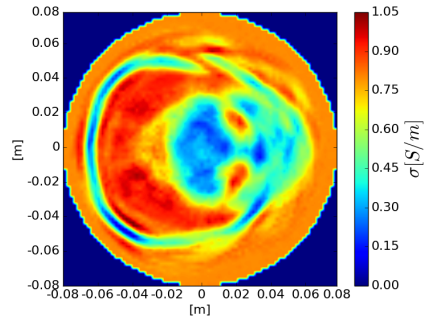
(c)
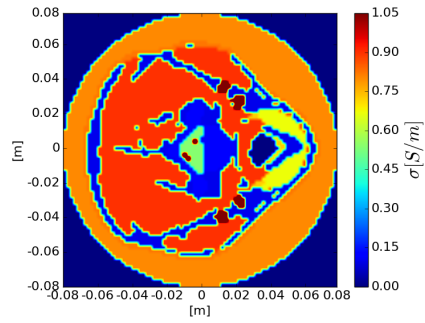
(d)

Figure 4.14: Realistic neck configuration without tumor (Test case #1). Relative dielectric permittivity: (a) Reconstructed values; (b) Actual configuration. Electric conductivity:(c) Reconstructed values; (d) Actual configuration. [108].
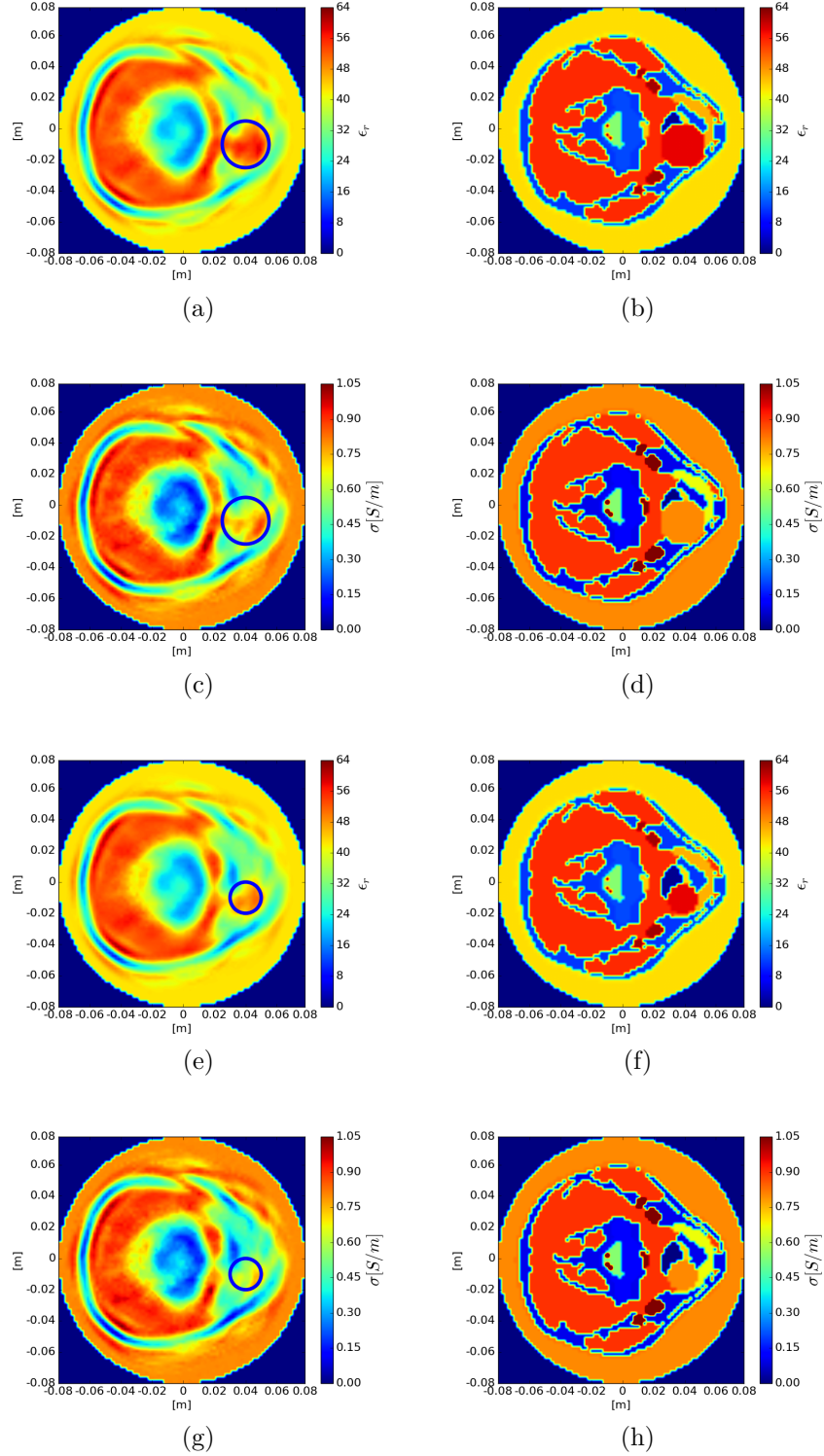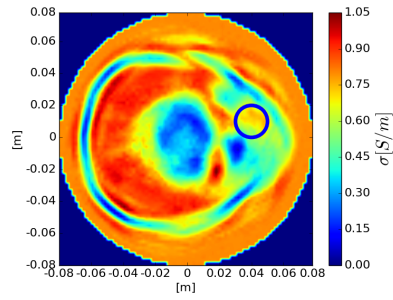
Figure 4.15: Realistic neck configuration with tumor centered in $(40, -10)$ mm. Test case #2, tumor radius $r_t = 15$ mm: (a) Reconstructed and (b) actual relative dielectric permittivity; (c) Reconstructed and (d) actual electric conductivity. Test case #3, tumor radius $r_t = 10$ mm: (e) Reconstructed and (f) actual relative dielectric permittivity; (g) Reconstructed and (h) actual electric conductivity. [108].

and $\sigma = 0.8$ [S/m], according to [116], [124].

First, a case without tumor is considered, to check the ability to reconstruct the dielectric properties in a healthy situation (Test case #1). Figure 4.14 (a)-(c) show the reconstructions of the relative dielectric permittivity and the electric conductivity, respectively. The actual configurations related to such a case are presented in Figure 4.14 (b)-(d). In the map of ϵ_r, the neural network is able to detect the vertebral bone, the spinal cord inside it, as well as the external shape of the neck. Moreover, in the reconstruction of the electric conductivity, the trachea is quite well detected. In both reconstructions the absence of tumor is verified. Successively, four cases with tumor-like inclusions are tested. Two different dimensions of the tumor, with the same center, are evaluated. In the first configuration (Test case #2), a circular target of radius equal to $r_t = 15$ mm representing the tumor was included. Figure 4.15 (a) and Figure 4.15 (c) represent the reconstructed distributions of the relative dielectric permittivity and electric conductivity, respectively. The tumor is well detected and characterized. Moreover, the external shape of the neck follows the real one, and the vertebral bone is detected. The corresponding actual neck configuration is shown in Figure 4.15 (b)-(d). In the second tumor-affected case (Test case #3), a smaller tumor is considered, with radius equal to $r_t = 10$ mm. Figure 4.15 (e)-(g) show the reconstructed dielectric properties, whereas the actual neck properties are reported in Figure 4.15 (f)-(h). In both test cases, the tumor is centered at $(40, -10)$ mm. The reconstructed maps of the dielectric properties allow the discrimination between the two different tumor sizes, with better results for the relative dielectric permittivity. Furthermore, the external shape of the neck is well reconstructed, as well as its main tissues, i.e., vertebral bone, trachea, spinal cord, and subcutaneous fat. On the other hand, in both cases the infiltrated fat near the vertebral bone in the posterior part of the neck is not identified.

To test the ability to discriminate different tumor positions, other two cases are evaluated. Figure 4.16 (a) and Figure 4.16 (b) show the reconstructed maps of ϵ_r and σ, respectively, with radius of tumor equal to $r_t = 15$ mm (Test case #4). Figure 4.16 (c)-(d) present the reconstructions with tumor radius equal to $r_t = 10$ mm (Test case #5). In these two situations, the tumor is centered at $(40, 10)$ mm. Again, the tumor-like inclusion, the vertebral bone and the internal spinal cord are detected, and the trachea is localized in the correct position. The external boundary of the neck follows the expected shape, as well as the subcutaneous fat. As before, the infiltrated fat near the bone is not detected.
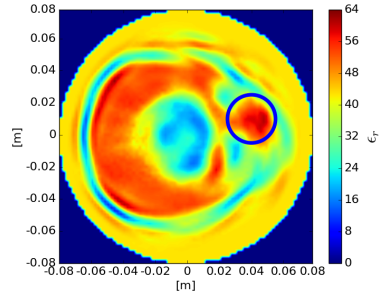
(a)
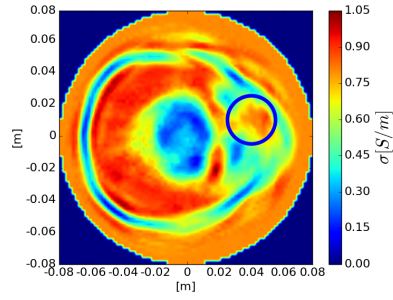
(b)
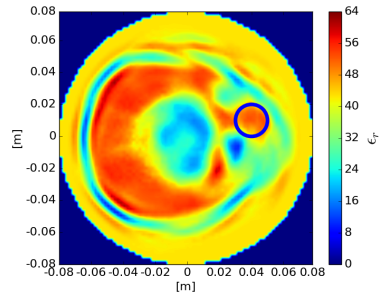
(c)

(d)

Figure 4.16: Realistic neck configuration with tumor centered in $(40, 10)$ mm. Test case #4, tumor radius $r_t = 15$ mm: Reconstructed map of (a) relative dielectric permittivity; (b) electric conductivity. Test case #5, tumor radius $r_t = 10$ mm: Reconstructed map of (c) relative dielectric permittivity; (d) electric conductivity [108].

Test case	err_{ϵ_r}	err_σ
#1	0.3082	0.3459
#2	0.3004	0.3446
#3	0.3071	0.3508
#4	0.2987	0.3428
#5	0.3044	0.3470

Table 4.3: Reconstruction errors for the considered test cases [108].

In Table 4.3, the reconstruction errors on relative dielectric permittivity err_{ϵ_r} and electric conductivity err_σ for each test case are shown. The errors are calculated using equation (4.7) and represent the normalized root mean square errors on the relative dielectric permittivity and on the electric conductivity, respectively. As confirmed by these errors, the dielectric reconstructions are more accurate for the relative dielectric permittivity than the electric conductivity. In summary, the reconstructed distributions of the dielectric properties show that, at least in the considered cases, the neural network is able to reconstruct different dimensions of tumor, for the same position, and also to localize it inside the neck.

For completeness, the estimated values of the center and the radius of the tumor in the four cases are calculated (the latter obtained by setting a threshold equal to 80% on the value of ϵ_r of the tumor). Table 4.4 reports the estimated values of both the radius of the tumor and of its center. As can be seen, both the radius size and the center are well reconstructed, also considering that a quite coarse discretization of 2 mm has been adopted.

Finally, also with this complex dataset, the results are evaluated changing the value of the SNR of the noise added to the computed fields for the test case. Specifically, other ten test cases are used. The first five considered test cases shown the tumor with the same center position. In particular, the radius r_t has been varied between 8 and 16 mm, with step of 2 mm, and its center is located in $(43, 10)$ mm.

Test case	Actual radius r_t [mm]	Estimated radius r_t [mm]	Actual center (x_0, y_0) [mm]	Estimated center (x_0, y_0) [mm]
#2	15	14.2	(40,-10)	(42.31,-7.25)
#3	10	11.6	(40,-10)	(42.62,-10.48)
#4	15	14.7	(40,10)	(43.77,8.28)
#5	10	9.2	(40,10)	(44.21,10.86)

Table 4.4: Estimated and actual tumor radius and center in different test cases.

Test case	$SNR = 35$ dB [mm]	$SNR = 15$ dB [mm]	Correct radius r_t
#6	6	3	8
#7	9	8	10
#8	11	15	12
#9	14	14.5	14
#10	15.5	15	16
#11	9	8.3	8
#12	9	9	10
#13	12	13.5	12
#14	16	16	14
#15	17.5	16.2	16

Table 4.5: Estimated radius of the tumor for different values of SNR [125].

Other five test cases are considered, in which the center is located in $(43, -10)$ mm. The radius r_t is again varied in the range $[8, 16]$ mm. The network is tested in the same configurations used for the previous cases, i.e., with $L = 5$ and $D = 448$. Two different values of SNR are considered, i.e., 15 dB and 35 dB. The results are summarized in Table 4.5. As expected, slightly worse estimations of the tumor dimensions are obtained for the lower value of SNR, especially for small sizes of the inclusion.

4.4 Experimental Results

In this Section, preliminary experimental results are introduced. Three different experimental test cases are proposed, and for each case a different numerical dataset is developed for the training procedure. The adopted microwave imaging system is described in Section 3.5.2 and shown in Figure 4.17. $F = 4$ frequencies between 600 and 750 MHz with 50 MHz frequency step are considered for the first two test cases, whereas for the third case $F = 7$ frequencies between 600 and 900 MHz are used. The network parameters used in the training phase are the same of the previous numerical cases, in particular $L = 5$ and $D = 448$.

For these experimental data, the aim is to detect just the inner inclusion present in each test case. For this reason, in the follow, the obtained reconstructions will exhibit differential values, $\Delta \epsilon_r$ and $\Delta \sigma$. In particular, $\Delta \epsilon_r^i = \epsilon_{r_{act}}^i - \epsilon_{r_{ref}}^i$ and $\Delta \sigma^i = \sigma_{act}^i - \sigma_{ref}^i$, where $\epsilon_{r_{act}}^i$ and σ_{act}^i represent the values of the relative dielectric permittivity and the electric conductivity, respectively, of the actual test case in the ith subdomain $(i = 1, \ldots, I_{tot})$. On the other hand, $\epsilon_{r_{ref}}^i$ and σ_{ref}^i are the values of the relative
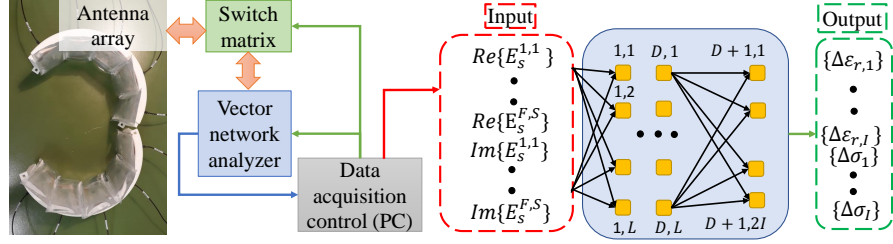
Figure 4.17: Structure of the proposed microwave imaging system and of the inversion approach based on a fully connected neural network [126]

dielectric permittivity and the electric conductivity, respectively, of the reference configuration of the test case in the ith subdomain ($i = 1, \ldots, I_{tot}$). In general, the reference configuration corresponds with the test case without the inclusion.

In the first case, the simplified beaker proposed in Section 3.5.2 is used as test case, in which a circular inclusion with radius $r_p = 8.5$ mm is placed at $(23, 3)$ mm. The network is trained using a dataset of $K = 10,000$ numerically simulated configurations. Each neck phantom is modeled as a circular cylinder with radius $r_n = 6.2$ cm (to account for beaker and matching medium) and fixed dielectric properties $\epsilon_{mm} = 43\epsilon_0$ and $\sigma_{mm} = 0.8$ S/m [101], in which a cylindrical inclusion with random radius $r_{tr1} \in (5, 10)$ mm and position (inside the beaker) is present. The inclusion simulates the spinal cord, so, as seen in the Table 4.1, the dielectric permittivity randomly ranges from $30\epsilon_0$ to $40\epsilon_0$ and its electric conductivity in the range [0.4,0.7] S/m. The investigation domain Ω_t correspond with the circular cylinder with radius r_n. It is discretized into $I_{tot} = 3024$ square cells of side 2 mm. In the training phase, a subset of 90% of samples is considered and the remaining ones are used for validation. In this case, the reference configuration is a homogenous circular structure with dielectric properties equal to those of the matching medium.

With the experimental data, a scattered-field calibration is needed [105]. For applying this procedure, a known experimental and simulated configuration is required, in particular the fields measured in the presence of a known target are used to derive a set of scaling coefficients, one for each transmitter-receiver pair and frequency. The calibrated measurements are then obtained as $E_s^{s,f,m} = E_s^{s,f,m,ME} E_s^{s,f,m,SI,R} / E_s^{s,f,m,ME,R}$, where $E_s^{s,f,m,ME}$ are the uncalibrated data, and $E_s^{s,f,m,ME,R}$, $E_s^{s,f,m,SI,R}$ are the experimental and simulated fields for the known configuration. For this first test case, the known calibration target is a circular inclusion with radius $r_{g1} = 6.2$ mm that has been placed inside the beaker at $(23, 5)$ mm. The reconstructions of $\Delta\epsilon_r$ and $\Delta\sigma$ are reported in Figure 4.18 (b) and Figure 4.18 (c). The internal inclusion is correctly localized, and a quite good estimation of the dielectric properties is obtained,

although $\Delta\epsilon_r$ is underestimated.

The second test case [Figure 4.18 (d)] is the 3D-printed model of the human neck described previously ("Phantom 1" of Section 3.5.1). In particular, an inclusion with radius $r_{g2} = 12.4$ mm is placed inside the neck phantom at (10,5) mm. In this case, a dataset built from a numerical model of the phantom (containing the external layer and the trachea) is considered. An inclusions with different random positions (inside the inner part) and radius $r_{tr2} \in (3, 15)$ mm have been located to generate different neck phantoms. The dielectric properties vary in the same ranges of the previous case and the PLA structure is simulated as seen in the Section 3.5.1. The reference scenario is the phantom without inclusions. To calibrate the data, the known target is an inclusion with radius $r_{g3} = 5$ mm and placed at (10, 9) mm. The reconstructed values of $\Delta\epsilon_r$ and $\Delta\sigma$ are shown in Figure 4.18 (e)-(f). In this case, too, the inclusion is well detected, although $\Delta\epsilon_r$ is slightly overestimated and $\Delta\sigma$ is underestimated.

Finally, a more complex 3D-printed model with vertebral column filled with glycerin ($\epsilon_{ver} = 9.77\epsilon_0, \sigma_{ver} = 0.36$ S/m) is considered ["Phantom 2" of Section 3.5.1, Figure 4.18 (g)]. The considered test case is a circular printed inclusion inside the vertebral bone with radius $r_{v2} = 5$ mm and located at (0.5, 0) mm. In this case, the neck phantoms in the training set reproduce the external printed structure and the vertebral bone and contain random inclusions inside the vertebra with radius in the range $r_{tr3} \in (3, 12)$ mm. The ranges of the dielectric properties of the average neck are the same as before, whereas the ϵ_r and σ of the bone range between 10 and 20 and 0.006 and 0.2, respectively (see Table 4.2). Also in this case, the structure without inclusion is used as reference scenario. To calibrate the data, an inclusion with radius $r_{v1} = 9$ mm is considered inside the vertebra at (5, 0) mm. The reconstructed maps of the dielectric properties are shown in Figure 4.18 (h)-(i). Even in this more involving case, the inclusion is well detected in both $\Delta\epsilon_r$ and $\Delta\sigma$, and the reconstructed values are quite accurate.

For completeness, the performances of the approach are evaluated using different error quantities, to quantify the reconstruction errors of the dielectric properties and also the error in the position and radius size of the inclusion. In particular, the mean relative errors, calculated as

$$e_{\{tot,b,in\},\gamma} = \frac{1}{I_{\{tot,b,in\}}} \sum_{\mathbf{r}_i \in \Omega_{\{t,b,in\}}} \frac{|\gamma_{rec}(\mathbf{r}_i) - \gamma_{act}(\mathbf{r}_i)|}{|\gamma_{act}(\mathbf{r}_i)|} \tag{4.9}$$

are used to evaluate the reconstruction error of the dielectric properties in the total, background and inclusion region. Moreover, γ_{rec} and γ_{act} are the reconstructed and actual values of $\Delta\epsilon_r$ or $\Delta\sigma$, r_i is the center of the ith cell of the investigation
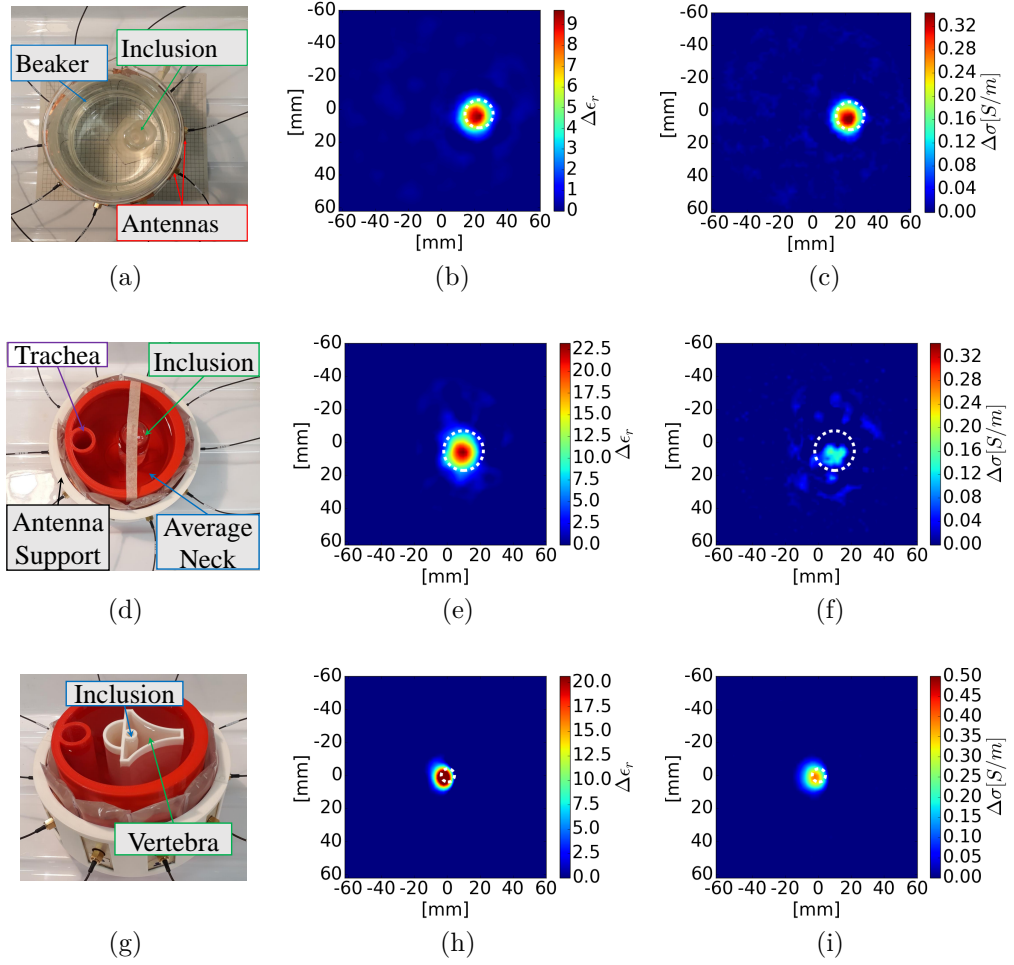
Figure 4.18: Configuration of the experimental target and reconstructed maps. Beaker: (a) picture of the phantom, reconstructions of (b) $\Delta\epsilon_r$ and (c) $\Delta\sigma$. 3-D printed neck "Phantom 1" [101]: (d) picture of the phantom, reconstructions of (e) $\Delta\epsilon_r$ and (f) $\Delta\sigma$. 3-D printed neck "Phantom 2" [101]: (g) picture of the phantom, reconstructions of (h) $\Delta\epsilon_r$ and (i) $\Delta\sigma$ [126].

domain, $\Omega_{\{b,in\}}$ is the background (b) or the inclusion (in) region, and $I_{b,in}$ is the corresponding number of cells. The relative errors on the estimated radius and center of the inclusion have been evaluated as dimensionless quantities. In particular, the radius error, e_r, is computed as

$$e_r = |r_r - r_a|/|r_a| \qquad (4.10)$$

where r_a and r_r are the actual and estimated radiuses, the latter obtained by setting a threshold equal to 40% on the maximum reconstructed value of $\Delta\epsilon_r$. The position errors, $e_{cd,x}$ and $e_{cd,y}$, are calculate as the center errors along the x and y coordinates of the reconstructed inclusion. For the three considered cases, in Table 4.6 the

75

Case	e_{tot,ϵ_r}	$e_{tot,\sigma}$	e_{b,ϵ_r}	$e_{b,\sigma}$	e_{in,ϵ_r}	$e_{in,\sigma}$	e_r	$e_{cd,x}$	$e_{cd,y}$
#1	0.007	0.013	0.004	0.008	0.169	0.259	0.001	0.026	0.100
#2	0.011	0.033	0.006	0.008	0.141	0.703	0.146	0.013	0.048
#3	0.008	0.006	0.006	0.005	0.262	0.328	0.250	0.020	0.001

Table 4.6: Relative reconstruction errors (dimensionless) [126].

calculated errors are reported. In the second configuration, e_{tot,ϵ_r} and $e_{tot,\sigma}$ and e_{b,ϵ_r} and $e_{b,\sigma}$ are slightly higher than in the first case, and it is expected given the higher complexity of the second configuration. Indeed, in Figure 4.18 (e)-(f) some artifacts in the background are present. Moreover, $e_{in,\sigma}$ is about twice the value of the first case, and this is motivated by the underestimation of the reconstructed values of $\Delta\sigma$. In all cases, the inclusion is correct detected, both in size and position, and it is highlighted by the obtained low radius and position errors. These results shown the possibility to identify and locate the inclusion suitably. In the last test case, errors are generally comparable with the simplest configuration even though the highest complexity in the configuration. In fact, the inclusion position in the training set changes few inside the vertebral bone.

Finally, for the test cases #1 and #2, the values of dielectric properties outside the inclusion are changed of $\pm5\%$ of the previously considered ones. This analysis allows to verified if the obtained results are influenced from the selected values of the dielectric properties. In particular, the average increase in the relative errors is 2.45% for e_{tot,ϵ_r} and 9.15% for $e_{tot,\sigma}$. This errors highlighted that the results are quite good also with a change of $\pm5\%$ in the dielectric properties.

Chapter 5

Conclusions

In this Thesis, two approaches to microwave imaging for medical diagnostics have been proposed. In particular, they have been focused on two different neck pathologies: The cervical myelopathy and the presence of neck tumors.

The first disease has been addressed by using an inexact-Newton strategy with regularization performed in the framework of the L^p Banach spaces. Different numerical neck phantoms have been considered and used to simulate the pathological conditions. Some numerical simulations have been performed and the obtained results have been discussed. In particular, the capabilities of retrieving the spinal cord with different sizes (the size is correlated to the health or pathological status of the patient) have been evaluated. Moreover, some experimental reconstructions have also been reported. To this end, an imaging system working at microwave frequencies for spinal cord diagnostics has been used. The prototype includes a set of antennas that can be positioned around the patient's neck. Different experimental neck phantoms have been used with increasing structural complexity. Firstly, a beaker has been used for the neck and pipes simulate the presence of the spinal cord. Then, a quite realistic neck phantom has been constructed by using a 3D printed. Although preliminary, these results seem to indicate the potentialities of microwave imaging techniques in detecting significant changes in the spinal cord size, which may be symptoms of cervical myelopathy. Indeed, the diameters of the cord, estimated from the retrieved images, seem to allow discriminating between the normal and pathologic conditions.

Furthermore, a hybrid inverse scattering procedure, based on the combination of a qualitative delay-and-sum focusing technique with a quantitative Newton scheme in Lebesgue spaces, has been developed and tested. The obtained experimental results shown the possibility to identify, localize, and shape the inclusion with quite good accuracy.

The second approach discussed in this document concerns the solution of the

electromagnetic inverse scattering problem by using a fully-connected neural network. This technique has been considered as a potential diagnostic method for neck tumor detection. To train the neural network, a set of synthetic neck phantoms has been constructed. The aim was to reconstruct the distribution of dielectric properties of a cross section of the neck starting from the measured samples of the scattered electric field. The phantoms are randomly generated and includes different biological tissues that mimic rather realistically the human neck. A preliminary numerical analysis has been performed to select the network parameters, considering various architectures with different numbers of hidden layers and neurons per layer. The obtained "best" neutral network has been used to evaluate the reconstruction capabilities of the approach. The obtained results, although very preliminary, seem to indicate the possibility of detecting neck tumors by using microwave imaging techniques.

Finally, initial experimental tests have been performed also by using this new approach. In order to perform these tests, due to the lack of experimental data for the training phase of the procedure, numerical simulations have been adopted, whereas the experimental data have been used in the testing phase. Three different phantoms, with different inclusions, have been considered and the preliminary results, although initial ones, seem to be very promising. In all cases, the position, dimensions, and dielectric properties of the inclusions are identified with a rather good accuracy.

Concerning the possible future developments of the research activity in the field of application of microwave imaging techniques for neck diagnostics, a strong effort should be dedicated to all the aspects considered in the present work. In particular, significant advances can be expected by improving the effectiveness of the experimental microwave system, as well as by introducing even more realistic neck phantoms. Obviously, clinical trials will be necessary to finally evaluate the capabilities and limitations of the approach. Concerning the diagnostic technique based on machine learning, the continuous progresses of the research in this field are expected to suggest the use of new and increasingly effective neural network architectures.

List of Figures

List of Tables

Bibliography

[1] M. Pastorino and A. Randazzo. *Microwave imaging methods and applications*. Artech House, 2018 (cit. on pp. 1, 7–8, 20).

[2] A. Benedetto and L. Pajewski. *Civil engineering applications of ground penetrating radar*. Springer, 2015 (cit. on p. 1).

[3] I. Giannakis, F. Tosti, L. Lantini, and A. M. Alani. "Diagnosing emerging infectious diseases of trees using ground penetrating radar". *IEEE Transactions on Geoscience and Remote Sensing* 58.2 (2019), pp. 1146–1155 (cit. on p. 1).

[4] F. Boero, A. Fedeli, M. Lanini, M. Maffongelli, R. Monleone, M. Pastorino, A. Randazzo, A. Salvade, and A. Sansalone. "Microwave tomography for the inspection of wood materials: imaging system and experimental results". *IEEE Transactions on Microwave Theory and Techniques* 66.7 (2018), pp. 3497–3510 (cit. on p. 1).

[5] J. Laviada, B. Wu, M. T. Ghasr, and R. Zoughi. "Nondestructive evaluation of microwave-penetrable pipes by synthetic aperture imaging enhanced by full-wave field propagation model". *IEEE Transactions on Instrumentation and Measurement* 68.4 (2018), pp. 1112–1119 (cit. on p. 1).

[6] G. Bozza, C. Estatico, A. Massa, M. Pastorino, and A. Randazzo. "Short-range image-based method for the inspection of strong scatterers using microwaves". *IEEE Transactions on Instrumentation and Measurement* 56.4 (2007), pp. 1181–1188 (cit. on p. 1).

[7] S. Pisa, E. Piuzzi, E. Pittella, P. D'Atanasio, A. Zambotti, and G. Sacco. "Comparison between delay and sum and range migration algorithms for image reconstruction in through-the-wall radar imaging systems". *IEEE Journal of Electromagnetics, RF and Microwaves in Medicine and Biology* 2.4 (2018), pp. 270–276 (cit. on p. 1).

[8]   S. Di Meo, P. F. Espin-Lopez, A. Martellosio, M. Pasian, G. Matrone, M. Bozzi, G. Magenes, A. Mazzanti, L. Perregrini, F. Svelto, et al. "On the feasibility of breast cancer imaging systems at millimeter-waves frequencies". *IEEE Transactions on Microwave Theory and Techniques* 65.5 (2017), pp. 1795–1806 (cit. on p. 1).

[9]   M. Ambrosanio, P. Kosmas, and V. Pascazio. "A multithreshold iterative DBIM-based algorithm for the imaging of heterogeneous breast tissues". *IEEE Transactions on Biomedical Engineering* 66.2 (2018), pp. 509–520 (cit. on p. 1).

[10]   G. Boverman, C. E. Davis, S. D. Geimer, and P. M. Meaney. "Image registration for microwave tomography of the breast using priors from nonsimultaneous previous magnetic resonance images". *IEEE Journal of Electromagnetics, RF and Microwaves in Medicine and Biology* 2.1 (2017), pp. 2–9 (cit. on p. 1).

[11]   M. Asefi, A. Zakaria, and J. LoVetri. "Microwave imaging using normal electric-field components inside metallic resonant chambers". *IEEE Transactions on Microwave Theory and Techniques* 65.3 (2016), pp. 923–933 (cit. on p. 1).

[12]   L. M. Neira, B. D. Van Veen, and S. C. Hagness. "High-resolution microwave breast imaging using a 3-D inverse scattering algorithm with a variable-strength spatial prior constraint". *IEEE Transactions on Antennas and Propagation* 65.11 (2017), pp. 6002–6014 (cit. on p. 1).

[13]   D. Tajik, F. Foroutan, D. S. Shumakov, A. D. Pitcher, and N. K. Nikolova. "Real-time microwave imaging of a compressed breast phantom with planar scanning". *IEEE Journal of Electromagnetics, RF and Microwaves in Medicine and Biology* 2.3 (2018), pp. 154–162 (cit. on p. 1).

[14]   A. Abubakar, P. M. Van den Berg, and J. J. Mallorqui. "Imaging of biomedical data using a multiplicative regularized contrast source inversion method". *IEEE Transactions on Microwave Theory and Techniques* 50.7 (2002), pp. 1761–1771 (cit. on p. 1).

[15]   T. Henriksson, N. Joachimowicz, C. Conessa, and J. Bolomey. "Quantitative microwave imaging for breast cancer detection using a planar 2.45 GHz system". *IEEE Transactions on Instrumentation and Measurement* 59.10 (2010), pp. 2691–2699 (cit. on p. 1).

[16]   Z. Miao and P. Kosmas. "Multiple-frequency DBIM-TwIST algorithm for microwave breast imaging". *IEEE Transactions on Antennas and Propagation* 65.5 (2017), pp. 2507–2516 (cit. on p. 1).

[17] G. Bellizzi, G. G. Bellizzi, O. M. Bucci, L. Crocco, M. Helbig, S. Ley, and J. Sachs. "Optimization of the working conditions for magnetic nanoparticle-enhanced microwave diagnostics of breast cancer". *IEEE Transactions on Biomedical Engineering* 65.7 (2017), pp. 1607–1616 (cit. on p. 1).

[18] H. Trefna and M. Persson. "Antenna array design for brain monitoring". *2008 IEEE Antennas and Propagation Society International Symposium* (2008), pp. 1–4 (cit. on p. 1).

[19] S. Y. Semenov and D. R. Corfield. "Microwave tomography for brain imaging: Feasibility assessment for stroke detection". *International Journal of Antennas and Propagation* 2008 (2008) (cit. on p. 1).

[20] L. Crocco, I. Karanasiou, M. L. James, and R. C. Conceição. *Emerging electromagnetic technologies for brain diseases diagnostics, monitoring and therapy.* Springer, 2018 (cit. on p. 1).

[21] A. Zakaria, A. Baran, and J. LoVetri. "Estimation and use of prior information in FEM-CSI for biomedical microwave tomography". *IEEE Antennas and Wireless Propagation Letters* 11 (2012), pp. 1606–1609 (cit. on p. 1).

[22] D. Gibbins, D. Byrne, T. Henriksson, B. Monsalve, and I. J. Craddock. "Less Becomes More for Microwave Imaging: Design and Validation of an Ultrawide-Band Measurement Array." *IEEE Antennas and Propagation Magazine* 59.5 (2017), pp. 72–85 (cit. on p. 1).

[23] A. Darvazehban, S. A. Rezaeieh, A. Zamani, and A. M. Abbosh. "Pattern reconfigurable metasurface antenna for electromagnetic torso imaging". *IEEE Transactions on Antennas and Propagation* 67.8 (2019), pp. 5453–5462 (cit. on p. 1).

[24] P. M. Meaney, D. Goodwin, A. H. Golnabi, T. Zhou, M. Pallone, S. D. Geimer, G. Burke, and K. D. Paulsen. "Clinical microwave tomographic imaging of the calcaneus: a first-in-human case study of two subjects". *IEEE Transactions on Biomedical Engineering* 59.12 (2012), pp. 3304–3313 (cit. on p. 1).

[25] M. Pastorino. *Microwave imaging.* Vol. 208. John Wiley & Sons, 2010 (cit. on pp. 2, 12–15, 18, 23).

[26] X. Li and S. C. Hagness. "A confocal microwave imaging algorithm for breast cancer detection". *IEEE Microwave and wireless components letters* 11.3 (2001), pp. 130–132 (cit. on p. 2).

[27] I. Catapano, L. Crocco, and T. Isernia. "Improved sampling methods for shape reconstruction of 3-D buried targets". *IEEE Transactions on Geoscience and Remote Sensing* 46.10 (2008), pp. 3265–3273 (cit. on p. 2).

[28] M. T. Bevacqua, T. Isernia, R. Palmeri, M. N. Akinci, and L. Crocco. "Physical insight unveils new imaging capabilities of orthogonality sampling method". *IEEE Transactions on Antennas and Propagation* 68.5 (2020), pp. 4014–4021 (cit. on p. 2).

[29] A. Fedeli, C. Estatico, M. Pastorino, and A. Randazzo. "Microwave detection of brain injuries by means of a hybrid imaging method". *IEEE Open Journal of Antennas and Propagation* 1 (2020), pp. 513–523 (cit. on p. 2).

[30] K. Xu, Y. Zhong, and G. Wang. "A hybrid regularization technique for solving highly nonlinear inverse scattering problems". *IEEE Transactions on Microwave Theory and Techniques* 66.1 (2017), pp. 11–21 (cit. on p. 2).

[31] C. X. Yang, J. Zhang, and M. S. Tong. "A hybrid quantum-behaved particle swarm optimization algorithm for solving inverse scattering problems". *IEEE Transactions on Antennas and Propagation* 69.9 (2021), pp. 5861–5869 (cit. on p. 2).

[32] B. Rao and L. Carin. "A hybrid scheme for inverse scattering of electrically large regions". *Radio Science* 35.2 (2000), pp. 315–329 (cit. on p. 2).

[33] A. Semnani and M. Kamyab. "An enhanced hybrid method for solving inverse scattering problems". *IEEE Transactions on Magnetics* 45.3 (2009), pp. 1534–1537 (cit. on p. 2).

[34] M. Rabbani, A. Tavakoli, and M. Dehmollaian. "A hybrid quantitative method for inverse scattering of multiple dielectric objects". *IEEE Transactions on Antennas and Propagation* 64.3 (2016), pp. 977–987 (cit. on p. 2).

[35] K. Langenberg, M Berger, T. Kreutter, K Mayer, and V Schmitz. "Synthetic aperture focusing technique signal processing". *NDT international* 19.3 (1986), pp. 177–189 (cit. on pp. 2, 26).

[36] K. J. Langenberg. "Linear scalar inverse scattering". *Scattering* (2002), pp. 121–141 (cit. on pp. 2, 26).

[37] F. Soldovieri, R. Solimene, and G Kouemou. "Ground penetrating radar subsurface imaging of buried objects". *Radar Technology* (2010), pp. 105–126 (cit. on pp. 2, 26).

[38] I. Bisio, C. Estatico, A. Fedeli, F. Lavagetto, M. Pastorino, A. Randazzo, and A. Sciarrone. "Brain stroke microwave imaging by means of a Newton-conjugate-gradient method in L^p Banach spaces". *IEEE Transactions on Microwave Theory and Techniques* 66.8 (2018), pp. 3668–3682 (cit. on pp. 2, 21, 25, 36).

[39] C. Estatico, A. Fedeli, M. Pastorino, and A. Randazzo. "Microwave imaging by means of Lebesgue-space inversion: An overview". *Electronics* 8.9 (2019), p. 945 (cit. on pp. 2–3).

[40] C. Estatico, M. Pastorino, A. Randazzo, and E. Tavanti. "Three-Dimensional microwave imaging in L^p Banach spaces: numerical and experimental results". *IEEE Transactions on Computational Imaging* 4.4 (2018), pp. 609–623 (cit. on pp. 2–3, 21, 23).

[41] I. T. Rekanos. "Inverse scattering of dielectric cylinders by using radial basis function neural networks". *Radio Science* 36.5 (2001), pp. 841–849 (cit. on p. 3).

[42] E. Bermani, S. Caorsi, and M. Raffetto. "An inverse scattering approach based on a neural network technique for the detection of dielectric cylinders buried in a lossy half-space". *Progress In Electromagnetics Research* 26 (2000), pp. 67–87 (cit. on p. 3).

[43] W. Shao and Y. Du. "Microwave imaging by deep learning network: feasibility and training method". *IEEE Transactions on Antennas and Propagation* 68.7 (2020), pp. 5626–5635 (cit. on p. 3).

[44] A. Yago, M. Cavagnaro, and L. Crocco. "Deep learning-enhanced qualitative microwave imaging: rationale and initial assessment". *2021 15th European Conference on Antennas and Propagation (EuCAP)* (2021), pp. 1–5 (cit. on p. 3).

[45] Y. Huang, R. Song, K. Xu, X. Ye, C. Li, and X. Chen. "Deep learning-based inverse scattering with structural similarity loss functions". *IEEE Sensors Journal* 21.4 (2020), pp. 4900–4907 (cit. on p. 3).

[46] H. M. Yao, L. Jiang, and E. Wei. "Enhanced deep learning approach based on the deep convolutional encoder–decoder architecture for electromagnetic inverse scattering problems". *IEEE Antennas and Wireless Propagation Letters* 19.7 (2020), pp. 1211–1215 (cit. on p. 3).

[47] L. Zhang, K. Xu, R. Song, X. Ye, G. Wang, and X. Chen. "Learning-based quantitative microwave imaging with a hybrid input scheme". *IEEE Sensors Journal* 20.24 (2020), pp. 15007–15013 (cit. on p. 3).

[48] S. D. Campbell, R. P. Jenkins, P. J. O'Connor, and D. Werner. "The explosion of artificial intelligence in antennas and propagation: how deep learning is advancing our state of the art". *IEEE Antennas and Propagation Magazine* 63.3 (2020), pp. 16–27 (cit. on p. 3).

[49] M. Li, R. Guo, K. Zhang, Z. Lin, F. Yang, S. Xu, X. Chen, A. Massa, and A. Abubakar. "Machine learning in electromagnetics with applications to biomedical imaging: a review". *IEEE Antennas and Propagation Magazine* 63.3 (2021), pp. 39–51 (cit. on p. 3).

[50] Z. Wei and X. Chen. "Physics-inspired convolutional neural network for solving full-wave inverse scattering problems". *IEEE Transactions on Antennas and Propagation* 67.9 (2019), pp. 6138–6148 (cit. on p. 3).

[51] H. M. Yao, E. Wei, and L. Jiang. "Two-step enhanced deep learning approach for electromagnetic inverse scattering problems". *IEEE Antennas and Wireless Propagation Letters* 18.11 (2019), pp. 2254–2258 (cit. on p. 3).

[52] O. Ronneberger, P. Fischer, and T. Brox. "U-net: convolutional networks for biomedical image segmentation". *International Conference on Medical Image Computing and Computer-Assisted Intervention* (2015), pp. 234–241 (cit. on p. 3).

[53] K. He, X. Zhang, S. Ren, and J. Sun. "Deep residual learning for image recognition". *Proceedings of the IEEE Conference on Computer Vision and Pattern Recognition* (2016), pp. 770–778 (cit. on p. 3).

[54] K. Simonyan and A. Zisserman. "Very deep convolutional networks for large-scale image recognition". *arXiv preprint arXiv:1409.1556* (2014) (cit. on p. 3).

[55] R. Rao. "Neck pain, cervical radiculopathy, and cervical myelopathy: pathophysiology, natural history, and clinical evaluation". *JBJS* 84.10 (2002), pp. 1872–1881 (cit. on p. 3).

[56] C. de Oliveira Vilaça, M. Orsini, M. A. A. Leite, M. R. de Freitas, E. Davidovich, R. Fiorelli, S. Fiorelli, C. Fiorelli, A. B. Oliveira, and B. L. Pessoa. "Cervical spondylotic myelopathy: what the neurologist should know". *Neurology International* 8.4 (2016), p. 6330 (cit. on p. 3).

[57]   G. D. Cramer and S. A. Darby. *Clinical anatomy of the spine, spinal cord, and ANS*. 2017 (cit. on pp. 3, 29).

[58]   E. M. Baron and W. F. Young. "Cervical spondylotic myelopathy: a brief review of its pathophysiology, clinical course, and diagnosis". *Neurosurgery* 60.1 (2007), S1–35 (cit. on p. 3).

[59]   R. Guo, J. Guo, L. Zhang, X. Qu, S. Dai, R. Peng, V. F. Chong, and J. Xian. "CT-based radiomics features in the prediction of thyroid cartilage invasion from laryngeal and hypopharyngeal squamous cell carcinoma". *Cancer Imaging* 20.1 (2020), pp. 1–11 (cit. on pp. 3, 54).

[60]   H. K. Kim, E. J. Ha, M. Han, J. Lee, and E. Y. Soh. "Reoperations for structurally persistent or recurrent disease after thyroidectomy: analysis via preoperative CT". *Scientific Reports* 10.1 (2020), pp. 1–7 (cit. on pp. 3, 54).

[61]   S. Gao, M. Zheng, X. Ren, Y. Tang, and X. Liang. "Local hyperthermia in head and neck cancer: mechanism, application and advance". *Oncotarget* 7.35 (2016), p. 57367 (cit. on pp. 3, 54).

[62]   M. M. Paulides, G. M. Verduijn, and N. Van Holthe. "Status quo and directions in deep head and neck hyperthermia". *Radiation Oncology* 11.1 (2016), pp. 1–14 (cit. on p. 3).

[63]   N. R. Datta, H. P. Kok, H. Crezee, U. S. Gaipl, and S. Bodis. "Integrating loco-regional hyperthermia into the current oncology practice: SWOT and TOWS analyses". *Frontiers in Oncology* 10 (2020), p. 819 (cit. on p. 3).

[64]   S. Y. Lee, G. Fiorentini, A. M. Szasz, G. Szigeti, A. Szasz, and C. A. Minnaar. "Quo vadis oncological hyperthermia (2020)?" *Frontiers in Oncology* 10 (2020), p. 1690 (cit. on p. 3).

[65]   J. A. Stratton. "Electromagnetic Theory McGraw-Hill". *New York* (1941), pp. 31–434 (cit. on pp. 5–6).

[66]   D. S. Jones. *The theory of electromagnetism*. Macmillan, 1964 (cit. on p. 6).

[67]   C. Gabriel. *Compilation of the dielectric properties of body tissues at RF and microwave frequencies*. Tech. rep. King's Coll London (United Kingdom) Dept. Of Physics, 1996 (cit. on p. 7).

[68]   K. R. Foster and H. P. Schwan. "Dielectric properties of tissues and biological materials: a critical review." *Critical Reviews in Biomedical Engineering* 17.1 (1989), pp. 25–104 (cit. on p. 7).

[69] H. P. Schwan and K. R. Foster. "RF-field interactions with biological systems: electrical properties and biophysical mechanisms". *Proceedings of the IEEE* 68.1 (1980), pp. 104–113 (cit. on p. 8).

[70] W. D. Hurt. "Multiterm Debye dispersion relations for permittivity of muscle". *IEEE Transactions on Biomedical Engineering* 1 (1985), pp. 60–64 (cit. on p. 9).

[71] S. Gabriel, R. W. Lau, and C. Gabriel. "The dielectric properties of biological tissues: II. Measurements in the frequency range 10 Hz to 20 GHz". *Physics in medicine & biology* 41.11 (1996), p. 2251 (cit. on p. 9).

[72] S. Gabriel, R. W. Lau, and C. Gabriel. "The dielectric properties of biological tissues: III. Parametric models for the dielectric spectrum of tissues". *Physics in Medicine & Biology* 41.11 (1996), p. 2271 (cit. on pp. 9, 31, 53–54).

[73] P. A. Hasgall, F. Di Gennaro, C. Baumgartner, E. Neufeld, B. Lloyd, M. C. Gosselin, D. Payne, A. Klingenbock, and N. Kuster. "IT IS Database for thermal and electromagnetic parameters of biological tissues, Version 4.0". *IT IS* (2018) (cit. on pp. 10, 79).

[74] C. Tai. "Dyadic Green's functions in electromagnetic theory". *PA: International Textbook* (1971) (cit. on pp. 13, 18).

[75] C. Estatico, M. Pastorino, and A. Randazzo. "A novel microwave imaging approach based on regularization in L^p Banach spaces". *IEEE Transactions on Antennas and Propagation* 60.7 (2012), pp. 3373–3381 (cit. on pp. 21, 23).

[76] A. Rieder. "On the regularization of nonlinear ill-posed problems via inexact Newton iterations". *Inverse Problems* 15.1 (1999), p. 309 (cit. on p. 21).

[77] B. Kaltenbacher, A. Neubauer, and O. Scherzer. *Iterative regularization methods for nonlinear ill-posed problems.* Vol. 6. Walter de Gruyter, 2008 (cit. on p. 21).

[78] R. S. Dembo, S. C. Eisenstat, and T. Steihaug. "Inexact newton methods". *SIAM Journal on Numerical analysis* 19.2 (1982), pp. 400–408 (cit. on p. 21).

[79] A. Abubakar, T. M. Habashy, G. Pan, and M. Li. "Application of the multiplicative regularized Gauss–Newton algorithm for three-dimensional microwave imaging". *IEEE Transactions on Antennas and Propagation* 60.5 (2012), pp. 2431–2441 (cit. on p. 22).

[80] T. Isernia, V. Pascazio, and R. Pierri. "On the local minima in a tomographic imaging technique". *IEEE Transactions on Geoscience and Remote Sensing* 39.7 (2001), pp. 1596–1607 (cit. on p. 23).

[81] F. Gao, B. D. Van Veen, and S. C. Hagness. "Sensitivity of the distorted born iterative method to the initial guess in microwave breast imaging". *IEEE Transactions on Antennas and Propagation* 63.8 (2015), pp. 3540–3547 (cit. on p. 23).

[82] D. Colton and R. Kress. *Inverse acoustic and electromagnetic scattering theory.* Vol. 93. Springer Science & Business Media, 2012 (cit. on p. 23).

[83] M. Bertero and P. Boccacci. *Introduction to inverse problems in imaging.* CRC press, 1998 (cit. on pp. 23, 25).

[84] G. H. Golub and C. F. Van Loan. *Matrix computations.* JHU press, 2013 (cit. on p. 23).

[85] E. Tavanti, C. Estatico, A. Fedeli, M. Pastorino, and A. Randazzo. "Nonlinear electromagnetic inverse scattering in via Frozen or Broyden update of the Fréchet derivative". *Journal of Physics: Conference Series* 657.1 (2015) (cit. on p. 23).

[86] T. Schuster, B. Kaltenbacher, B. Hofmann, and K. S. Kazimierski. *Regularization methods in Banach spaces.* Vol. 10. Walter de Gruyter, 2012 (cit. on pp. 23–24).

[87] A. W. Knapp. *Basic real analysis.* Springer Science & Business Media, 2005 (cit. on p. 23).

[88] F. Schöpfer, A. K. Louis, and T. Schuster. "Nonlinear iterative methods for linear ill-posed problems in Banach spaces". *Inverse Problems* 22.1 (2006), p. 311 (cit. on pp. 23–24).

[89] C. Estatico, S. Gratton, F. Lenti, and D. Titley-Peloquin. "A conjugate gradient like method for $p-$norm minimization in functional spaces". *Numerische Mathematik* 137.4 (2017), pp. 895–922 (cit. on p. 25).

[90] F. Lenti, F. Nunziata, C. Estatico, and M. Migliaccio. "Conjugate gradient method in Hilbert and Banach spaces to enhance the spatial resolution of radiometer data". *IEEE Transactions on Geoscience and Remote Sensing* 54.1 (2015), pp. 397–406 (cit. on p. 25).

[91] J. F. Epperson. *An introduction to numerical methods and analysis.* John Wiley & Sons, 2013 (cit. on p. 25).

[92] M. Salucci, G. Oliveri, and A. Massa. "GPR prospecting through an inverse-scattering frequency-hopping multifocusing approach". *IEEE Transactions on Geoscience and Remote Sensing* 53.12 (2015), pp. 6573–6592 (cit. on p. 26).

[93] W. C. Chew and J. Lin. "A frequency-hopping approach for microwave imaging of large inhomogeneous bodies". *IEEE Microwave and Guided Wave Letters* 5.12 (1995), pp. 439–441 (cit. on p. 26).

[94] M. A. Eleiwa and A. Z. Elsherbeni. "Debye constants for biological tissues from 30 Hz to 20 GHz". *Applied Computational Electromagnetics Society Journal* 16.3 (2001), pp. 202–213 (cit. on p. 28).

[95] C. Dachena, A. Fanti, A. Fedeli, G. Mazzarella, M. Pastorino, and A. Randazzo. "Microwave imaging of cervical myelopathy: a preliminary feasibility assessment". *2020 14th European Conference on Antennas and Propagation (EuCAP)* (2020), pp. 1–4 (cit. on pp. 28–30, 33, 79–80, 83).

[96] M. Paulides, D. Wielheesen, J. Van Der Zee, and G. Van Rhoon. "Assessment of the local SAR distortion by major anatomical structures in a cylindrical neck phantom". *International Journal of Hyperthermia* 21.2 (2005), pp. 125–140 (cit. on pp. 29–30).

[97] C. Dichtl, P. Sippel, and S. Krohns. "Dielectric properties of 3D printed polylactic acid". *Advances in Materials Science and Engineering* 2017 (2017) (cit. on p. 29).

[98] J. Baker-Jarvis, M. D. Janezic, J. H. Grosvenor Jr, and R. G. Geyer. "Transmission/reflection and short-circuit line methods for measuring permittivity and permeability". *Nasa Sti/recon Technical Report N* 93 (1992), p. 12084 (cit. on p. 30).

[99] A. T. Whittle, I. Marshall, I. L. Mortimore, P. K. Wraith, R. J. Sellar, and N. J. Douglas. "Neck soft tissue and fat distribution: comparison between normal men and women by magnetic resonance imaging". *Thorax* 54.4 (1999), pp. 323–328 (cit. on pp. 30, 49).

[100] L. K. Kamibayashi and F. J. Richmond. "Morphometry of human neck muscles". *Spine* 23.12 (1998), pp. 1314–1323 (cit. on pp. 30, 49).

[101] C. Dachena, A. Fedeli, A. Fanti, M. B. Lodi, M. Pastorino, and A. Randazzo. "Microwave imaging for the diagnosis of cervical diseases: a feasibility analysis". *IEEE Journal of Electromagnetics, RF and Microwaves in Medicine and Biology* 5.3 (2020), pp. 277–285 (cit. on pp. 31–35, 37, 54, 73, 75, 79–80, 82–83).

[102] W. C. Chew. *Waves and fields in inhomogeneous media.* Vol. 16. Inst. of Electrical &, 1995 (cit. on p. 31).

[103] H. Bussey and J. Richmond. "Scattering by a lossy dielectric circular cylindrical multilayer numerical values". *IEEE Transactions on Antennas and Propagation* 23.5 (1975), pp. 723–725 (cit. on p. 32).

[104] J. Richmond. "Scattering by a dielectric cylinder of arbitrary cross section shape". *IEEE Transactions on Antennas and Propagation* 13.3 (1965), pp. 334–341 (cit. on p. 35).

[105] M. Ostadrahimi, P. Mojabi, C. Gilmore, A. Zakaria, S. Noghanian, S. Pistorius, and J. LoVetri. "Analysis of incident field modeling and incident/scattered field calibration techniques in microwave tomography". *IEEE Antennas and Wireless Propagation Letters* 10 (2011), pp. 900–903 (cit. on pp. 38, 73).

[106] C. Dachena, A. Fedeli, A. Fanti, M. B. Lodi, M. Pastorino, and A. Randazzo. "A microwave imaging technique for neck diseases monitoring". *2021 15th European Conference on Antennas and Propagation (EuCAP)* (2021), pp. 1–5 (cit. on pp. 40–44, 80–81, 83).

[107] S. Franceschini, M. Ambrosanio, F. Baselice, and V. Pascazio. "Neural networks for inverse problems: The microwave imaging case". *2021 15th European Conference on Antennas and Propagation (EuCAP)* (2021), pp. 1–5 (cit. on pp. 46, 61).

[108] C. Dachena, A. Fedeli, A. Fanti, M. B. Lodi, G. Fumera, A. Randazzo, and M. Pastorino. "Microwave imaging of the neck by means of artificial neural networks for tumor detection". *IEEE Open Journal of Antennas and Propagation* 2 (2021), pp. 1044–1056 (cit. on pp. 47, 52, 55, 63–65, 67–68, 70–71, 81–83).

[109] A. F. Agarap. "Deep learning using rectified linear units (relu)". *arXiv preprint arXiv:1803.08375* (2018) (cit. on p. 48).

[110] C. Dachena, A. Fedeli, M. Pastorino, A. Randazzo, A. Fanti, M. B. Lodi, and G. Fumera. "Microwave tomography of the neck with ANNs: preliminary results with simplified numerical phantoms". *2021 IEEE International Conference on Imaging Systems and Techniques (IST)* (2021), pp. 1–5 (cit. on pp. 49–51, 57–58, 60, 81, 83).

[111] P. M. Meaney, C. J. Fox, S. D. Geimer, and K. D. Paulsen. "Electrical characterization of glycerin: water mixtures: implications for use as a coupling medium in microwave tomography". *IEEE Transactions on Microwave Theory and Techniques* 65.5 (2017), pp. 1471–1478 (cit. on p. 50).

[112]   A. Christ, W. Kainz, E. G. Hahn, K. Honegger, M. Zefferer, E. Neufeld, W. Rascher, R. Janka, W. Bautz, J. Chen, et al. "The Virtual Family development of surface based anatomical models of two adults and two children for dosimetric simulations". *Physics in Medicine & Biology* 55.2 (2009), N23 (cit. on pp. 50, 66).

[113]   R. H. Bartels, J. C. Beatty, and B. A. Barsky. *An introduction to splines for use in computer graphics and geometric modeling.* Morgan Kaufmann, 1995 (cit. on p. 50).

[114]   A. Ruggeri. "Development and multiphysic analysis of a neck phantom for microwave hyperthermia". *2020 28th Telecommunications Forum (TELFOR)* (2020), pp. 1–4 (cit. on p. 54).

[115]   M. M. Paulides, J. F. Bakker, E. Neufeld, J. V. D. Zee, P. P. Jansen, P. C. Levendag, and G. C. Van Rhoon. "The HYPERcollar: a novel applicator for hyperthermia in the head and neck". *International Journal of Hyperthermia* 23.7 (2007), pp. 567–576 (cit. on p. 54).

[116]   R. Gaffoglio, M. Righero, G. Giordanengo, M. Zucchi, and G. Vecchi. "Fast optimization of temperature focusing in hyperthermia treatment of sub-superficial tumors". *IEEE Journal of Electromagnetics, RF and Microwaves in Medicine and Biology* 5.3 (2020), pp. 286–293 (cit. on pp. 54, 69).

[117]   M. Zanoli and H. D. Trefná. "Iterative time-reversal for multi-frequency hyperthermia". *Physics in Medicine & Biology* 66.4 (2021), p. 045027 (cit. on p. 54).

[118]   L. Hadjiiski, S. K. Mukherji, S. K. Gujar, B. Sahiner, M. Ibrahim, E. Street, J. Moyer, F. P. Worden, and H. P. Chan. "Treatment response assessment of head and neck cancers on CT using computerized volume analysis". *American Journal of Neuroradiology* 31.9 (2010), pp. 1744–1751 (cit. on p. 54).

[119]   N. Tong, S. Gou, S. Yang, D. Ruan, and K. Sheng. "Fully automatic multi-organ segmentation for head and neck cancer radiotherapy using shape representation model constrained fully convolutional neural networks". *Medical Physics* 45.10 (2018), pp. 4558–4567 (cit. on p. 54).

[120]   J. Y. Lim and M. Leech. "Use of auto-segmentation in the delineation of target volumes and organs at risk in head and neck". *Acta Oncologica* 55.7 (2016), pp. 799–806 (cit. on p. 54).

[121] P. Togni, Z. Rijnen, W. Numan, R. Verhaart, J. Bakker, G. Van Rhoon, and M. Paulides. "Electromagnetic redesign of the HYPERcollar applicator: toward improved deep local head-and-neck hyperthermia". *Physics in Medicine & Biology* 58.17 (2013), p. 5997 (cit. on p. 54).

[122] M. Bevacqua, G. G. Bellizzi, T. Isernia, and L. Crocco. "A method for effective permittivity and conductivity mapping of biological scenarios via segmented contrast source inversion". *Progress In Electromagnetics Research* 164 (2019), pp. 1–15 (cit. on p. 54).

[123] D. P. Kingma and J. Ba. "Adam: A method for stochastic optimization". *arXiv preprint arXiv:1412.6980* (2014) (cit. on p. 54).

[124] T. Drizdal, M. M. Paulides, N. van Holthe, and G. C. van Rhoon. "Hyperthermia treatment planning guided applicator selection for sub-superficial head and neck tumors heating". *International Journal of Hyperthermia* 34.6 (2018), pp. 704–713 (cit. on p. 69).

[125] C. Dachena, A. Fedeli, A. Fanti, M. B. Lodi, G. Fumera, M. Pastorino, and A. Randazzo. "A microwave imaging technique based on artificial neural networks for neck tumors detection". *2022 16th European Conference on Antennas and Propagation (EuCAP)* (2022), pp. 1–5 (cit. on pp. 72, 83).

[126] C. Dachena, A. Fedeli, A. Fanti, M. B. Lodi, G. Fumera, M. Pastorino, and A. Randazzo. "Initial experimental tests of an ANN-based microwave imaging technique for neck diagnostics". *IEEE Microwave and Wireless Components Letters* (2022) (cit. on pp. 73, 75–76, 82–83).